Topological Quantum Phases in Layered Systems with Rashba Spin-Orbit Interaction

Inauguraldissertation

zur

Erlangung der Würde eines Doktors der Philosophie

vorgelegt der

Philosophisch-Naturwissenschaftlichen Fakultät

der Universität Basel

von

Yanick André Volpez

Basel, 2020

Genehmigt von der Philosophisch-Naturwissenschaftlichen Fakultät
auf Antrag von

Prof. Dr. Daniel Loss

Prof. Dr. Jelena Klinovaja

Prof. Dr. Titus Neupert

Basel, den 21. April 2020

Prof. Dr. Martin Spiess
Dekan

Acknowledgments

First of all I would like to express my gratitude to my supervisor Prof. Daniel Loss for accepting me as one of his Ph. D. students, for giving me the opportunity to conduct cutting-edge research at the forefront of modern condensed matter theory, and for providing such a stimulating environment. I highly appreciate that Daniel is such an approachable person and that despite his very busy schedule, he was always willing to listen to new ideas or to discuss physics. I greatly benefited from these numerous discussions and was impressed by his broad knowledge on all aspects of quantum physics as well as his exceptional intuition.

I also would like to sincerely thank my second supervisor Prof. Jelena Klinovaja for providing such an extraordinary support, especially in the early stages of my Ph. D.. The fact that I could always walk into Jelena's office and ask all kinds of questions, that we even compared our Mathematica codes line for line, was such an enormous help and facilitated a successful start into my Ph. D.. Moreover, the completion of my dissertation would not have been possible without Jelena's ideas for new projects, her creativity in problem solving, and our one-on-one discussions.

Furthermore, I am also very thankful to Prof. Titus Neupert for accepting to co-referee my thesis and being part of the examination committee.

I would also like to thank Prof. Andrey Chubukov for hosting me and starting a collaboration with me. I had an amazing time in Minneapolis and it was a great pleasure to discuss with Andrey.

I am indebted to Katharina Laubscher, Kirill Plekhanov, and Christopher Reeg for taking their time to proof-read the manuscript and for providing countless helpful comments and criticism.

I have enjoyed four amazing, very intense years in Basel. Special thanks to all my working colleagues for creating such an amazing social atmosphere and all the good laughs (and some drinks). This was of paramount importance to me and I will never forget: Christoph Adelsberger, Ehud Amitai, Pavel Aseev, Stefano Bosco, Denis Chevallier, Oindrila Deb, Olesia Dmytruk, Sebastián Díaz, Tamás Haidekker Galambos, Richard Heß, Bence Hetényi, Silas Hoffman, Martin Koppenhöffer, Christoph Klöffel, Katharina Laubscher, Victor Ming Chua, Dmitry Miserev, Alex Mook, Kouki Nakata, Kirill Plekhanov, Christina Psaroudaki, Marko Rančić, Christopher Reeg, Flavio Ronetti, Alexandre Roulet, Constantin Schrade, Ferdinand Schulz, Tibor Sekera, Marcel Serina, Aleksandr Svetogorov, Pawel Szumniak, Manisha Thakurathi, James Wootton, and Alexander Zyuzin.

I am also very grateful to my previous supervisors as they had a big influence on my excitement about theoretical physics. I would like to thank Prof. Thomas Gehrmann for supporting me as a Bachelor's student and for giving me the opportunity to gain experience on actual research in theoretical particle physics already during the early stages of my physics studies at the University of Zurich. I also wish to thank Lorenzo Tancredi and Erich Weihs for being such patient, helpful and inspiring supervisors during these days.
Second I wish to express my deep appreciation of PD Michael Scherer with whom I carried out my Master's thesis at the University of Heidelberg. Our daily inter-

actions were always very enlightening and further excited my curiosity about condensed matter theory. I also would like to thank Laura Classen for co-supervising me. Laura was a big support and her willingness to discuss very openly all sorts of physics related questions had a great influence on me.

I would like to thank all my friends who have been around me for such a long time and have supported me through ups and downs during my studies.

Special thanks to Marlies Baumgärtner and Heinrich Ulrich for their moral and culinary support during all these years of studying.

I would like to express my deepest gratitude to Leonie Ulrich for being such a strong and loving companion on our joint path through life. Without Leonie I would never have reached the point I am at right now, and I am forever grateful to you.

Finally, I am deeply indebted to my parents Sabine Volpez and Remo Volpez, who have supported me all these years through my studies and who have always been there for me. You have encouraged me to try out different things, to pursue what feels right to me, and to find my own path. I am forever grateful to you for all what you have done for me.

Summary

The exploration of topological phases of quantum matter has attracted considerable interest of various research communities: the condensed matter physics community, the quantum information community, and importantly also industry[1]. The interest of fundamental research in these phases is manifold. For one, the use of the abstract notions of topology and its powerful statements in the context of quantum many-body systems extends the tools of conventional condensed matter theory. Moreover, the theory predicts new exotic phases with protected boundary states, which can have fractional quantum numbers and anyonic statistics. Non-Abelian anyons, Majorana bound states being the most prominent example, are especially interesting in the context of quantum computation, since their topological nature makes qubits formed from such states immune against decoherence. It is thus of fundamental interest to study those systems, especially experimentally, in order to shed light on the existence of these phases in Nature. At the same time, it will be important to check to what extent the aforementioned mathematical tools provide an accurate description of actual physical systems.

A lot of experimental achievements were reported in the last two decades, ranging from the first signatures of the quantum spin Hall effect and the topological surface states of three-dimensional (3D) topological insulators (TIs) to the zero-bias conductance peak associated with Majorana bound states (MBSs) in one-dimensional (1D) topological superconductors. Despite the great advances since these first experimental findings, there are still open questions, especially regarding MBSs, which need to be answered in order to decisively conclude whether or not the observed signatures actually are of topological origin.

At the same time, the search for alternative materials with topological phases continues. In this Thesis it is theoretically shown that there exists a class of materials, namely two-dimensional (2D) layers with strong Rashba spin-orbit interaction (SOI) (subsequently called Rashba layers for short), which can be used to fabricate heterostructures realizing a wide range of topological phases.

In particular, it is shown (see Chapter 3) how a stack of Rashba layers, can be used to build 3D topological phases. In the first part, it is proven that the system can be a 3D strong TI. Starting from this topological phase, it is demonstrated that by including strong electron-electron interactions the system fractionalizes and realizes a fractional 3D TI. The use of rotational symmetry and energy condensation arguments provides an intuitive way to reduce the problem to a set of interacting quasi-1D systems. This is one of the first concrete material candidates for such a phase which does not rely on a coupled-wires construction. In the last part of Chapter 3, it is shown that if the 2D layers not only have Rashba SOI, but a combination of Rashba and Dresselhaus SOI, the stack of layers can realize a Weyl semimetal.

Moreover, it is shown (see Chapter 4) how a Rashba bilayer can be used to

[1] Microsoft is by now running eight laboratories around the globe in order to study Majorana bound states and fabricate a topological quantum computer (see `https://www.microsoft.com/en-us/quantum/quantum-network`).

generate different 2D topological superconducting phases. The setup consists of a conventional s-wave superconductor sandwiched between two Rashba layers. Due to the proximity to the superconductor, the Rashba layers themselves become superconducting by the virtue of two competing pairing mechanisms: (i) direct Andreev pairing – a process where a Cooper pair as a whole tunnels into one of the layers and (ii) crossed Andreev pairing – a process where a Cooper pair splits and the electrons tunnel into opposite layers. The competition of these two processes leads to a 2D time-reversal invariant (TRI) topological superconducting phase when crossed Andreev pairing dominates. By applying a Zeeman, field the setup can be brought either into a chiral topological superconducting phase or a 2D gapless superconducting phase with unidirectional edge states. In essence, a Rashba bilayer system is a versatile platform which allows the realization of various 2D topological superconducting phases.

In Chapter 5, a system consisting of two tunnel-coupled Rashba layers which are proximitized by a top and bottom s-wave superconductor with a phase difference ϕ close to π is studied. This system is predicted to be a 2D TRI topological superconductor if the tunnel coupling is stronger than the proximity induced superconducting pairing strength. By breaking time-reversal symmetry with an inplane magnetic field, the system can be brought into the recently discovered second-order topological superconducting phase. In this phase, the bulk as well as the edges of the system are gapped, while in a square geometry two MBSs appear on opposite corners. Numerical results show that this finding even holds true if deviations from the $\phi = \pi$ phase difference between the parent superconductors is as large as $\delta\phi \approx \pi/3$. This implies that in an experiment, the phase difference does not need to be fine tuned.

In Chapter 6, an alternative way to fabricate a 1D TRI topological superconducting phase in a Josephson bijunction is presented. Concretely, the setup consists of a thin superconductor - insulator - superconductor (SIS) π-Josephson junction sandwiched between Rashba layers with opposite SOI. Due to the proximity effect, the Rashba layers themselves form a superconductor - normal conductor - superconductor (SNS) junction. The SIS junction is assumed to be thin enough such that electron tunneling between the Rashba layers is possible. This leads to a hybridization between the Andreev bound state bands (ABSBs) that emerge in the normal regions in the Rashba layers. Roughly speaking, the 1D channels formed by the ABSBs mimick the physical situation in tunnel coupled nanowires, and it is shown that indeed a topological phase with a Kramers pair of MBSs can emerge at the end of the normal regions.

Contents

Chapter 1

Prologue

Quantum condensed matter physics - the study of the quantum mechanical behavior of condensed matter - is one of the most exciting areas of modern physics research. It is at the heart of the digital revolution our world has witnessed in the last sixty years with the advent of semiconductor physics, and especially the development of MOSFET transistors and laser diodes. Nowadays, we are at a stage where humans are able to fabricate devices that have approximately $30 - 40$ transistors on an area as small as $1\mu\text{m}^2$ [1]. On such small length scales the quantum mechanical behavior of our world becomes evident, and although the quantum theory is one of the most tested and confirmed theories currently at hand, it never ceases to surprise us as its far reaching consequences are still being explored.

An ingenious idea that was put forward by Richard Feynman is to use quantum degrees of freedom to simulate other quantum systems[2]. This has created the fields of quantum simulators and quantum computation. In contrast to classical computers where information is stored in a binary fashion in the form of bits, quantum computers make use of quantum bits (qubits), the binary version of a quantum system. By definition, any quantum mechanical two-level system is a qubit. However, the search for a suitable physical system that not only implements one qubit, but that can also be scaled up to a system with many qubits poses a major challenge. Storing and processing information in qubits requires a coherent quantum state, which in general is quite sensitive to noise induced perturbations from the surrounding environment. Decoherence therefore leads to loss of information about the quantum state, and as such limits the operation of a quantum computer. Finding physical systems which realize qubits with long coherence times and fast operations is a very active field of research. Promising

[1] `https://en.wikipedia.org/wiki/Transistor_count`, accessed: 10.3.2020

[2] R. P. Feynman, International Journal of Theoretical Physics **21**, 6/7 (1982).

candidates range from optical lattices[3] to superconducting qubits[4] and quantum dots in semiconductors[5]. This last candidate is especially interesting from an industry point of view, as it was demonstrated that current industry standard in transistor fabrication can be used to build semiconductor spin-qubits[6]. It is thus highly probable that in the near future new quantum technologies will emerge and impact our everyday lives.

Besides all these exciting developments in technology, one could argue that the fundamental questions addressed by quantum condensed matter physics are even more fascinating. When many particles are brought together, the system as a whole can behave very differently from its individual constituents. There exist a plethora of phases, ranging from ordinary metals and insulators, where the elementary excitations are in a sense still the original constituents (electrons), to more exotic phases such as superconductors, Bose-Einstein condensates, (anti-) ferromagnets that have so-called collective excitations, where a macroscopic number of the original constituents 'conspire' together to form new types of particles. Then, there are even more exotic phases such as the integer and fractional quantum Hall effect, magnetic skyrmionic crystals, quantum spin liquids, two-dimensional topological insulators/superconductors, and this list is far from being exhaustive. In the search for a theoretical understanding of the phases of this last group, it was discovered rather recently that concepts and results from the mathematical field of topology can be used to characterize and classify them. This marked the beginning of a new research area, since for a long time almost all known phases and transitions between them were successfully described by Landau's theory of phase transitions which is based on local properties and the breaking of symmetry. Topological phases, in contrast, cannot be characterized in terms of a local order parameter, neither are transitions between different topological phases associated with the spontaneous breaking of a symmetry. They are characterized in terms of topological invariants, which capture global properties of a system and therefore, different topological phases do not need to differ in symmetries. In the next chapter, these notions will be made more precise.

In certain topological phases, states with non-Abelian statistics are predicted to emerge, which are particularly interesting as they could be used to implement

[3] G. K. Brennen, C. M. Caves, P. S. Jessen, and I. H. Deutsch, Phys. Rev. Lett. **82**, 1060 (1999).
[4] see *e.g.* T. D. Ladd, F. Jelezko, R. Laflamme, Y. Nakamura, C. Monroe, and J. L. O'Brien, Nature **464**, 45 (2010).
[5] D. Loss and D. P. DiVincenzo, Phys. Rev. A **57**, 120 (1998).
[6] R. Maurand *et al.*, Nat. Comm. **7**, 13575 (2016).

topological qubits[7]. Owing to their topological nature, such qubits are robust against local noise induced by the surrounding environment and thereby circumvent the problem of decoherence mentioned above. This seems to be a promising route to quantum computation, however, there is so far not a definite proof for the existence of non-Abelian states and thus there is still a lot of research to be done until the first topological qubit is operating.

The most prominent example of non-Abelian states are Majorana bound states (MBSs) which are predicted to exist at the end of one-dimensional (1D) p-wave superconductors[8] or in the vortex core of two-dimensional (2D) chiral p-wave superconductors[9]. Since the occurrence of p-wave superconductors in Nature is at best very rare, it was of great importance to the field when Fu *et al.*[10] realized that MBSs can also appear at superconducting vortices on surfaces of three-dimensional (3D) topological insulators (TIs). The next milestone was set in 2010 by Lutchyn *et al.*[11] and Oreg *et al.*[12], and subsequently by Nadj-Perge *et al.*[13] and Klinovaja *et al.*[14] when the authors came up with a realistic and well achievable proposal to realize MBSs in heterostructures built from only conventional materials, *i.e.*, materials that are topologically trivial, experimentally well understood and 'easily' available. The former two works considered a combination of a semiconducting nanowire with Rashba spin-orbit interaction (SOI) and an s-wave superconductor in a magnetic field, while the latter proposed to place magnetic adatoms on an s-wave superconductor. Both setups were realized in experiments with promising results showing essential features of MBS. Nevertheless, still more experimental work will have to be done in order to conclude whether the observed signatures actually are of topological origin.

The search for alternative topological systems is still ongoing and the aim of this Thesis is to demonstrate that many different topological phases can be realized with a particular class of materials: heterostructures made of 2D layers with strong Rashba spin-orbit interaction (subsequently called Rashba layers for short). The approach here is inspired by the above-mentioned works: Instead of looking for exotic materials that are intrinsically topological, a combination of conventional materials is used such that the system as a whole is in a topological

[7] see *e.g.*, C. Nayak *et al.*, Rev. Mod. Phys. **80**, 1083 (2008).
[8] A. Y. Kitaev, Phys.-Usp. 44, 131 (2001).
[9] D. A. Ivanov, Phys. Rev. Lett. **86**, 268 (2001).
[10] L. Fu and C. L. Kane, Phys. Rev. Lett. **100**, 096407 (2008).
[11] R. M. Lutchyn, J. D. Sau, and S. Das Sarma, Phys. Rev. Lett. **105**, 077001 (2010).
[12] Y. Oreg, G. Refael, and F. v. Oppen, Phys. Rev. Lett. **105**, 177002 (2010).
[13] S. Nadj-Perge, I. K. Drozdov, B. A. Bernevig, A. Yazdani, Phys. Rev. B **88**, 020407(R) (2013).
[14] J. Klinovaja, P. Stano, A. Yazdani, and D. Loss, Phys. Rev. Lett. **111**, 186805 (2013).

phase. It was possible to show that heterostructures built from Rashba layers can realize phases ranging from 3D fractional TIs to 2D topological superconductors of different kinds, and even second-order topological superconductors.

Chapter 2

Introduction

This chapter introduces all relevant concepts presented in the later chapters and provides some additional background information that some readers might find useful. The theory sections are not self-contained and are inspired by the countless excellent reviews, books, and especially the seminal works. For explicit calculations and more in-depth discussions the reader will be referred to these resources.

2.1 Topological Band Insulators

Band insulators belong to the most basic states of fermionic condensed matter, and yet, it seems that they were never really fully understood. Until recently, whenever a physical system was classified as an insulator, it was simply characterized by the size of its energy gap. From such a characterization one could conclude that, up to variations in the size of the energy gap, every insulator is the same. However, it turns out that insulators can have an additional topological property which allows a refined classification. More precisely, one can define an equivalence relation on the space of insulating non-interacting fermionic Hamiltonians, and show that under certain conditions there exists more than only one equivalence class.

Atomic and More General Insulators

Consider a lattice made of N atoms or molecules. The most basic insulator is the one where the electronic wavefunctions of neighboring atoms do not overlap, and thus all the electrons stay completely localized in the atomic orbitals on a particular lattice site. In such a case, it is easy to see that no electrical current can be transported. This system in which neighboring atoms do not interact and the electrons do not move between them is a highly idealized system and is usually referred to as the atomic insulator. In the discussion of equivalence classes

of insulators the atomic insulator serves as a reference point as it clearly is a representative of the class that will be called trivial.

A more general description of an insulator can be formulated as follows. Consider an infinitely extended system of identical atoms arranged in a Bravais lattice in the absence of any impurities. Then, the system has translational symmetry and Bloch's theorem applies. The second quantized fermionic Hamiltonian in d spatial dimensions then reads

$$H = \int_{\mathrm{BZ}} d^d k \; c^\dagger_{\boldsymbol{k}\alpha} \mathcal{H}_{\alpha\alpha'}(\boldsymbol{k}) c_{\boldsymbol{k}\alpha'}, \tag{2.1}$$

where BZ denotes the first Brillouin zone, $\boldsymbol{k}$ is the d-dimensional crystal momentum, $\alpha \in \{1, \ldots, n\}$ is a collective index describing spin, orbital, or sublattice degrees of freedom and $c^\dagger_{\boldsymbol{k}\alpha}$ is the creation operator for an electron in a state characterized by $(\boldsymbol{k}, \alpha)$. The Hamiltonian density $\mathcal{H}_{\alpha\alpha'}(\boldsymbol{k})$ is the Bloch Hamiltonian which describes the tunneling amplitude between two states labelled by α and α', respectively. The energy eigenstates of this Hamiltonian can easily be found by applying a unitary transformation, and the result will be a collection of n energy bands $\epsilon_\beta(\boldsymbol{k})$ with $\beta \in \{1, \ldots, n\}$. The system can be in an insulating state if and only if there exists an index i such that the relation

$$\epsilon_i(\boldsymbol{k}) < \epsilon_{i+1}(\boldsymbol{k}) \;\; \forall \boldsymbol{k} \tag{2.2}$$

holds. The quantity $\delta E = \min_{\boldsymbol{k}}[\epsilon_{i+1}(\boldsymbol{k}) - \epsilon_i(\boldsymbol{k})]$ is called the energy gap of the system, and the system is an insulator if all the energy bands until ϵ_i are fully occupied, and all higher bands are empty (at finite temperature T the energy gap also needs to be larger than the thermal energy $k_B T$).

Symmetry Classes and Equivalence Relation

In order to proceed it is useful to consider Hamiltonians with certain generic or fundamental symmetries. As is well-known, symmetries in quantum mechanics are represented as unitary or anti-unitary operators. If a Hamiltonian possesses a unitary symmetry, it can be block diagonalized and one can investigate the topological properties of each block individually. The fundamental symmetries which are considered are time-reversal symmetry (TRS) Θ, particle-hole symmetry $\mathcal{P}$, and the product of the two $\mathcal{C} = \Theta\mathcal{P}$. $\mathcal{C}$ is called chiral or sublattice symmetry. Note that a system can have chiral symmetry also when Θ and $\mathcal{P}$ individually are not symmetries. It can easily be shown that these operators satisfy $\Theta^2 = \pm 1$ and $\mathcal{P}^2 = \pm 1$ depending on the system. This divides the space of non-interacting gapped Hamiltonians into ten symmetry classes [1, 2] (see Table 2.1). In this

section, the discussion is restricted to insulators and the reader is referred to the next section for the discussion of Hamiltonians describing superconducting phases.

An equivalence relation in the space of insulating Hamiltonians can then be defined by using the adiabatic theorem. Consider an insulator in one of the symmetry classes presented in Table 2.1, which is described by a Hamiltonian $H(\boldsymbol{R})$, and which is in its non-degenerate ground state. Assume that $H(\boldsymbol{R})$ is completely specified by fixing the values of a set of parameters (such as, *e.g.*, hopping amplitudes) which are collected in a vector $\boldsymbol{R}$. If $\boldsymbol{R}$ is changed adiabatically, the system will stay in its (insulating) ground state at every point during this change. Therefore, two gapped Hamiltonians are called equivalent if there exists an adiabatic interpolation between the two that does not close the energy gap and respects all the symmetries of the symmetry class. It is straightforward to verify that this defines an equivalence relation. Note that this definition crucially relies on the presence of a spectral gap and therefore can only be established between insulators (or superconductors as will be discussed further below). A trivial insulator is then defined as an insulator that is equivalent to the atomic insulator, *i.e.*, it can be adiabatically deformed into a trivial product state.

Complete Classification of Non-Interacting Gapped Hamiltonians

Having established an equivalence relation between insulators, it is natural to ask how many equivalence classes besides the trivial class exist for a given symmetry class. The problem has then become a classification problem, which was solved by Kitaev [3] and Schnyder *et al.* [4], who gave an exhaustive classification of non-interacting gapped Hamiltonians in any dimension. The result is known as the periodic table of topological band insulators and superconductors (see Table 2.1). In summary, for each symmetry class in a particular dimension, there exists a topological invariant which (*i*) can take on only one value, (*ii*) which is $\mathbb{Z}$-valued, or (*iii*) which is $\mathbb{Z}_2$-valued. The type of invariant reveals how many equivalence classes exist, or equivalently, how many topologically distinct phases exist for a given symmetry class and dimension.

Another crucial concept in the context of topological band insulators and superconductors is the so-called bulk-boundary correspondence. The bulk-boundary correspondence states that if a system is studied in an open geometry, *i.e.*, in the presence of boundaries, there is a one-to-one correspondence between the value of the topological invariant, which is a bulk property, and the number of gapless states on the boundary. While Kitaev used K-theory to derive the periodic table, Schnyder and co-workers established a full classification by making use of this

	Θ^2	$\mathcal{P}^2$	$\mathcal{C}^2$	d	1	2	3	4	5	6	7	8
A	0	0	0		0	$\mathbb{Z}$	0	$\mathbb{Z}$	0	$\mathbb{Z}$	0	$\mathbb{Z}$
$AIII$	0	0	1		$\mathbb{Z}$	0	$\mathbb{Z}$	0	$\mathbb{Z}$	0	$\mathbb{Z}$	0
AII	-1	0	0		0	$\mathbb{Z}_2$	$\mathbb{Z}_2$	$\mathbb{Z}$	0	0	0	$\mathbb{Z}$
$DIII$	-1	+1	+1		$\mathbb{Z}_2$	$\mathbb{Z}_2$	$\mathbb{Z}$	0	0	0	$\mathbb{Z}$	0
D	0	+1	0		$\mathbb{Z}_2$	$\mathbb{Z}$	0	0	0	$\mathbb{Z}$	0	$\mathbb{Z}_2$
BDI	+1	+1	+1		$\mathbb{Z}$	0	0	0	$\mathbb{Z}$	0	$\mathbb{Z}_2$	$\mathbb{Z}_2$
AI	+1	0	0		0	0	0	$\mathbb{Z}$	0	$\mathbb{Z}_2$	$\mathbb{Z}_2$	$\mathbb{Z}$
CI	+1	-1	+1		0	0	$\mathbb{Z}$	0	$\mathbb{Z}_2$	$\mathbb{Z}_2$	$\mathbb{Z}$	0
C	0	-1	0		0	$\mathbb{Z}$	0	$\mathbb{Z}_2$	$\mathbb{Z}_2$	$\mathbb{Z}$	0	0
CII	-1	-1	+1		$\mathbb{Z}$	0	$\mathbb{Z}_2$	$\mathbb{Z}_2$	$\mathbb{Z}$	0	0	0

Table 2.1: Periodic table of topological band insulators and superconductors showing the type of topological invariant for all ten symmetry classes in dimensions $d \in \{1, \ldots, 8\}$. Note that the first two rows (classes A and $AIII$) have a periodicity of $d \to d+2$, while the remaining classes have a periodicity of $d \to d+8$. Each symmetry class is defined by the triple $(\Theta^2, \mathcal{P}^2, \mathcal{C}^2)$. Note that if, *e.g.*, a symmetry class has $\Theta^2 = 0$, this indicates that TRS is not a symmetry for this particular class (analogously for $\mathcal{P}$ and $\mathcal{C}$).

bulk-boundary correspondence. For a d-dimensional system, they studied the phenomenon of Anderson localization on its $(d-1)$-dimensional boundary, and showed that for topologically non-trivial phases, there exist gapless boundary states that evade Anderson localization, *i.e.*, they stay gapless also in the presence of disorder, which is assumed not to break the symmetries of the symmetry class.

In summary, a topologically non-trivial band insulator is a gapped system which has ν gapless boundary states protected against disorder and the number ν is determined by a topological invariant. Considering two Hamiltonians of one symmetry class, it is now clear that if and only if they have the same value of the topological invariant, there exists an adiabatic interpolation between the two that respects the symmetries and does not close the energy gap. Only then they are two representatives of the same equivalence class. Also, they have the same number of protected gapless boundary states. Conversely, if the value of their topological invariant is not the same, one cannot deform one Hamiltonian into the other without closing and reopening the bulk gap. This process of changing parameters such that the bulk gap of a system closes and reopens and the value of the topological invariant changes is a quantum phase transition which is called topological phase transition.

Note that the topological protection of the phases discussed above crucially relies on the energy gap and so far, zero temperature was assumed. However,

in reality, if the temperature is high enough thermal fluctuations can overcome the energy gap and the topological phase is no longer strictly protected since the bulk becomes conducting. Vice versa, if the energy gap is very small the topological phase might only be observable at unrealistically low temperatures. Similarly, if the strength of disorder becomes comparable to the size of the energy gap the topological protection can be lost. Thus, when considering the stability of a potential topological material, it is not only important to consider the topology of the energy bands and the symmetries of the system, but one also has to take into account the size of the energy gap.

Paradigmatic Example: Quantum Hall Effect

The integer quantum Hall (IQH) effect illustrates the paradigms introduced in the preceding section. The IQH effect was discovered in an experiment by Klitzing and co-workers in 1980 [5], where they measured the Hall conductance of a 2D electron gas in an external perpendicular magnetic field. Surprisingly, they observed that for strong magnetic fields the Hall conductance shows a discrete number of plateaus that appear at exact multiples of e^2/h, while the longitudinal conductance is zero. Nowadays, this universal quantization has been verified to one part in 10^{10} [6].

The connection to topology was then established by Thouless, Kohmoto, Nightingale and den Nijs (TKNN) [7], who calculated the Hall conductance σ_H from the Kubo formula. In essence, they were able to show that

$$\sigma_H = \frac{e^2}{h}\frac{1}{2\pi}\int dk_x \int dk_y \; F_{xy}(\boldsymbol{k}), \tag{2.3}$$

where

$$F_{xy}(\boldsymbol{k}) = \partial_{k_x} A_y(\boldsymbol{k}) - \partial_{k_y} A_x(\boldsymbol{k}), \tag{2.4}$$

$$A_i(\boldsymbol{k}) = -i \sum_{n \text{ filled}} \langle n\boldsymbol{k}|\partial_{k_i}|n\boldsymbol{k}\rangle\,, \tag{2.5}$$

are the definitions of the Berry curvature $F_{xy}(\boldsymbol{k})$, the Berry connection $A_i(\boldsymbol{k})$, and $|n\boldsymbol{k}\rangle$ denotes the Bloch wavefunction of the nth energy band at momentum $\boldsymbol{k}$. The quantity on the right-hand side of Eq. (2.3) is better known as the first Chern number of a fiber bundle, which only takes on integer values in units of 2π [8] and depends on the number of filled Landau levels. This shows that one can give an explanation of the quantization of the Hall conductance in terms of topology.

In the language of the periodic table introduced above, the quantum Hall insulator belongs to the symmetry class A as it neither has TRS nor particle-hole symmetry. The Chern number as defined in Eq. (2.3) constitutes the topological

invariant for this symmetry class in $d = 2$, which is why the entry in Table 2.1 is $\mathbb{Z}$.

The bulk-boundary correspondence for the quantum Hall effect is nicely evident from Eq. (2.3), when combined with the fact that the only conducting channels are the edge states and that each channel contributes a conductance quantum e^2/h. An argument for the existence of edge states was given by Laughlin [9]. By now, there exists a lot of numerical proof for the existence of edge states, and since more recently also very convincing experimental evidence [10]. Additionally, the edge states of the quantum Hall effect are called chiral, since they are propagating around a sample with a handedness that is set by the magnetic field.

Starting with the works by Pankratov [11] and Haldane [12], physicists started to look for quantum systems that have a non-zero Hall conductance without Landau levels, *i.e.*, in the absence of an external magnetic field. The topological invariant characterizing these generalized versions of the IQH effect is still given by the first Chern number, and thus these insulators are called *Chern insulators*.

TIs in Two Dimensions: the Importance of Spin-Orbit Interaction

It was not until the year 2005 that Kane and Mele theoretically discovered that there exists a time-reversal invariant (TRI) version of the IQH effect [13, 14]. Generally, one can show that in a time-reversal symmetric system the Berry curvature satisfies $F(\boldsymbol{k}) = -F(-\boldsymbol{k})$, and thus when integrated over the whole Brillouin zone (BZ) the integral vanishes and the Hall conductance σ_H is zero. However, assume that spin-up and spin-down electrons are in a IQH phase generated by a spin-dependent magnetic field that is opposite for opposite spins. Then the z component of the spin S_z is conserved and the system can be described by two decoupled sectors (for spin-up and spin-down) which are characterized by an opposite Hall conductance, *i.e.*, $\sigma_{H,\uparrow} = -\sigma_{H,\downarrow}$. The total Hall conductance is still zero, but one can define the so-called spin Hall conductance as $\sigma_S = \sigma_{H,\uparrow} - \sigma_{H,\downarrow} = 2e^2/h$. Invoking the bulk-boundary correspondence, it is clear that the system is insulating in the bulk and has helical edge states, *i.e.*, states which are localized on the edges and which counterpropagate for opposite spin projections. This simply follows from the fact that a non-zero Hall conductance guarantees chiral edge states, where their chirality depends on the sign of the Hall conductance. Since $\sigma_{H,\downarrow} = -\sigma_{H,\uparrow}$, it follows that the system has helical edge states.

This situation was first achieved in a theoretical model by Kane and Mele [13, 14], where the authors considered two copies of the Haldane model [12] with opposite mass terms for opposite spins. They showed that such a spin-dependent mass

term is generated by the intrinsic SOI, which generates an effective spin-dependent magnetic field. The SOI is an interaction that arises as a relativistic effect from the Dirac equation and couples the orbital and the spin degrees of freedom. Since in this model the S_z component is conserved, the spin Hall conductance as defined above is quantized to $\sigma_S = 2e^2/h$ and the phase is called a quantum spin Hall (QSH) insulator [13, 15]. The authors also introduced a new topological invariant [14] and showed that it is $\mathbb{Z}_2$-valued. This reflects the fact that in a time-reversal symmetric system with N pairs of helical edge states all edge states can be gapped out by disorder if N is even, and accordingly only $N-1$ edge states can be gapped out if N is odd. Note that this holds only for non-magnetic disorder. Therefore, in the topologically non-trivial phase, the system is characterized by the presence of an odd number of helical edge state pairs. The stability of this characterization strongly depends on TRS, more concretely on Kramers theorem. TRS guarantees that for every state with momentum $\boldsymbol{k}$ and energy $\epsilon(\boldsymbol{k})$ there exists a time-reversed partner with the same energy but opposite momentum $\epsilon(\boldsymbol{k}) = \epsilon(-\boldsymbol{k})$. When the system is put on a lattice there exist special points in the BZ: TRI momenta are mapped onto themselves under TRS modulo a reciprocal a lattice vector. This happens at the origin and the boundaries of the BZ. Kramers theorem states that the system must have a degeneracy at these TRI momenta: $\boldsymbol{k} = (0,0)$, $\boldsymbol{k} = (\pm\pi, 0)$, $\boldsymbol{k} = (0, \pm\pi)$, and $\boldsymbol{k} = (\pm\pi, \pm\pi)$. The dispersion of the helical edge states typically crosses at $k = 0$, where k denotes here the momentum along the edge, and thus this degeneracy cannot be lifted by any perturbation that preserves TRS and the helical edge states stay gapless. This is an example of a symmetry protected topological (SPT) phase.

In practice, the Kane-Mele model has the drawback that it relies on intrinsic SOI in graphene, which is on the order of a few meV. The energy gap opened by intrinsic SOI was shown to be only of the order of 10^{-3} meV [16–18], and therefore the QSH in graphene could only be observed for unrealistically low temperatures [16–18].

This problem was overcome by a model of Bernevig *et al.* on CdTe/HgTe quantum wells (BHZ model) [19, 20]. The mechanism responsible for the TRI topological phase discovered in this model, the inversion of energy bands, turned out to be quite generic for TIs [21]. Both materials, CdTe and HgTe, are semiconductors which around the center of the Brillouin zone (Γ-point) have an effective six-band model description in three-dimensions. There is an s-type band with total angular momentum $J = 1/2$ and four p-type bands with total angular momentum $J = 3/2$ due to SOI. Importantly, isolated CdTe and HgTe have an inverted band

ordering around the energy gap. The authors showed that if the thickness of the well material is larger than some critical value, the energy spectrum of the whole system shows a band inversion at the CdTe/HgTe interfaces and in this inverted regime the spin Hall conductance σ_S is quantized to $\sigma_S = 2e^2/h$. Only one year after this prediction, the group of Molenkamp carried out transport measurements and reported ballistic transport with $2e^2/h$ conduction [22]. Since then, there exist strong experimental evidences for a QSH in bismuthene on a SiC substrate [23] and a monolayer of WTe [24, 25].

In this Section, only models where S_z is conserved have been discussed so far. In general, this does not need to be the case to still allow for a topological classification. It turns out that the quantization of the spin Hall conductance σ_S is rather a consequence of the conservation of S_z than a topological feature. For time-reversal symmetric insulators the topological feature is essentially the existence of an odd number of helical edge state pairs [14]. This more general class, which includes the QSH, is termed topological insulators. As has become clear from the simple discussion in the beginning of this section and the more elaborate BHZ model, SOI is essential for TIs, and indeed almost any model for TIs crucially depends on it.

TIs in Three Dimensions

Soon after the pioneering works on 2D TIs, it was realized independently by three groups [26–28] that the results from two dimensions can be generalized to three dimensions. In essence, a 3D TI has an insulating bulk and gapless boundary states, which means that on every surface a single non-degenerate Dirac cone spectrum exists within the bulk gap. Additionally, these surface states feature spin-momentum locking such that the Dirac cone has a spin-structure where the spin of the states winds around the cone. This follows simply from TRS: for every state with momentum $\boldsymbol{k}$ and spin projection σ, there must exist a state with momentum $-\boldsymbol{k}$ and opposite σ. This winding of the spin gives rise to a π Berry phase. As in the 2D case, the surface states are protected against backscattering by TRS, and due to the π Berry phase of the Dirac cones these surface states show weak Anderson delocalization at low temperatures [29]. In 2008, the material $Bi_{1-x}Sb_x$ was the first one in which essential features of a 3D TI were confirmed. Angle-resolved photoemission spectroscopy (ARPES) and spin-resolved ARPES measurements were able to detect the Dirac cone surface states and confirm the spin-momentum locking of these states [30, 31]. Already one year later, a second generation of 3D TI materials was examined: Bi_2Se_3 [32], Bi_2Te_3 [33] and Sb_2Te_3 [34]. For a more

detailed discussion the interested reader is referred to the review by Hasan and Kane [35].

2.2 Topological Superconductors

Mean Field Approximation and Superconducting Pairing

The superconducting state is a state in which a quantum condensed matter system allows dissipationless transport of electrical current. In a fermionic system, this is only possible if electrons form bosonic bound states, known as Cooper pairs, which condense into the ground state and can be described by one macroscopic wavefunction Ψ. The dissipationless current is associated with collective excitations which correspond to variations of the phase of the macroscopic wavefunction Ψ (see, *e.g.*, Ref. [36]). In 1956, Cooper showed that the non-interacting ground state of an electron system is unstable against attractive electron-electron interactions, regardless of their strength, and that the instability shows up in the 'Cooper channel', *i.e.*, that correlations of the form $\sim \langle \psi^\dagger_{\boldsymbol{k}+\boldsymbol{q},\downarrow} \psi^\dagger_{-\boldsymbol{k}-\boldsymbol{q},\uparrow} \psi_{-\boldsymbol{k},\uparrow} \psi_{\boldsymbol{k},\downarrow} \rangle$ grow large [37]. Naturally, the question arises about the origin of the attractive interaction between electrons that is needed for bound states to form. Bardeen, Cooper and Schrieffer provided an answer in what has become known as BCS theory for conventional superconductors [38]: The interaction of electrons with phonons leads to an effective attractive interaction between electrons. In unconventional superconductors the origin of the attractive interaction is still a matter of lively debate. Put differently, consider the general form of a momentum- and spin-conserving electron-electron interaction in three spatial dimensions,

$$H_{int} \propto \sum_{\sigma,\sigma'} \int d^3k_1 \int d^3k_2 \int d^3q \; V_{\sigma\sigma'}(\boldsymbol{k}_1, \boldsymbol{k}_2, \boldsymbol{q}) c^\dagger_{\boldsymbol{k}_1+\boldsymbol{q},\sigma} c^\dagger_{\boldsymbol{k}_2-\boldsymbol{q},\sigma'} c_{\boldsymbol{k}_2,\sigma'} c_{\boldsymbol{k}_1,\sigma}. \quad (2.6)$$

If certain components of $V_{\sigma\sigma'}(\boldsymbol{k}_1, \boldsymbol{k}_2, \boldsymbol{q})$ are negative, *i.e.*, attractive, the system undergoes a phase transition to a superconducting state. As mentioned above, in conventional superconductors the attractive components are originating from phonon-mediated interactions. Interestingly, it is in principle possible that superconductivity occurs in a system with long range Coulomb-like interactions only. This is known as the Kohn-Luttinger instability [39], which is based on the fact that the effective electron-electron interaction will be a screened Coulomb interaction with Friedel oscillations. At larger distances these oscillations can cause overscreening and therefore certain components of $V_{\sigma\sigma'}(\boldsymbol{k}_1, \boldsymbol{k}_2, \boldsymbol{q})$ will become attractive [40].

Since the instability appears in the Cooper channel one can restrict Eq. (2.6) to $\boldsymbol{k}_1 = -\boldsymbol{k}_2$ (for zero center-of-mass momentum Cooper pairs), which leads to

$$H_{int} \propto \sum_{\sigma,\sigma'} \int d^3k \int d^3q \; V(\boldsymbol{k}, -\boldsymbol{k}, \boldsymbol{q})_{\sigma\sigma'} c^\dagger_{\boldsymbol{k}+\boldsymbol{q},\sigma} c^\dagger_{-\boldsymbol{k}-\boldsymbol{q},\sigma'} c_{-\boldsymbol{k},\sigma'} c_{\boldsymbol{k},\sigma}. \quad (2.7)$$

To further study the superconducting state, the standard approach is to perform a mean field analysis. This procedure relies on knowledge or an educated guess about the physics of the ground state. In the superconducting ground state expectation values of the form $\langle c^\dagger_{\boldsymbol{k}_2,\sigma'} c^\dagger_{\boldsymbol{k}_1,\sigma}\rangle$ are non-zero [41] due to the possibility to create/annihilate Cooper pairs. It is useful to define the superconducting pairing potential

$$\Delta^*_{\sigma\sigma'}(\boldsymbol{k}) = \int d^3q\; V_{\sigma\sigma'}(\boldsymbol{k},-\boldsymbol{k},\boldsymbol{q})\mathcal{F}_{\sigma\sigma'}(\boldsymbol{k},\boldsymbol{q}), \tag{2.8}$$

where $\mathcal{F}_{\sigma\sigma'}(\boldsymbol{k},\boldsymbol{q}) = \langle c^\dagger_{\boldsymbol{k}+\boldsymbol{q},\sigma} c^\dagger_{-\boldsymbol{k}-\boldsymbol{q},\sigma'}\rangle$ is the anomalous Green's function computed with respect to the superconducting ground state. In the next step, one considers only small fluctuations of the form $c^\dagger_{\boldsymbol{k},\sigma} c^\dagger_{-\boldsymbol{k},\sigma'}$ around $\mathcal{F}_{\sigma\sigma'}$ and approximates the interaction in Eq. (2.7) by

$$H_{int} \approx \sum_{\sigma,\sigma'} \int d^3k \left[\Delta^*_{\sigma\sigma'}(\boldsymbol{k}) c_{\boldsymbol{k},\sigma} c_{-\boldsymbol{k},\sigma'} + \Delta_{\sigma\sigma'}(\boldsymbol{k}) c^\dagger_{\boldsymbol{k},\sigma} c^\dagger_{-\boldsymbol{k},\sigma'}\right] + \text{constant}. \tag{2.9}$$

In this approximation the two-particle interaction is approximated by a single-particle term which describes the interaction of a single particle with a mean field.

Generally speaking, $\Delta_{\sigma\sigma'}(\boldsymbol{k})$ is a 2×2 matrix and, thus, can be parametrized as

$$\Delta(\boldsymbol{k}) = [\Delta_s \phi(\boldsymbol{k})\sigma_0 + \Delta_t \boldsymbol{d}(\boldsymbol{k})\cdot\boldsymbol{\sigma}](i\sigma_2), \tag{2.10}$$

where σ_0 is the 2×2 identity matrix, $\boldsymbol{\sigma} = (\sigma_1,\sigma_2,\sigma_3)$ is the vector of Pauli matrices, and $\phi(\boldsymbol{k})$ [$\boldsymbol{d}(\boldsymbol{k})$] decompose $\Delta(\boldsymbol{k})$ into its spin-singlet [spin-triplet] components. The superconducting pairing is then classified according to its behavior under rotational transformations. In analogy to the spherical harmonic functions, an isotropic pairing $\Delta(\boldsymbol{k}) = \Delta_s(i\sigma_2)$ is referred to as s-wave pairing. Another example is spin-triplet p-wave pairing which can be described by $\boldsymbol{d}(\boldsymbol{k}) = (k_y, k_x, 0)$. The mean field theory of superconductors serves as the starting point for the study of their topological properties, and although within the framework presented in the next section they formally appear like insulators, one should keep in mind that the physical ground state of such systems is completely different.

Bogoliubov - de Gennes Hamiltonian

The mean field superconducting Hamiltonian

$$H = \sum_{\sigma,\sigma'} \int d^dk \Big[c^\dagger_{\boldsymbol{k},\sigma} \mathcal{H}_{0,\sigma\sigma'}(\boldsymbol{k}) c_{\boldsymbol{k},\sigma'} + \Delta_{\sigma\sigma'}(\boldsymbol{k}) c^\dagger_{\boldsymbol{k},\sigma} c^\dagger_{-\boldsymbol{k},\sigma'} + \text{H.c.}\Big], \tag{2.11}$$

where $\mathcal{H}_0$ is the normal state Hamiltonian, can be exactly solved by performing a Bogoliubov transformation. A more convenient approach which also makes the

connection to topological band insulators manifest is to write the above Hamiltonian in the Nambu basis $\Phi_{\boldsymbol{k}} = (c_{\boldsymbol{k},\uparrow}, c_{\boldsymbol{k},\downarrow}, c^\dagger_{-\boldsymbol{k},\uparrow}, c^\dagger_{-\boldsymbol{k},\downarrow})^T$. Then the Hamiltonian reads

$$H = \int d^d k \; \Phi^\dagger_{\boldsymbol{k}} \mathcal{H}_{BdG}(\boldsymbol{k}) \Phi_{\boldsymbol{k}}, \tag{2.12}$$

$$\mathcal{H}_{BdG}(\boldsymbol{k}) = \begin{pmatrix} \mathcal{H}_0(\boldsymbol{k}) & \Delta(\boldsymbol{k}) \\ \Delta^\dagger(\boldsymbol{k}) & -\mathcal{H}_0^T(-\boldsymbol{k}) \end{pmatrix}. \tag{2.13}$$

Structure-wise, this Hamiltonian resembles the one in Eq. (2.1) where the Bloch Hamiltonian $\mathcal{H}(\boldsymbol{k})$ is replaced by the Bogoliubov - de Gennes (BdG) Hamiltonian $\mathcal{H}_{BdG}(\boldsymbol{k})$. For a simple quadratic dispersion $\xi_{\boldsymbol{k}} = \hbar^2|\boldsymbol{k}|^2/(2m) - \mu$ and conventional s-wave pairing this Hamiltonian has a spectrum with a gap of $2\Delta_s$. If the pairing is of p-wave type, the superconducting pairing has point nodes where it vanishes. However, depending on the form of $\mathcal{H}_0$, there might still be parameter regimes where the spectrum is gapped globally (see, *e.g.*, Refs. [42, 43]). It is worth noting that due to this representation, the system intrinsically has particle-hole symmetry, *i.e.*, there exists an anti-unitary operator $\mathcal{P}$ which anti-commutes with the Hamiltonian and satisfies $\mathcal{P}^2 = \pm 1$ [4]. It can be shown that $\mathcal{P}$ can be written as the product of a unitary operator $\mathcal{U}_\mathcal{P}$ and the complex conjugation operator $\mathcal{K}$, *i.e.*, $\mathcal{P} = \mathcal{U}_\mathcal{P}\mathcal{K}$. This then translates to the condition

$$\mathcal{U}_\mathcal{P}^{-1} \mathcal{H}_{BdG}(\boldsymbol{k}) \mathcal{U}_\mathcal{P} = -\mathcal{H}^*_{BdG}(-\boldsymbol{k}), \tag{2.14}$$

which in the case of a simple quadratic dispersion $\xi_{\boldsymbol{k}} = \hbar^2|\boldsymbol{k}|^2/(2m) - \mu$ and s-wave pairing $\Delta(\boldsymbol{k}) = \Delta_s(i\sigma_2)$ is satisfied for $\mathcal{U}_\mathcal{P} = \eta_1$, where η_i are the Pauli matrices acting in particle-hole space.

Whenever a superconductor has a fully gapped spectrum, all of the theory that was introduced above for topological band insulators also applies: For every symmetry class (with $\mathcal{P}^2 = \pm 1$) and any dimension there exists a topological invariant which characterizes the gapped bulk spectrum and determines the number of boundary states via the bulk-boundary correspondence.

Majorana Bound States and Their Non-Abelian Exchange Statistics

Majorana bound states are bound states that are pinned to zero energy. They show non-Abelian exchange statistics and appear at the boundary of 1D topological superconductors [42], in the core of vortices of the superconducting order parameter in 2D chiral p-wave superconductors [43], or also at corners of higher-order topological superconductors [44] (see further below).

Generally, a complex fermion operator c_α can always be decomposed into two real Majorana operators $\gamma_{\alpha,i}$

$$c_\alpha = \frac{1}{2}\Big(\gamma_{\alpha,1} + i\gamma_{\alpha,2}\Big), \tag{2.15}$$

where the Majorana operators satisfy $\gamma_{\alpha,i} = \gamma_{\alpha,i}^\dagger$ by definition. From the fermionic anti-commutation relation $\{c_\alpha, c_\beta^\dagger\} = \delta_{\alpha\beta}$ and $c_\alpha^2 = 0 = (c_\alpha^\dagger)^2$, one finds that they satisfy the anti-commutation relations

$$\{\gamma_\alpha, \gamma_\beta\} = 2\delta_{\alpha\beta}, \tag{2.16}$$

and thus also $\gamma_\alpha^2 = 1$. While such a decomposition is not always useful, it is a very convenient representation for certain models (see, *e.g.*, Ref. [42]). In the context of 1D p-wave topological superconductors, one MBS exists at each end of the system, say γ_L and γ_R for the left and right end, respectively. In the topologically non-trivial phase they form a non-local fermion

$$c = \frac{1}{2}\Big(\gamma_L + \gamma_R\Big). \tag{2.17}$$

In time-reversal symmetric 1D topological superconductors there is a Kramers pair of MBSs (see, *e.g.*, Refs. [45, 46]) at each end. Since they are Kramers partners they are orthogonal to each other and thus are prevented from hybridizing to become finite-energy states.

The main reason for the great interest in finding MBSs is that they have non-Abelian exchange statistics, which will be discussed now in a bit more detail. This paragraph is based on the presentations in [47, 48], and for an in-depth discussion the reader is encouraged to consider these resources.

Non-trivial exchange statistics of point-like particles strictly exists only for 2D systems. In this case, the wavefunction of a quantum state of n indistinguishable particles is not an irreducible representation of the symmetric group S_n, but of the braid group $\mathcal{B}_n$. This can be seen from the following simple considerations. Consider the path of two indistinguishable particles when adiabatically exchanged twice. This is equivalent to one particle encircling the other (see Fig. 2.1). In three spatial dimensions, this path can always be continuously deformed to a point (contracted) without going through the position of the other particle (see Fig. 2.1). It is therefore topologically equivalent to both particles not moving around each other at all. This means that this process should act on the wavefunction of these two particles as the identity map and, therefore, a single exchange alters the wavefunction by a factor of ± 1. This corresponds to conventional bosons and fermions. In two spatial dimensions the above mentioned contraction of the path to a point

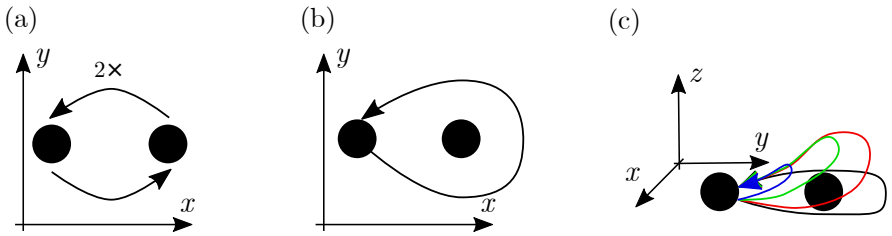

Figure 2.1: (a) The double-exchange of two indistinguishable point-like particles (black dots) is equivalent to one particle encircling the other (b). (c) Continuous deformation of the trajectory of a point-like particle encircling another particle in three dimensions. It is always possible to contract such a closed path to a point without passing through the second particle. Thus, the double-exchange of indistinguishable particles in 3D is equal to the identity map.

is impossible without the path passing through the position of the second particle. This has interesting consequences. If one considers the evolution of N particles at initial positions $(\boldsymbol{R}_{1,i}, \ldots, \boldsymbol{R}_{N,i})$ at time t_i to final positions $(\boldsymbol{R}_{1,f}, \ldots, \boldsymbol{R}_{N,f})$ at time t_f in a path integral formulation, one has to take into account all possible trajectories of these particles connecting the initial and final positions. The set of all trajectories can then be decomposed into different topological classes in the above sense. These classes are in one-to-one correspondence with the elements of the braid group $\mathcal{B}_N$. The braid group has infinite order, but has a quite simple description in terms of generators. Consider N ordered particles and denote by T_i the clockwise exchange of particle i with particle $(i+1)$. Then there exist $(N-1)$ generators $T_1, \ldots, T_{N-1}$ which satisfy the algebra

$$T_i T_j = T_j T_i \qquad \text{if } |i-j| \geq 2, \tag{2.18}$$

$$T_i T_{i+1} T_i = T_{i+1} T_i T_{i+1} \text{ for } 1 \leq i \leq N-1. \tag{2.19}$$

In order to describe the quantum evolution of such a system one has to define how the braid group acts on the states of the system, or in other words, under which representations of the braid group the physical states transform.

The simplest case are the 1D representations of the braid group where under the single exchange of two particles

$$\psi(\boldsymbol{r}_1, \boldsymbol{r}_2) \to e^{i\theta} \psi(\boldsymbol{r}_1, \boldsymbol{r}_2), \tag{2.20}$$

while $\theta = 0$ (π) corresponds to bosons (fermions), and in the general case $0 < \theta < \pi$ the particles are called Abelian anyons. This name stems from the fact that the representation of the braid group in this case is 1D and amounts to simply multiplying the quantum state by a phase factor. It becomes more interesting when

a system consisting of n indistinguishable particles at fixed positions $\boldsymbol{r}_1, \ldots, \boldsymbol{r}_n$ has a degenerate ground state space of dimension $\tilde{d}$. Then, there exist $\tilde{d}$-dimensional representations of $\mathcal{B}_n$ such that the exchange of, say, particles one and two is described by

$$\psi_\alpha \to [\rho(T_1)]_{\alpha\beta}\psi_\beta, \tag{2.21}$$

where ψ_α is the multi-particle wavefunction of the groundstate α and $\rho(T_1)$ is a $\tilde{d} \times \tilde{d}$ unitary matrix that furnishes the representation of T_1. This means that the exchange of two particles has the effect of generating rotations in the degenerate ground state subspace of the system. If $\rho(T_1)\rho(T_2) \neq \rho(T_2)\rho(T_1)$ the particles are called non-Abelian anyons. This connection between the exchange statistics and the ground state degeneracy is at the heart of topological order and will be further discussed below.

It was theoretically shown that MBS appearing in the vortex core of 2D chiral p-wave superconductors are an example of non-Abelian anyons [43]. In one spatial dimension particle exchange is not possible, but this problem can be circumvented, *e.g.*, by building effective 2D systems from nanowire networks. Importantly, it was shown that it is possible to braid MBS that appear at the boundary of 1D topological superconductors by creating such networks. The basic building block is a T-junction, which allows to define the braiding operation. Quite surprisingly, the MBS still show non-Abelian statistics for these kinds of braiding operations [49].

Given the theoretical prediction that MBS are non-Abelian anyons it is clear that the experimental confirmation of these states is not only of fundamental but also of practical interest: Non-Abelian anyons were proposed to be used as building blocks in a topological quantum computer, where the rotations generated by braiding [see Eq. (2.21)] can be used to implement logical quantum gates, for more details see Refs. [47, 49, 50]. However, this comes with the problem that one has to have great control over the location of the non-Abelian anyons used to set up the computational ground state subspace. Moreover, the anyons have to be moved around each other in an adiabatic manner since diabatic changes can lead out of the ground state subspace and the topological protection is lost. In a more modern approach to topological quantum computing this is circumvented by replacing the braiding operations with projective measurements [51–53].

2.3 Fractional Topological Insulators

In the previous sections, non-interacting topological phases and their classification were discussed. It is natural to ask whether this classification is stable once interactions between electrons are taken into account. If the interactions do not explicitly or spontaneously break any symmetries, their effect can be: (*i*) The topologically non-trivial phase is left invariant. (*ii*) Two topologically distinct phases of the non-interacting system can be adiabatically deformed into each other without closing the bulk gap. (*iii*) Strong correlations can enrich the classification Table 2.1 and change the topological invariant [54, 55], or (*iv*) most interestingly, strong correlations can lead to completely new phases with no non-interacting counterpart. In this last case, the strong correlations typically lead to fractionalized phases as for example in the fractional quantum Hall (FQH) effect.

According to the current understanding of interacting gapped topological phases of matter, they are divided into phases with short-range entanglement (SRE) and phases with long-range entanglement (LRE). The former goes under the name of (interacting) SPT states and the topological band insulators discussed above are simply the special (non-interacting) case of SPT states. The latter is one of the definitions of intrinsic topological order.

There are other possibilities to identify a system with topological order in (2+1) dimensions [54, 56]:

- A gapped quantum system with topological order has a robust (in the large size limit) ground state degeneracy on a torus or other compact manifolds with non-trivial topology, which is commonly referred to as topological ground state degeneracy (TGD). The robustness comes from the fact that any local operator has zero off-diagonal matrix elements in the degenerate ground state space. In a system of finite size L these terms scale as $\sim e^{-L/\xi}$, where ξ is some characteristic length scale [54]. However, the TGD does not provide a full characterization of the topological order, as different topological orders sometimes lead to the same TGD.

- The bulk has deconfined and dynamic low-energy quasi-particle excitations which carry fractional quantum numbers (such as fractional charge) and have fractional statistics. These particles are point-like in two dimensions, while in three dimensions there must also exist line-like excitations for non-trivial statistics. In order to make connection with the discussion of anyonic statistics above, it should be evident now that the statistics of the quasi-

particles is intimately connected with the TGD and in fact determined by the topological order.

The definition of topological order does not rely on any symmetries of the system. If, however, a topologically ordered state relies on a particular symmetry, it is called a symmetry-enriched topological state.

For a more in-depth discussion of topological order and interacting SPT states the reader is referred to Refs. [55–57]. After a brief description of the FQH effect, the remainder of this section is devoted to fractional TIs, which will be the central topic in the next chapter of this Thesis.

Fractional Quantum Hall Effect

The FQH effect is the prime example of a fractionalized phase. The physical picture and the theoretical methods that have emerged from studies of the FQH effect set the groundwork for the more recent developments in the exploration of interacting topological phases of matter. Therefore, this section briefly introduces the hallmarks of the FQH effect and highlights some of the theoretical developments associated with it.

In 1982, Tsui *et al.* [58] observed in very clean samples at strong magnetic fields that at fractional filling of the lowest Landau level a new plateau emerges at the fractional value of the Hall conductance

$$\sigma_H = \nu \frac{e^2}{h}, \tag{2.22}$$

where $\nu = 1/3$. It turned out that in fact a rich structure develops with many plateaus at different fractional fillings: $\nu = 1/3, 2/5, 3/7, \ldots$. Since only very clean samples show these features, it is clear that in contrast to the IQH effect, these plateaus cannot be explained by disorder. Additionally, the fact that the lowest Landau level is only partially filled but the system still shows an energy gap, suggests that many-body effects are crucial in the understanding of the FQH effect.

In a first theoretical attempt, Laughlin proposed a variational wavefunction for the many-body ground state that describes the fractional fillings at $\nu = 1/m$, with m an odd integer [59]. Exact diagonalization studies have shown that the Laughlin wavefunction has an overlap of up to 99% with the true ground state, hence the fillings with $\nu = 1/m$ are nowadays called Laughlin states. It can be shown theoretically that the quasi-particles (quasi-holes) carry fractional electric charge $e^* = -e/m$ ($e^* = e/m$), and they have Abelian anyonic statistics. As such, the $\nu = 1/3$ FQH effect is regarded as the archetype of a fractionalized phase. However, so far the anyonic statistics has not been directly observed in experiment.

Subsequently, Haldane [60] and Halperin [61] introduced the idea of a hierarchical structure in the FQH states, while Jain [62] introduced the idea of composite fermions in which electrons are bound to magnetic fluxes. The composite fermion approach by Jain allows to describe all observed filling fractions with odd denominators but is not able to capture the experimentally observed even denominator fillings. Moore and Read [63] were able to derive the many-body wavefunctions for the $\nu = 5/2$ filling and showed that excitations above the ground state have non-Abelian anyonic statistics.

All of these works were based on a microscopic description of the FQH effect, where the authors derived the many-body wavefunctions for the quasi-particles. This approach allowed to show that strongly interacting systems in 2D can have fractional electric charge and anyonic statistics.

In an attempt to give a universal characterization of the FQH phases, Wen introduced the concept of topological order briefly discussed above and suggested that the FQH phase is a manifestation of this new phase of matter [64].

Fractional TIs in Two Dimensions

In a spirit similar to the first construction of the QSH state, the simplest way to obtain a fractional TI is by taking the direct product of two time-reversed copies of a Laughlin state. Consider a system for which S_z is conserved and the spin-up (spin-down) electrons are in a FQH phase with $\nu = 1/m$ ($\nu = -1/m$). In this case, by construction, the system has topological order and the edges host helical edge states with fractional charges. This is the fractional quantum spin Hall (FQSH) effect discussed by Levin and Stern [65]. Alternatively, one can realize the FQSH phase in a coupled-wires construction with non-uniform SOI [66]. The FQSH phase was then generalized by Neupert *et al.* [67, 68] and Levin *et al.* [69] by considering models where S_z is not a good quantum number. They studied a topologically ordered 2D system where TRS is imposed and the bulk is described by an Abelian Chern-Simons (CS) field theory. The bulk-boundary correspondence for these theories was established in the context of the FQH effect and determines the 1D edge theory from the structure of the bulk CS theory. In the presence of electron-electron interactions, there exist TRS-preserving terms which can gap out the gapless edge states. Thus, in contrast to the non-interacting case, it is not guaranteed that an odd number of Kramers pairs of edge states cannot be gapped by (TRS-preserving) disorder. Neupert [67] and Levin [69] derived a stability criterion for the edge states in fractional TIs and showed that it depends on the universal data for the edge theory. Fractional TIs with an odd number of stable

Kramers pairs of edge states can be viewed as the fractionalized variants of the non-interacting TIs. Note that if all edge states are gapped out the system is still non-trivial since it is topologically ordered: The bulk quasi-particle excitations carry fractional charge and show fractional statistics.

Fractional TIs in Three Dimensions

In three spatial dimensions the situation is much less clear. Maciejko *et al.* [70] took a field theoretic approach inspired by the FQH effect and quantum chromodynamics, where the electron fractionalizes into partons, which themselves occupy a known SPT state. In this construction the authors were able to obtain an axion topological field theory (TFT) where the so-called θ-angle θ is a fraction of π. Note that it was shown that a non-interacting 3D TI can be described by an axion TFT with $\theta = \pi$ [71]. As is well-known, the surface of a 3D TI exhibits a half-integer QHE if TRS is broken. From the axion TFT it was derived that this result generalizes for fractional 3D TIs to [70]

$$\sigma_H = \frac{p}{q}\frac{e^2}{2h}, \tag{2.23}$$

where p and q are odd integers. Another way to obtain this result is by considering a coupled-wires construction in 3D [72, 73], where the authors confirm Eq. (2.23). All of these works suggest that there exist fractionalized versions of the non-interacting 3D TIs. However, while the TFT approach does not allow the identification of any candidate materials, the realization of a 3D coupled-wires network in an experiment is rather complicated. In fact, only a few works focused on candidate materials for fractional 3D TIs [74]. In Chapter 3 of this Thesis it is shown that a layered system consisting of stacked electron- and hole-gas layers with Rashba SOI can realize a fractional 3D TI.

2.4 Higher-Order Topology

The topological phases considered thus far assumed no or only 'generic' symmetries such as TRS, particle-hole symmetry, and the product of the two. In non-interacting systems this leads to the classification presented in Table 2.1, where the topologically non-trivial system behaves as a band insulator or superconductor in the bulk and exhibits gapless states localized on the boundary. These results were soon extended to include spatial symmetries such as the crystalline space groups [75]. As a special subgroup of topological crystalline insulators, Schindler *et al.* [76] introduced the concept of higher-order topological phases for certain combinations of spatial and temporal symmetries (product of mirror reflection and TRS or the product of four-fold rotation and TRS, see also Ref. [77]). Before the introduction of this more general concept, certain higher-order topological insulators were known under the name of quantized electric multipole insulators studied in the works by Benalcazar *et al.* [78–80]. Geier *et al.* further showed that an order-two crystalline symmetry is enough for second-order topological phases in $d = 2$ and $d = 3$ [44].

For higher-order topological phases there exists a generalized bulk-boundary correspondence. For an nth-order topological phase in d spatial dimensions, the system has a gapped bulk spectrum and topologically protected gapless states on

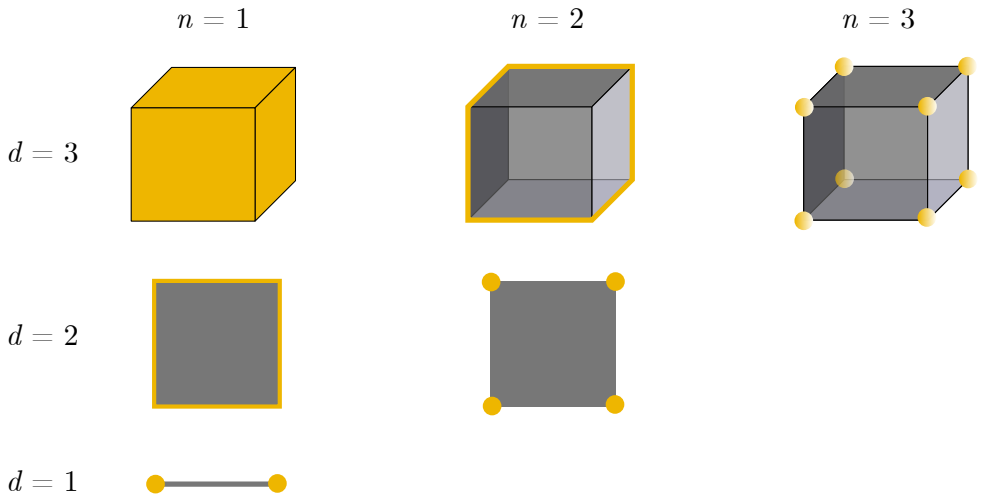

Figure 2.2: Schematic illustration of first-order ($n = 1$), second-order ($n = 2$), and third-order ($n = 3$) topological phases in different dimensions d. The first-order topological phases have gapless states (yellow) on all boundaries and a gapped bulk (grey). A d-dimensional system in a higher-order phase with $n > 1$ does not necessarily have gapless states on all of its $(d - n)$-dimensional boundaries.

its $(d-n)$-dimensional boundary (see Fig. 2.2). In contrast to the conventional topological phases presented above, the higher-order topological phases do not necessarily have gapless states on all of their $(d-n)$-dimensional boundaries. Also note that in this formulation, the topological phases presented above are first-order topological phases. The higher-order topological phases are topologically trivial within the classification of first-order topological phases. However, the $(d-n+1)$-dimensional boundaries can be viewed as separate topological gapped systems, and the gapless boundary states appear where two adjacent surfaces, hinges, or edges are characterized by different topological invariants.

Generally, the literature distinguishes between intrinsic and extrinsic higher-order topological phases [44]. Extrinsic higher-order topological systems typically arise if no particular spatial symmetries are present. For example, a 2D second-order topological superconductor has zero-energy MBS at some of its corners. In the absence of any spatial symmetries, these corner states are protected by the energy gap of the edge. This means that the corner states can disappear if the edge gap is closed and then reopened. On the other hand, the corner states of intrinsic higher-order topological phases are protected by the bulk energy gap. However, these phases require additional symmetries such as the particular combination of spatial and temporal symmetries [76] or order-two spatial symmetries [44]. As a result, no perturbation which respects the symmetries of the system and leaves the bulk gap open can make the corner states disappear. In contrast to the extrinsic phase, this specifically implies that in the intrinsic phase a symmetry-preserving perturbation can close and reopen any edge gap and the corner states will remain. The only possible change is that the corner states are relocated in a way that respects the symmetry, but the existence of the corner states is guaranteed as long as the bulk gap is not closed.

Despite the fact that the field of higher-order topology is relatively new, first experimental evidences already exist. Experimental and theoretical groups joined forces to reveal that hexagonal bismuth nanowires grown along a particular axis show signatures of higher-order topology. The presence of narrow conducting channels localized at hinges was shown by performing scanning tunneling microscope and Josephson interferometry measurements [81, 82].

As of now, there exist several new proposals for 2D second-order topological superconductors [83–89], 2D second-order topological insulators [90, 91], 3D second-order topological insulators [92, 93], and even fractional 2D second-order topological superconductors [94–96].

Additionally, characteristics of higher-order topological insulators were also

found in classical systems such as in an electric circuit realization [97] or acoustic crystals [98, 99].

2.5 Engineered Topological Matter

As already mentioned in the Prologue, Kitaev showed in his seminal work that MBSs can occur at the end of 1D spinless p-wave superconductors [42]. Similarly, Ivanov demonstrated the occurence of MBSs in vortex cores of 2D chiral p-wave superconductors [43]. Unfortunately, p-wave superconductors are extremely rare in Nature, and it is not clear which material could be used to study MBSs in experiment. This has motivated theorists to look for new ways to realize topological superconductors and in particular MBSs. In their pioneering work, Fu and Kane showed that a MBS occurs if conventional s-wave superconductors are placed on one of the surfaces of a 3D TI such as to create a vortex [100]. The idea to combine materials in order to create topological states of matter was then quickly explored further. In the most popular example, the idea is to reproduce the physics of a 1D spinless p-wave superconductor. This can be done using a semiconducting nanowire where the spin-degeneracy is lifted due to Rashba SOI [101, 102]. Applying a magnetic field along the nanowire axis opens a partial gap in the spectrum and removes the spin degree of freedom, such that the system is essentially spinless. If the system is brought into contact with a conventional s-wave superconductor, it can be shown that the combination of these three ingredients exactly maps to Kitaev's toy model. This was one of the first examples of how 1D topological superconductors can be generated by using a combination of 'ordinary', topologically trivial materials. It should be emphasized that for this scheme to work it is essential that the nanowire either has strong SOI or that the magnetic field has a helical texture while the SOI is zero. This second approach was pursued in the works by Nadj-Perge *et al.* [103] and Klinovaja *et al.* [104], where the authors studied a chain of magnetic adatoms on a conventional superconductor. It can be shown that due to Ruderman-Kittel-Kasuya-Yosida (RKKY) interactions a helical magnetic order forms [104], and that the low-energy description of the system is equivalent to Kitaev's toy model. Both platforms were well within reach of experimental techniques, and thus, quite quickly first experiments could be carried out. Transport measurements in the Rashba nanowires showed the existence of a zero-bias peak in the conductance, while atomic-force microscope measurements on the magnetic chain also revealed the spatial information of the localized states at the end of the chain. This rapid success motivated physicists to further look for relatively simple heterostructures made of conventional materials that realize new topological phases.

It was discovered quickly that in fact many topological phases can be realized when the right combination of materials is used, *e.g.*, topological superconducting

phases [45, 46, 105, 106], topological phases in periodically driven systems [107–110], or fractional phases [106, 111–119] (this list is by far not exhaustive). Some of these approaches relied on a coupled-wires construction to produce 2D or 3D phases. While as a theoretical tool this approach allows to conveniently treat interacting systems in these higher dimensions, it becomes notoriously difficult to realize a 3D nanowire network in an experiment. In this Thesis, the approach of engineering topological matter is taken further and it is shown that a variety of 2D and 3D topological phases can be constructed from coupled 2D layers with Rashba SOI. Using layered materials to engineer higher-dimensional topological phases significantly simplifies the heterostructure as compared to coupled-wires structures and makes them more likely to be realized in an experiment.

Bibliography

[1] M. R. Zirnbauer, J. Math. Phys. **37**, 4986 (1996).

[2] A. Altland and M. R. Zirnbauer, Phys. Rev. B **55**, 1142 (1997).

[3] A. Kitaev, AIP Conference Proceedings **1134**, 22 (2009).

[4] S. Ryu, A. P. Schnyder, A. Furusaki, and A. W. W. Ludwig, New J. Phys. **12**, 065010 (2010).

[5] K. v. Klitzing, G. Dorda, and M. Pepper, Phys. Rev. Lett. **45**, 494 (1980).

[6] B. Jeckelmann and B. Jeanneret, Rep. Prog. Phys. **64**, 1603 (2001).

[7] D. J. Thouless, M. Kohmoto, M. P. Nightingale, and M. den Nijs, Phys. Rev. Lett. **49**, 405 (1982).

[8] see e.g. M. Nakahara, *Geometry, Topology and Physics*, 2nd ed., CRC Press, 2003.

[9] R. B. Laughlin, Phys. Rev. B **23**, 5632(R) (1981).

[10] T. Patlatiuk, C. P. Scheller, D. Hill, Y. Tserkovnyak, G. Barak, A. Yacoby, L. N. Pfeiffer, K. W. West, and D. M. Zumbühl, Nat. Comm. **9**, 3692 (2018).

[11] O. A. Pankratov, Phys. Rev. A **121**, 360 (1987).

[12] F. D. M. Haldane, Phys. Rev. Lett. **61**, 2015 (1988).

[13] C. L. Kane and E. J. Mele, Phys. Rev. Lett. **95**, 226801 (2005).

[14] C. L. Kane and E. J. Mele, Phys. Rev. Lett. **95**, 146802 (2005).

[15] B. A. Bernevig and S.-C. Zhang, Phys. Rev. Lett. **96**, 106802 (2006).

[16] H. Min, J. E. Hill, N. A. Sinitsyn, B. R. Sahu, Leonard Kleinman, and A. H. MacDonald, Phys. Rev. B **74**, 165310 (2006).

[17] D. Huertas-Hernando, F. Guinea, and A. Brataas, Phys. Rev. B **74**, 155426 (2006).

[18] Y. Yao, F. Ye, X.-L. Qi, S.-C. Zhang, and Z. Fang, Phys. Rev. B **75**, 041401(R) (2007).

[19] C. Wu, B. A. Bernevig, and S. Zhang, Phys. Rev. Lett. **96**, 106401 (2006).

[20] B. A. Bernevig, T. L. Hughes, and S. Zhang, Science **314**, 5806 (2006).

[21] B. A. Bernevig and T. L. Hughes, *TIs and Topological Superconductors*, Princeton University Press, 2013.

[22] M. König, S. Wiedmann, C. Brüne, A. Roth, H. Buhmann, L. W. Molenkamp, X. Qi, and S. Zhang, Science **318**, 5851 (2007).

[23] F. Reis, G. Li, L. Dudy, M. Bauernfeind, S. Glass, W. Hanke, R. Thomale, J. Schaʹafer, and R. Claessen, Science **357**, 287 (2017).

[24] Z. Fei, T. Palomaki, S. Wu, W. Zhao, X. Cai, B. Sun, P. Nguyen, J. Finney, X. Xu, and David H. Cobden, Nat. Phys. **13**, 677 (2017).

[25] S. Tang *et al.*, Nat. Phys. **13**, 683 (2017).

[26] L. Fu, C. L. Kane, and E. J. Mele, Phys. Rev. Lett. **98**, 106803 (2007).
[27] J. E. Moore and L. Balents, Phys. Rev. B **75**, 121306(R) (2007).
[28] R. Roy, Phys. Rev. B **79**, 195322 (2009).
[29] H. Suzuura and T. Ando, Phys. Rev. Lett. **89**, 266603 (2002).
[30] D. Hsieh, D. Qian, L. Wray, Y. Xia, Y. S. Hor, R. J. Cava, and M. Z. Hasan, Nature **452**, 970 (2008).
[31] D. Hsieh,Y. Xia, L. Wray, D. Qian, A. Pal, J. H. Dil, J. Osterwalder, F. Meier, G. Bihlmayer, C. L. Kane, Y. S. Hor, R. J. Cava, M. Z. Hasan, Science **323**, 919 (2009).
[32] Y. Xia, D. Qian, D. Hsieh, L. Wray, A. Pal, H. Lin, A. Bansil, D. Grauer, Y. S. Hor, R. J. Cava, and M. Z. Hasan, Nat. Phys. **5**, 398 (2009).
[33] Z. Alpichshev, J. G. Analytis, J.-H. Chu, I. R. Fisher, Y. L. Chen, Z. X. Shen, A. Fang, and A. Kapitulnik, Phys. Rev. Lett. **104**, 016401 (2010).
[34] D. Hsieh *et al.*, Phys. Rev. Lett. **103**, 146401 (2009).
[35] M. Z. Hasan and C. L. Kane, Rev. Mod. Phys **82**, 4 (2010).
[36] A. Altland and B. Simons, *Condensed Matter Field Theory*, Cambridge University Press, 2010.
[37] L. Cooper, Phys. Rev. **104**, 1189 (1956).
[38] J. Bardeen, L. Cooper, and J. R. Schrieffer, Phys. Rev. **108**, 1175 (1957).
[39] W. Kohn and J. m. Luttinger, Phys. Rev. Lett. **15**, 524 (1965).
[40] S. Maiti and A. V. Chubukov, AIP Conference Proceedings **1150**, 3 (2013).
[41] A. A. Abrikosov, L. P. Gorkov, and I. E. Dzyaloshinski, *Methods of quantum field theory in statistical physics*, Dover Publications Inc. New York, 2017.
[42] A. Y. Kitaev, Phys.-Usp. **44**, 131 (2001).
[43] D. A. Ivanov, Phys. Rev. Lett. **86**, 268 (2001).
[44] M. Geier, L. Trifunovic, M. Hoskam, and P. W. Brouwer, Phys. Rev. B **97**, 205135 (2018).
[45] F. Zhang, C. L. Kane, and E. J. Mele, Phys. Rev. Lett. **111**, 056402 (2013).
[46] J. Klinovaja and D. Loss, Phys. Rev. B **90**, 045118 (2014).
[47] C. Nayak, S. H. Simon, A. Stern, M. Freedman, and S. Das Sarma, Rev. Mod. Phys. **80**, 3 (2008).
[48] M. Gaberdiel, Lecture notes on *Symmetries in Physics*, held at ETH Zürich, Fall Semester 2013, available at: *http://edu.itp.phys.ethz.ch/hs13/Symmetries/notes/Symmetries.pdf*.
[49] J. Alicea, Y. Oreg, G. Refael, F. v. Oppen, and M. P. A. Fisher, Nat. Phys. **7**, 412 (2011).
[50] A. Hutter and D. Loss, Phys. Rev. B **93**, 125105 (2016).
[51] P. Bonderson, M. H. Freedman, and C. Nayak, Phys. Rev. Lett. **101**, 010501 (2008).
[52] P. Bonderson, M. H. Freedman, and C. Nayak, Ann. Phys. (Amsterdam) **324**, 787 (2009).
[53] H. Zheng and A. Dua, and L. Jiang, New J. Phys. **18**, 123027 (2016)
[54] B. A. Bernevig and T. Neupert, Lecture Notes on: *Topological Superconductivity and Category Theory*, arXiv:1506.05805
[55] T. Senthil, Annu. Rev. Condens. Matter Phys. **6**, 299 (2015).
[56] X.-G. Wen, Rev. Mod. Phys. **89**, 041004 (2017).
[57] S. Rachel, Rep. Prog. Phys. **81**, 1165 (2018).
[58] D. C. Tsui, H. L. Stormer, and A. C. Gossard, Phys. Rev. Lett. **48**, 1559 (1982).
[59] R. B. Laughlin, Phys. Rev. Lett. **50**, 1395 (1983).
[60] F. D. M. Haldane, Phys. Rev. Lett. **51**, 7 (1983).
[61] B. I. Halperin, Phys. Rev. Lett. **52**, 18 (1984).
[62] J. K. Jain, Phys. Rev. Lett. **63**, 2 (1989).

[63] G. Moore and N. Read, Nuc. Phys. B **360**, 361 (1991).
[64] X.-G. Wen, Int. J. Mod. Phys. B **05**, 1641 (1990).
[65] M. Levin and A. Stern, Phys. Rev. Lett. **103**, 196803 (2009).
[66] J. Klinovaja and Y. Tserkovnyak, Phys. Rev. B **90**, 115426 (2014).
[67] T. Neupert, L. Santos, S. Ryu, C. Chamon, and C. Mudry, Phys. Rev. B **84**, 165107 (2011).
[68] L. Santos, T. Neupert, S. Ryu, C. Chamon, and C. Mudry, Phys. Rev. B **84**, 165138 (2011).
[69] M. Levin and A. Stern, Phys. Rev. B **86**, 115131 (2012).
[70] J. Maciejko, X.-L. Qi, A. Karch, and S.-C. Zhang, Phys. Rev. Lett. **105**, 246809 (2010).
[71] X.-L. Qi, T. L. Hughes, and S.-C. Zhang, Phys. Rev. B **78**, 195424 (2008).
[72] E. Sagi and Y. Oreg, Phys. Rev. B **92**, 195137 (2015).
[73] T. Meng, Phys. Rev. B **92**, 115152 (2015).
[74] J. Maciejko and G. A. Fiete, Nat. Phys. **11**, 385 (2015).
[75] L. Fu, Phys. Rev. Lett. **106**, 106802 (2011).
[76] F. Schindler, A. M. Cook, M. G. Vergniory, Z. Wang, S. S. P. Parkin, B. A. Bernevig, and T. Neupert, Sci. Adv. **4**, eaat0346 (2018).
[77] Z. Song, Z. Fang, and C. Fang, Phys. Rev. Lett. **119**, 246402 (2017).
[78] W. A. Benalcazar, J. C. Y. Teo, and T. L. Hughes, Phys. Rev. B **89**, 224503 (2014).
[79] W. A. Benalcazar, B. A. Bernevig, and T. L. Hughes, Science **357**, 61 (2017).
[80] W. A. Benalcazar, B. A. Bernevig, and T. L. Hughes, Phys. Rev. B **96**, 245115 (2017).
[81] F. Schindler *et al.*, Nat. Phys. **14**, 918 (2018).
[82] A. Murani *et al.*, Nat. Comm. **8**, 15941 (2017).
[83] M. Ezawa, Phys. Rev. Lett. **121**, 116801 (2018).
[84] X. Zhu, Phys. Rev. B **97**, 205134 (2018).
[85] Q. Wang, C.-C. Liu, Y.-M. Lu, and F. Zhang, Phys. Rev. Lett. **121**, 186801 (2018).
[86] Z. Yan, F. Song, and Z. Wang, Phys. Rev. Lett. **121**, 096803 (2018).
[87] X. Zhu, Phys. Rev. Lett. **122**, 236401 (2019).
[88] Z. Yan, Phys. Rev. B **100**, 205406 (2019).
[89] K. Plekhanov, M. Thakurathi, D. Loss, and J. Klinovaja, Phys. Rev. Res. **1**, 032013(R) (2019).
[90] F. Schindler, M. Brzezińska, W. A. Benalcazar, M. Iraola, A. Bouhon, S. S. Tsirkin, M. G. Vergniory, and T. Neupert, Phys. Rev. Res. **1**, 033074 (2019).
[91] M. J. Park, Y. Kim, G. Y. Cho, and S. B. Lee, Phys. Rev. Lett. **123**, 216803 (2019).
[92] K. Plekhanov, F. Ronetti, D. Loss, and J. Klinovaja, Phys. Rev. Res. **2**, 013083 (2019).
[93] P. Szumniak, D. Loss, and J. Klinovaja, arXiv:1910.05090.
[94] Y. You, arXiv:1908.04299.
[95] K. Laubscher, D. Loss, and J. Klinovaja, Phys. Rev. Res. **1**, 032017 (2019).
[96] K. Laubscher, D. Loss, and J. Klinovaja, arXiv:1912.10931.
[97] S. Imhof, C. Berger, F. Bayer, J. Brehm, L. W. Molenkamp, T. Kiessling, F. Schindler, C. H. Lee, M. Greiter, T. Neupert, and R. Thomale, Nat. Phys. **14**, 925 (2018).
[98] X. Zhang, H.-X. Wang, Z.-K. Lin, Z. Tian, B. Xie, M.-H. Lu, Y.-F. Chen, and J.-H. Jian, Nat. Phys. **15**, 582 (2019).
[99] H. Xue, Y. Yang, F. Gao, Y. Chong, and B. Zhang, Nat. Mat. **18**, 108 (2019).
[100] L. Fu and C. L. Kane, Phys. Rev. Lett. **100**, 096407 (2008).
[101] R. M. Lutchyn, J. D. Sau, and S. Das Sarma, Phys. Rev. Lett. **105**, 077001 (2010).
[102] Y. Oreg, G. Refael, and F. v. Oppen, Phys. Rev. Lett. **105**, 177002 (2010).

[103] S. Nadj-Perge, I. K. Drozdov, B. A. Bernevig, A. Yazdani, Phys. Rev. B **88**, 020407(R) (2013).
[104] J. Klinovaja, P. Stano, A. Yazdani, and D. Loss, Phys. Rev. Lett. **111**, 186805 (2013).
[105] I. Seroussi, E. Berg, and Y. Oreg, Phys. Rev. B **89**, 104523 (2014).
[106] J. Klinovaja, A. Yacoby, and D. Loss, Phys. Rev. B **90**, 155447 (2014).
[107] A. G. Grushin, Á. Gómez-León, and T. Neupert, Phys. Rev. Lett. **112**, 156801 (2014).
[108] J. Klinovaja, P. Stano, and D. Loss, Phys. Rev. Lett. **116**, 176401 (2016).
[109] M. Thakurathi, D. Loss, and J. Klinovaja, Phys. Rev. B **95**, 155407 (2017).
[110] M. Thakurathi, P. P. Aseev, D. Loss, and J. Klinovaja, arXiv:1910.03730.
[111] Y.-L. Wu, B. A. Bernevig, and N. Regnault, Phys. Rev. B 85, 075116 (2012).
[112] J. Klinovaja and D. Loss, Phys. Rev. Lett. **111**, 196401 (2013).
[113] J. Klinovaja and D. Loss, Phys. Rev. Lett. **112**, 246403 (2014).
[114] Y. Oreg, E. Sela, and A. Stern, Phys. Rev. B **89**, 115402 (2014).
[115] E. Sagi and Y. Oreg, Phys. Rev. B **90**, 201102(R) (2014).
[116] J. Klinovaja, Y. Tserkovnyak, and D. Loss, Phys. Rev. B **91**, 085426 (2015).
[117] E. Sagi and Y. Oreg, Phys. Rev. B **92**, 195137 (2015).
[118] E. Sagi, A. Haim, E. Berg, F. v. Oppen, and Y. Oreg, Phys. Rev. B **96**, 235144 (2017).
[119] T. Iadecola, T. Neupert, C. Chamon, and C. Mudry, Phys. Rev. B 99, 245138 (2019).

Chapter 3

Three-Dimensional Fractional Topological Insulators in Coupled Rashba Layers

Adapted from:
Yanick Volpez, Daniel Loss, and Jelena Klinovaja
"Three-dimensional fractional topological insulators in coupled Rashba layers",
Phys. Rev. B **96**, 085422 (2017).

We propose a model of three-dimensional topological insulators consisting of weakly coupled electron- and hole-gas layers with Rashba spin-orbit interaction stacked along a given axis. We show that in the presence of strong electron-electron interactions the system realizes a fractional strong topological insulator, where the rotational symmetry and condensation energy arguments still allow us to treat the problem as quasi-one-dimensional with bosonization techniques. We also show that if Rashba and Dresselhaus spin-orbit interaction terms are equally strong, by doping the system with magnetic impurities, one can bring it into the Weyl semimetal phase.

3.1 Introduction

In recent years, the study of topological phases of matter has become one of the prominent subjects in condensed matter research. Soon after the theoretical prediction and experimental confirmation of topological band insulators (TIs) in two [1–5] and three dimensions [6–9], it was theoretically shown that the class of topologically non-trivial matter is much larger and the corresponding phases even more exotic once interacting systems are considered that can allow phases hosting gapless excitations with fractional charges or spin quantum numbers [10–12]. The realization of such unconventional phases in Nature is not only of fundamental interest, but also promising for applications such as topological quantum computation, where Fibonacci anyons can serve as qubits which allow for universal quantum computation [13]. However, the basic ingredients for obtaining a Fibonacci phase are parafermions, also called fractional Majorana fermions, which emerge only in the presence of electron-electron interactions. Many proposal for experimental realizations of parafermions rely on a combination of superconductivity and fractional TIs [14–19]. So far, fractional TIs still lack experimental realization and it is thus of great importance searching for models possibly realizable in future experiments.

It is the purpose of this paper to introduce a model which shows how, in principle, a three-dimensional (3D) fractional TI can be engineered. We generalize the approach of weakly coupled wires [20] to three dimensions by considering a stack of weakly coupled two-dimension electron gas (2DEG) layers. Although the coupled wires approach is a very successful method for theoretically constructing two-dimensional (2D) [12, 20–30] and 3D [31–33] topological systems, the coupled layers approach [34] is simpler to handle and is physically more transparent when describing 3D systems. We consider a stack of 2D layers with Rashba spin-orbit

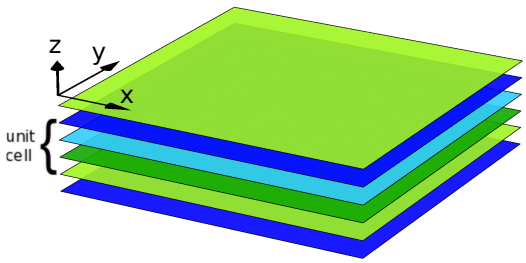

Figure 3.1: Schematic representation of the system formed by tunnel-coupled layers with charge carriers. The unit cell consists of two electron (blue) and two hole (green) layers. The color brightness encodes the two different signs of the SOI.

interaction (SOI) weakly tunnel coupled to each other. Such a system could be realized in a semiconductor superlattice where the 2DEGs form at heterojunctions and the SOI can be controlled with electrical gates [35, 36]. Alternatively, one could realize our setup in a van der Waals heterostructure, by stacking a carefully chosen sequence of different atomically thin layers on top of each other[37–42].

The paper is organized as follows. In Section 3.2 we introduce the system composed of weakly coupled layers. In Section 3.3, we study its properties in the non-interacting regime. We derive the bulk spectrum, discuss the computation of the topological invariant, and show the existence of gapless surface states using analytical and numerical methods. We conclude that the non-interacting model realizes a 3D TI. This sets the stage for the main part of the work presented in Section 3.4 - the fractional topological phase. We identify the regime where the interacting system forms a fractional strong 3D TI [32, 33, 43] in the regime of strong electron-electron interactions. The main idea of the analysis is to search for solutions minimizing the energy of the system, which translates into maximizing the size of the gap opened by backscattering-assisted tunneling processes and should stabilize the system, similar to nesting conditions discussed before in various systems [44–47]. Importantly, the condensation energy gain is maximum for processes that do not break the rotational and translation symmetries of the system [48, 49]. This helps us to reduce the problem effectively to one dimension where we can then use bosonization and Luttinger liquid techniques to show the existence of fractionally charged surface states with a nondegenerate helical Dirac cone spectrum in the topological phase. Additionally, in Section 3.5 we discuss how an equal combination of Rashba and Dresselhaus SOI leads to a Weyl semimetal phase in non-interacting systems. We summarize our results in Section VI.

3.2 Model

We consider a system of weakly coupled 2DEG layers stacked along the z axis with the distance a_z between layers. The unit cell consists of four layers, two of which have an electron-like dispersion and two have a hole-like dispersion, see Fig. 3.1. Each layer has a SOI of Rashba type. The strength of the SOI, α, is the same throughout the unit cell but alternates its sign from layer to layer. We introduce two indices to label the layers: $\eta \in \{1, \bar{1}\}$ and $\tau \in \{1, \bar{1}\}$, which distinguish between electron and hole layers as well as between layers with positive and negative SOI,

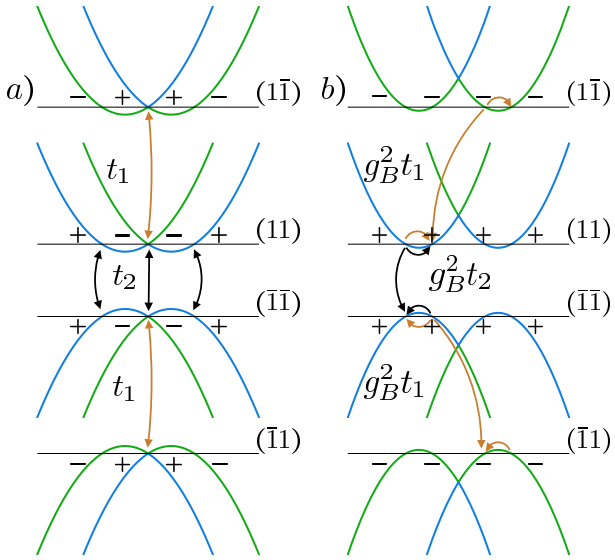

Figure 3.2: Dispersion relation of the layers for a fixed value of θ. (a) The chemical potentials μ (black lines) are tuned to the SOI energy E_{so}. The colors blue/green encode positive/negative helicity. The arrows represent the tunneling processes between fields allowed by spin and momentum conservation laws. (b) The chemical potential is tuned to $E_{so}/9$. In the presence of strong interactions, tunneling processes assisted by backscattering dominate resulting in the bulk gap. The orange and black arrows represent terms in $\mathcal{O}_{t_1}$ and $\mathcal{O}_{t_2}$, respectively [see Eqs. (3.4.1) and (3.4.2)].

respectively. The kinetic part of the Hamiltonian reads

$$H_0 = \sum_{n=1}^{N} \sum_{\eta\tau} \sum_{\sigma\sigma'} \int dxdy\ \Psi^\dagger_{n\eta\tau\sigma} h^0_{\eta\tau\sigma\sigma'} \Psi_{n\eta\tau\sigma'} \tag{3.2.1}$$

$$h^0_{\eta\tau\sigma\sigma'} = \eta\left(-\frac{\hbar^2}{2m}\nabla^2 - \mu\right) - i\tau\alpha(\sigma_1\partial_y - \sigma_2\partial_x)_{\sigma\sigma'}, \tag{3.2.2}$$

where the sum runs over N unit cells and $\Psi_{n\eta\tau\sigma}(x,y)$ is the annihilation operator of an electron in the $(\eta\tau)$ layer of the nth unit cell with spin-projection $\sigma = \pm 1$ at position (x,y). The chemical potential μ is measured from the SOI energy $E_{so} = m\alpha^2/2\hbar^2$ in each layer and has the same magnitude in all layers. The dispersion of the $(\eta\tau)$ layer is given by $E_\pm(k) = \eta\frac{\hbar^2k^2}{2m} \pm \tau\alpha k$ with the eigenstates characterized by spinor $|\eta,\tau,\sigma,\theta\rangle = \left(1, -i\eta\tau\sigma e^{i\theta}\right)^T/\sqrt{2}$, where θ is the angle between the 2D momentum vector $\mathbf{k}$ and the k_x axis.

In the following, we consider spin-conserving tunneling between layers. For a tunneling process of amplitude t_1 (t_2) between layers of the same (opposite) mass

the Hamiltonian is given by

$$H_{t_2} = t_2 \sum_{n\sigma} \int dxdy \left(\Psi^\dagger_{n1\bar{1}\sigma} \Psi_{(n-1)\bar{1}1\sigma} + \Psi^\dagger_{n\bar{1}\bar{1}\sigma} \Psi_{n11\sigma} + \text{H.c.} \right),$$
$$H_{t_1} = t_1 \sum_{n\sigma\eta} \int dxdy \left(\Psi^\dagger_{n\eta 1\sigma} \Psi_{n\eta\bar{1}\sigma} + \text{H.c.} \right). \tag{3.2.3}$$

Without loss of generality, we assume that $t_1, t_2 \geq 0$.

3.3 Three Dimensional Strong Topological Insulator

3.3.1 Bulk Spectrum and Symmetry Class

To begin with, we show that there is a bulk gap at $\mu = 0$ and the symmetry class the Hamiltonian falls into is AII. In order to do so, we first consider an infinite system and introduce momenta $(\boldsymbol{k}, k_z)$. The total Hamiltonian is given by $H = H_0 + H_{t_1} + H_{t_2}$ [see Eqs. (3.2.1)-(3.2.3) and (3.3.3)] with the exact bulk spectrum

$$E^2_\pm(k, k_z) = \epsilon^2 + (\alpha k)^2 + (t_1^2 + t_2^2) \pm 2\sqrt{(\alpha k)^2 \epsilon^2 + t_1^2 \epsilon^2 + t_1^2 t_2^2 \cos^2(k_z a_z/2)}, \tag{3.3.1}$$

where $\epsilon(k) = \hbar^2 k^2/2m$. If $t_1 \neq t_2$ and $t_2 > 0$, the bulk is fully gapped. If $t_1 = t_2 > 0$, the bulk gap closes at $(\boldsymbol{k}, k_z) = (0, 0)$. The system can be tuned into topological $(t_1 > t_2)$ and trivial $(t_2 > t_1)$ phase, as shown below.

In order to discuss the symmetry class of the Hamiltonian we rewrite the total Hamiltonian in terms of Pauli matrices σ_i, η_i, and τ_i acting in spin and layer space, respectively. As a result, we obtain

$$H = \int d\boldsymbol{k} dk_z \ \Psi^\dagger(\mathbf{k}, k_z) h(\mathbf{k}, k_z) \Psi(\mathbf{k}, k_z), \tag{3.3.2}$$

$$h(\mathbf{k}, k_z) = \Big[\frac{\hbar^2 (k_x^2 + k_y^2)}{2m} - \mu \Big] \eta_3 + \alpha \tau_3 (\sigma_1 k_y - \sigma_2 k_x) + t_1 \tau_1 + t_2 \Big[\cos^2(k_z a_z/2) \eta_1 \tau_1 + \sin^2(k_z a_z/2) \eta_2 \tau_2 + \sin(k_z a_z)(\eta_1 \tau_2 + \eta_2 \tau_1)/2 \Big]. \tag{3.3.3}$$

The Hamiltonian is invariant under time reversal operation $\Theta = i\sigma_2 \mathcal{K}$, where $\mathcal{K}$ is the complex conjugation operator. In the Altland-Zirnbauer classification [50, 51] there are three symmetry classes with $\Theta^2 = -1$, two of which have additional particle-hole symmetry. Under particle-hole transformation $\mathcal{C}$ the Bloch Hamiltonian has to satisfy $\mathcal{C} h^T(-\mathbf{k}, -k_z) \mathcal{C}^{-1} = -h(\mathbf{k}, k_z)$. No such operator could be found for $h(\mathbf{k}, k_z)$ [see Eq. (3.3.2)] and it therefore belongs to the AII symmetry

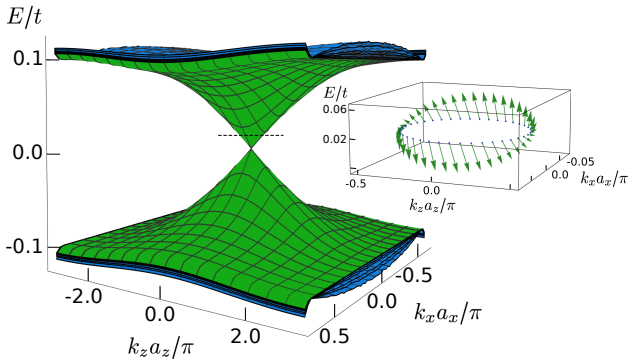

Figure 3.3: The spectrum in the topological phase obtained numerically for $N_y = 300$, $t_1/t = 0.2$, $t_2/t = 0.1$, $\bar{\alpha}/t = 0.3$, see Appendix 3.A. The bulk states (blue) are fully gapped with gap $\Delta_{\min} = 2(t_1 - t_2)$. The dispersion of the surface states localized in the xz plane (green) is represented by an anisotropic Dirac cone. The inset shows the helical spin structure in the layer $\eta = \bar{\tau} = 1$ at $y/a_y = 1$ for $E/t = 0.02$ (dashed line), confirming the presence of a single *helical* Dirac cone at the xz-surface.

class [50, 51]. In three dimensions, the system is classified by a $\mathbb{Z}_2$ invariant and can be a strong topological insulator hosting single helical Dirac cones at each surface [52].

We end this subsection by computing the topological invariant explicitly following Ref. [52]. We derive an effective Hamiltonian by identifying the low-energy bands that close at the phase transition and the level crossing wave vector and then expand the Hamiltonian around these points. From our analysis we know that the topological phase transition takes place at $t_1 = t_2$ and the gap closes at $(\mathbf{k}, k_z) = (0, 0)$. Expanding Eq. (3.3.3) around this momentum point and performing a unitary transformation, the Hamiltonian can be brought into a form consisting of two decoupled 4×4 blocks containing the low-energy and high-energy bands. The low-energy bands undergo the topological phase transition at $t_1 = t_2$. Projecting onto the subspace containing these low-energy bands that close at the critical point, one obtains the effective Hamiltonian given by

$$h_{\text{eff}}(\mathbf{k}, k_z) = \alpha k_x \sigma_2 - \alpha k_y \sigma_1 - \frac{a_z t_2}{2} k_z \eta_2 \sigma_3 + M \eta_1 \sigma_3, \tag{3.3.4}$$

where we introduced the mass $M = t_1 - t_2$. Using this simplified Hamiltonian, one can calculate the $\mathbb{Z}_2$ invariant ν_0 explicitly. We find that $\nu_0 = 1$ ($\nu_0 = 0$) if $M > 0$ ($M < 0$). We note that the same Hamiltonian was studied before in Ref. [53], where it was shown that $h_{\text{eff}}(\mathbf{k}, k_z)$ [Eq. (3.3.4)] corresponds to a 3D strong TI.

3.3.2 Existence of Surface States

The presence of one helical Dirac cone at *any* surface is a central feature of a strong TI. In this subsection, we show the existence of these surface states in the topological regime $t_1 > t_2$ using analytical and numerical methods. First, we prove the existence of surface states on the top and bottom surface of the stack, *i.e.* at the boundaries orthogonal to the stacking direction. To this end, we restrict the discussion to the low-energy regime and perform a linearization of the Hamiltonian by assuming $t_1, t_2 \ll E_{so}$. We represent the momentum in polar coordinates to exploit the rotational symmetry of the layers. Being functions of good quantum numbers, the modulus k and the polar angle θ are constants for k_x and k_y fixed. The spectrum of each layer is isotropic and, therefore, independent of θ, which means that there are only fluctuations in k direction. States with different θ are decoupled from each other, and we can treat the problem as effectively one-dimensional in direction of propagation r [34].

We linearize the spectrum and represent the field operators around the Fermi surface (FS) in terms of slowly varying fermionic field operators $S^{\delta,\beta}_{n\theta\eta\tau}(r)$ [34, 54],

$$\Psi_{n\theta\eta\tau\sigma}(x,y) = \sum_{\delta\beta} \alpha_{\delta\beta\theta\eta\tau\sigma} S^{\delta,\beta}_{n\theta\eta\tau} e^{i\eta\beta k_F^\delta (x\cos\theta + y\sin\theta)}, \tag{3.3.5}$$

where $\delta = e, i$ labels the exterior ($e \equiv 1$) and interior ($i \equiv \bar{1}$) FS, with corresponding Fermi momenta $k_F^e = 2m\alpha/\hbar^2$ and $k_F^i = 0$. Here, $\beta = 1, \bar{1}$ refers to 'right' (1) and 'left' ($\bar{1}$) movers propogating into opposite y directions. In this representation the polar angle θ is restricted to $[0, \pi)$. The spin overlap amplitude is given by $\alpha_{\delta\beta\theta\eta\tau\sigma} = \langle\sigma|\eta, \tau, \delta, \theta + \pi(1-\eta\beta)/2\rangle$. The linearized kinetic term [see Eq. (3.2.1)] becomes $\bar{H}_0 = \int dr\ \bar{\mathcal{H}}_0(r)$ with

$$\bar{\mathcal{H}}_0 = -i\hbar v_F \sum_{n=1}^{N} \sum_{\theta\eta\tau} \sum_{\delta\beta} \beta (S^{\delta,\beta}_{n\theta\eta\tau})^\dagger (\partial_r S^{\delta,\beta}_{n\theta\eta\tau}), \tag{3.3.6}$$

where $v_F = \alpha/\hbar$ is the Fermi velocity.

We next employ a two-step perturbation approach by considering the regime $t_1 \gg t_2$ [29]. We first take into account the t_1 tunnelings and obtain after linearization,

$$\bar{\mathcal{H}}_{t_1} = t_1 \sum_{n=1}^{N} \sum_{\theta\eta\beta} \Big[(S^{i,\beta}_{n\theta\eta 1})^\dagger S^{i,\bar{\beta}}_{n\theta\eta\bar{1}} + \text{H.c.} \Big]. \tag{3.3.7}$$

Importantly, $\bar{\mathcal{H}}_{t_1}$ couples fields of opposite velocities at $\boldsymbol{k} = 0$ resulting in a partial gap [see also Fig. 3.2a]. In a next step, we take into account the fields that are unaffected by the t_1-term and neglect the already gapped fields. Analogously, one

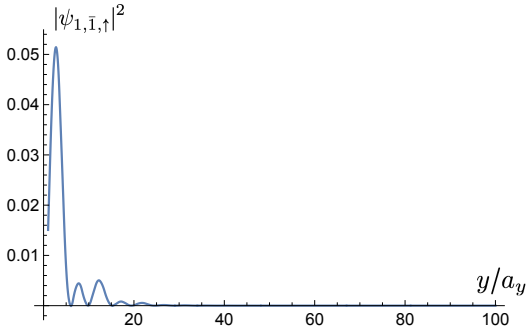

Figure 3.4: The probability density of the wavefunction $|\psi_{1,\bar{1},\uparrow}|^2$ in the $(1,\bar{1})$ layer for a state on the Dirac cone on the first one hundred sites ($N_y = 800$) along y direction. The figure was obtained for $t_1/t = 0.2$, $t_2/t = 0.1$, $\bar{\alpha}/t = 0.3$, and $\mu = -4t$ for a state on the Dirac cone with $k_x a_x/\pi = 0.05$ and $k_z a_z/\pi = 0$. The wavefunction is localized at the xz surface decaying rapidly along y direction into the bulk.

obtains

$$\bar{\mathcal{H}}_{t_2} = t_2 \sum_{\theta\beta} \Big[\sum_{n=2}^{N} (S^{e,\beta}_{n\theta 1\bar{1}})^\dagger S^{e,\bar{\beta}}_{(n-1)\theta\bar{1}1} + \sum_{n=1}^{N} (S^{e,\beta}_{n\theta\bar{1}\bar{1}})^\dagger S^{e,\bar{\beta}}_{n\theta 11} + \text{H.c.} \Big]. \tag{3.3.8}$$

These terms gap out the remaining fields in the bulk but do not affect the two fields at the top, $S^{e,1/\bar{1}}_{1\theta 1\bar{1}}$, and at the bottom, $S^{e,1/\bar{1}}_{N\theta\bar{1}1}$, of the stack, since they do not appear in Eq. (3.3.8). These surface states are gapless, have a linear dispersion, and the spin of each state is locked to be orthogonal to its momentum; in other words, they form a single helical Dirac cone at each of the two surfaces. We remark that starting the perturbative analysis in the opposite regime $t_2 \gg t_1$ all fields at the top and bottom surfaces are gapped and the system is in the trivial insulating state. The result obtained in the perturbative regimes smoothly connects to the region of the phase diagram where $t_1 > t_2$, and due to their topological nature the gapless surface states persist over the whole parameter range, see Fig. 3.3.

To access the spectrum of the, say, xz surface at $y = 0$, we employ numerical diagonalization (see Appendix 3.A for more details) and consider the system finite in y direction with N_y lattice sites. The spectrum of the tight-binding Hamiltonian [see Eq. (3.A.1)] in the topological phase is shown in Fig. 3.3. It can be seen that the bulk states are separated by an energy gap and that there exist states with a Dirac spectrum. In Fig. 3.4, we show the modulus squared of the wavefunction of a state on the Dirac cone on the first hundred lattice sites. One can observe that, indeed, the state is localized at the surface of the system and therefore conclude that the Dirac cone corresponds to surface states on xz surface. The spin is locked to the momentum resulting in a helical texture [see the inset in Fig. 3.3]. Since the system has rotational symmetry around the z axis, it is clear that the same

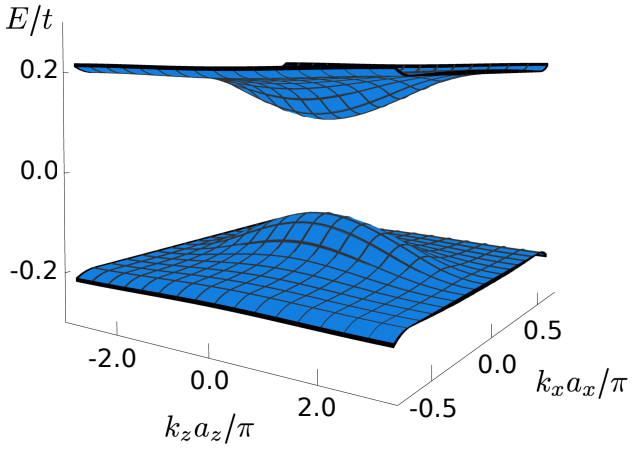

Figure 3.5: The spectrum in the trivial phase obtained numerically for $N_y = 300$, $t_1/t = 0.1$, $t_2/t = 0.2$, $\bar{\alpha}/t = 0.3$. The spectrum is fully gapped and no surface states were found in the xz plane. The same holds for all other surfaces, which shows that here the system is in the trivial phase.

conclusions could be drawn if we had imposed a hard wall boundary condition at $x = 0$. In conclusion, we showed the existence of a single helical Dirac cone on each boundary and a fully gapped bulk spectrum in the regime $t_1 > t_2$. We emphasize that the gapless surface states were obtained in a nonperturbative regime which proves that their existence does not rely on the perturbative approach considered above, underlining their topological nature.

For completeness we also show the spectrum in the region $t_1 < t_2$ which is separated by the gap closing line $t_1 = t_2$ from the region where we found the Dirac cone. As can be seen in Fig. 3.5 the spectrum is fully gapped and there are no surface states. The system is a trivial insulator in the whole region where $t_1 < t_2$. This analysis confirms that for $t_1 > t_2$ ($t_1 < t_2$), the strong topological $\mathbb{Z}_2$ invariant ν_0 is given by $\nu_0 = 1$ ($\nu_0 = 0$), which is consistent with our analysis above.

To emphasize the topological origin of surface states, we show their stability against nonmagnetic disorder. In order to do so, we modified our tight-binding model to implement detuning of the chemical potential in the (η,τ) layer at lattice site i by $\delta\mu_{\eta\tau i}$. The perturbations were randomly generated from a normal distribution centered at $\langle\delta\mu\rangle = 0$ and the variance characterizing the disorder strength was chosen such that $\sqrt{\langle\delta\mu^2\rangle} < t_2$. As can be seen from Fig. 3.6, the surface states remain intact in the presence of non-magnetic disorder. There is no gap opening. Moreover, this analysis also confirms that our initial assumption of the rotational and translational symmetries is not crucial for the existence of the topological phase.

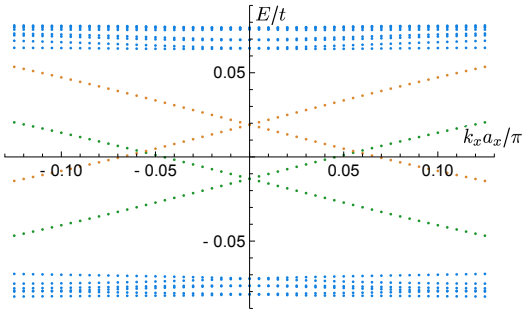

Figure 3.6: The spectrum of the topological phase in the presence of disorder along the cut $k_z a_z/\pi = 0$ with parameters $N_y = 300$, $t_1/t = 0.2$, $t_2/t = 0.1$, $\bar{\alpha}/t = 0.3$, $\mu = -4t$, and $\sqrt{\langle \delta\mu^2 \rangle} = 0.7t_2$. The two Dirac cones on two opposite surfaces (green and orange) still exist and there is no gap opened by disorder. However, due to slightly different disorder configurations at two surfaces, there is a small shift of the position of the center of the Dirac cone in energy.

3.4 Fractional Topological Insulator

Next, our goal is to identify the regime in which the system is a fractional strong 3D TI. For this, we detune the chemical potential in H_0 [see Eq. (3.2.2)] to $\mu_{1/3} = E_{so}/9$. This particular choice of μ fixes the ratio between the radii of the interior and exterior FS to $2k_F^i = k_F^e = 4m\alpha/3\hbar^2$. We, again, restrict the discussion to the regime $t_1 \gg t_2$ and treat the t_1-terms first. The direct tunneling (t_1) between layers of the same mass is forbidden by spin/momentum conservation and does not result in a gap. Repulsive electron-electron interactions, however, open the channel for backscattering assisted tunneling which has a chance to open a gap. These processes consist of a tunneling with nonzero momentum transfer which is accompanied by two backscattering events (in leading order) ensuring overall momentum conservation. If the tunneling occurs between two states where the spins are misaligned, the tunneling amplitude gets suppressed by a factor of the spin overlap [see Fig. 3.7].

Thus, we only take into account events where the tunneling amplitude and correspondingly the size of the bulk gap becomes maximal [44–47], which corresponds to processes preserving the rotational and translational symmetries of the system and do not mix states characterized by different values of θ [47–49], see Fig. 3.2b. Such processes similar to nesting conditions on Fermi surfaces [44–47] allow us to maximize the condensation energy gain (also known as Peierls-type energy gain) and stabilize the topological phase [44–47]. If the chemical potential is detuned by $\delta\mu$, the tunneling no longer conserves momentum exactly. However, the gap is still opened, although suppressed, if $\delta\mu < t_1, t_2$.

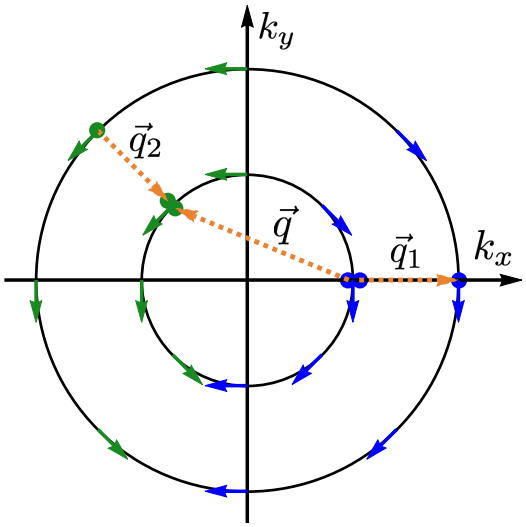

Figure 3.7: Schematics of backscattering assisted tunneling process between two neighboring electron layers. The two Fermi surfaces are drawn on top of each other. For brevity, the spin polarizations of the corresponding state at the Fermi surface for the first (green arrows) and second layer (blue arrows) is indicated only for $k_x < 0$ ($k_x > 0$). The involved electrons residing in the respective layers are shown by blue (green) dots. The momentum transfer $\vec{q}$ (orange dotted arrows) during the tunneling event is compensated by the two backscattering processes such that $\vec{q} + \vec{q}_1 + \vec{q}_2 = 0$. Correspondingly, due to the spin structure of the Fermi surface, the amplitude of the tunneling process with momentum transfer $\vec{q}$ connecting two states with misaligned spins is reduced. The backscattering assisted tunneling amplitude (and thus the resulting bulk gap) is maximum if all involved spins are aligned, thus, $\vec{q} \parallel \vec{q}_{1,2}$. In this case, the rotation symmetry of the system is preserved.

The Hamiltonian density describing tunneling between layers of the same mass becomes [see also Fig. 3.2b]

$$\mathcal{O}_{t_1} = g_1 \sum_{n\theta\eta\tau} \big[(S^{e,1}_{n\theta\eta\bar{\tau}})^\dagger S^{i,\bar{1}}_{n\theta\eta\bar{\tau}} (S^{i,1}_{n\theta\eta\tau})^\dagger S^{i,\bar{1}}_{n\theta\eta\bar{\tau}} (S^{i,1}_{n\theta\eta\tau})^\dagger S^{e,\bar{1}}_{n\theta\eta\tau} + \text{H.c.} \big], \tag{3.4.1}$$

with $g_1 = t_1 g_B^2$ and g_B being the strength of the backscattering term due to interactions. For the t_2 processes we distinguish the cases where tunneling occurs between the interior (exterior) FSs. The operator that commutes with the one in Eq. (3.4.1) is given in leading order by

$$\begin{aligned} \mathcal{O}_{t_2} = g_2 \sum_{\substack{n\theta \\ l\in\{1,\bar{1}\}}} \big[& (S^{e,1}_{n\theta l l})^\dagger S^{i,\bar{1}}_{n\theta l l} (S^{e,1}_{n\theta l l})^\dagger S^{e,\bar{1}}_{n\theta l\bar{l}} (S^{i,1}_{n\theta l\bar{l}})^\dagger S^{e,\bar{1}}_{n\theta l\bar{l}} \\ & + (S^{e,1}_{n_l\theta l\bar{l}})^\dagger S^{i,\bar{1}}_{n_l\theta l\bar{l}} (S^{e,1}_{n_l\theta l\bar{l}})^\dagger S^{e,\bar{1}}_{\bar{n}_l\theta l\bar{l}} (S^{i,1}_{\bar{n}_l\theta l\bar{l}})^\dagger S^{e,\bar{1}}_{\bar{n}_l\theta l\bar{l}} + \text{H.c.} \big], \end{aligned} \tag{3.4.2}$$

with $g_2 = t_2 g_B^2$ and where tunneling occurs between the exterior FSs. For brevity we use the index-dependent unit cell labels $n_l = n - (1-l)/2$ and $\bar{n}_l = n - (1+l)/2$.

For completeness we give the expression for the second operator describing t_2 tunneling processes between the interior FS of layers with opposite mass

$$\begin{aligned}\tilde{\mathcal{O}}_{t_2} = g_2 \sum_{\substack{n\theta \\ l\in\{1,\bar{1}\}}} \big[&(S^{e,1}_{n\theta ll})^\dagger S^{i,\bar{1}}_{n\theta ll} (S^{i,1}_{n\theta l\bar{l}})^\dagger S^{i,\bar{1}}_{n\theta ll} (S^{i,1}_{n\theta l\bar{l}})^\dagger S^{e,\bar{1}}_{n\theta l\bar{l}} \\ &+ (S^{e,1}_{n_l\theta l\bar{l}})^\dagger S^{i,\bar{1}}_{n_l\theta l\bar{l}} (S^{i,1}_{\bar{n}_l\theta\bar{l}})^\dagger S^{i,\bar{1}}_{n_l\theta l\bar{l}} (S^{i,1}_{\bar{n}_l\theta\bar{l}})^\dagger S^{e,\bar{1}}_{\bar{n}_l\theta\bar{l}} + \text{H.c.}\big], \end{aligned} \tag{3.4.3}$$

with n_l and $\bar{n}_l$ as above. While $\mathcal{O}_{t_1}$ and $\mathcal{O}_{t_2}$ commute, $\tilde{\mathcal{O}}_{t_2}$ does not commute with $\mathcal{O}_{t_1}$ and therefore these operators can not be diagonalized simultaneously. Thus, they leave the system gapless and, consequentially, do not result in an energy gain. Such terms can therefore be dropped.

The terms $\mathcal{O}_{t_1}$ and $\mathcal{O}_{t_2}$ open a gap in the bulk spectrum but in order to access the nature of the gapless surface states we employ the bosonization procedure for 1D systems. This is justified since in the limit of dominant tunneling, fields with different angles θ are not coupled [cf. Eqs. (3.4.1) and (3.4.2)]. Thus, for θ fixed, the problem is equivalent to tunnel-coupled infinite wires.

We next introduce chiral bosonic fields $\phi^{(\theta)}_{n\beta\eta\tau\sigma}(r)$ ($S^{\delta,\beta}_{n\theta\eta\tau} \sim e^{i\phi^{(\theta)}_{n\beta\eta\tau\sigma}}$), where β determines the chirality and σ the spin projection [55]. The chiral fields satisfy the commutation relation $\left[\phi^{(\theta)}_{n\beta\eta\tau\sigma}(r), \phi^{(\theta)}_{n\beta\eta\tau\sigma}(r')\right] = i\pi\beta\,\text{sgn}(r-r')$ and all other commutators vanish. In a more convenient basis defined as $\eta^{(\theta)}_{n\beta\eta\tau\sigma} = 2\phi^{(\theta)}_{n\beta\eta\tau\sigma} - \phi^{(\theta)}_{n\bar{\beta}\eta\tau\sigma}$, the above interaction terms become

$$\begin{aligned}\mathcal{O}_{t_2} &= g_2 \sum_{\substack{\theta \\ l\in\{1,\bar{1}\}}} \left[\sum_{n=1}^{N} \cos(\eta^{(\theta)}_{n1ll} - \eta^{(\theta)}_{n\bar{1}\bar{l}\bar{l}l}) + \sum_{n=2}^{N} \cos(\eta^{(\theta)}_{n_l 1 l\bar{l}} - \eta^{(\theta)}_{\bar{n}_l\bar{1}\bar{l}l}) \right], \\ \mathcal{O}_{t_1} &= g_1 \sum_{n\theta\eta\tau} \cos(\eta^{(\theta)}_{n\bar{1}\eta\bar{\tau}\bar{\tau}} - \eta^{(\theta)}_{n1\eta\tau\bar{\tau}}). \end{aligned} \tag{3.4.4}$$

We work in the limit where g_i are large compared to the quadratic part of the Hamiltonian and the fields get pinned to one of the minima of the cosines [55]. Using Eqs. (3.4.4), we infer that all the fields in the bulk get pinned pairwise and, therefore, the bulk spectrum is fully gapped. However, as in the previous section, two fields at the top surface and two fields at the bottom surface do not appear in the tunneling terms, namely $\eta^{(\theta)}_{1,\bar{1}1\bar{1}\uparrow}$, $\eta^{(\theta)}_{1,11\bar{1}\downarrow}$, $\eta^{(\theta)}_{N,1\bar{1}1\uparrow}$, and $\eta^{(\theta)}_{N,\bar{1}\bar{1}1\downarrow}$. These fields do not get pinned and stay gapless [24]. We conclude that the interacting system hosts gapless surface states that have their spin locked orthogonal to their momentum. The quasi-particle excitations on the surface are directly given by the

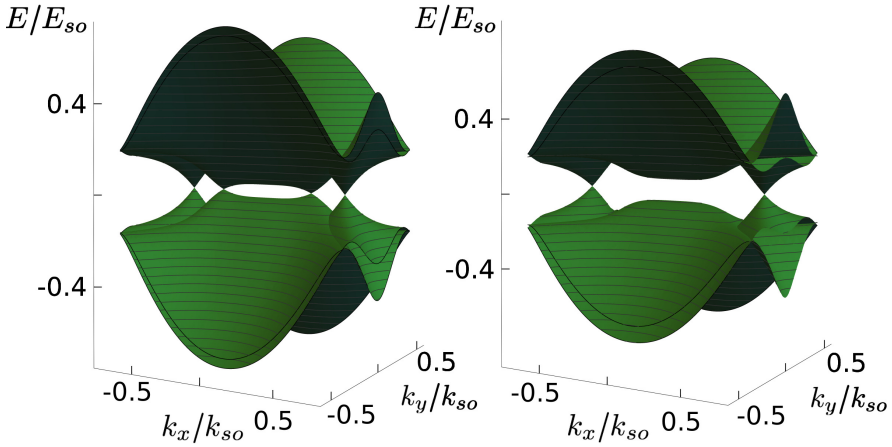

Figure 3.8: The Weyl semimetal spectrum for the parameters $t_1/E_{so} = 0.3$, $t_2/E_{so} = 0.19$, and $k_z = 0$. Left: Four Weyl nodes exist for weak exchange interaction ($J/E_{so} = 0.08$). Right: In the regime $|J - t_1| < t_2$, only two Weyl outer nodes remain ($J/E_{so} = 0.17$).

exponential of the gapless bosonic fields listed above. These excitations have been shown [56] to carry fractional charge $q = e/3$. This procedure can be generalized to other odd integers $n > 3$ to obtain fractional TIs with $q = e/n$.

3.5 Weyl Semimetal Phase

Remarkably, if the SOI is no longer of pure Rashba type but given by an equal combination of Rashba and Dresselhaus SOI by gate tuning [35], such that the spin gets coupled only to the momentum in one particular direction [57–64], a Weyl semimetal phase (WSM) can be realized in the same setup. The modified SOI term reads

$$\tilde{H}_{\mathrm{SOI}} = -i\alpha \sum_{n\eta\tau} \sum_{\sigma\sigma'} \int dxdy\ \Psi^{\dagger}_{n\eta\tau\sigma} \tau (\sigma_1)_{\sigma\sigma'} \partial_y \Psi_{n\eta\tau\sigma'}. \tag{3.5.1}$$

As a result, the Hamiltonian density for each $\eta\tau$ layer is given by

$$\tilde{\mathcal{H}}_0(x,y) = \sum_{\substack{n\eta\tau \\ \sigma\sigma'}} \Psi^{\dagger}_{n\eta\tau\sigma} \Big[\eta \left(-\frac{\hbar^2}{2m} \nabla^2 - \mu \right) - i\tau\alpha\sigma_1 \partial_y \Big]_{\sigma\sigma'} \Psi_{n\eta\tau\sigma'}. \tag{3.5.2}$$

In Refs. [57–63] it was shown that combining Rashba and Dresselhaus SOI in a 2DEG can lead to a partial compensation of the two. The above term arises when Rashba and Dresselhaus SOI are of equal strength. The tunneling part of the total Hamiltonian $H_{t_1} + H_{t_2}$ remains the same. From the above equation it is evident, that spin projection along the x-axis is a good quantum number $\sigma = \pm 1$. The total

8×8 Bloch Hamiltonian is block diagonal and can be written in terms of Pauli matrices as

$$\begin{aligned}\tilde{h}(\mathbf{k}) = &\frac{\hbar^2(k_x^2+k_y^2)}{2m}\eta_3 - \alpha k_y \sigma_1\tau_3 + t_1\tau_1 \\ &+ t_2\Big[\cos^2(k_z a_z/2)\eta_1\tau_1 + \sin^2(k_z a_z/2)\eta_2\tau_2 \\ &\quad + \sin(k_z a_z)(\eta_1\tau_2 + \eta_2\tau_1)/2\Big]. \end{aligned} \tag{3.5.3}$$

From now on $\boldsymbol{k}$ denotes the 3D momentum and $\boldsymbol{k}_\parallel$ the in-plane momentum. The energy spectrum of this Hamiltonian is found to be

$$\begin{aligned}\tilde{E}_\pm^2 = &\epsilon_\parallel^2 + t_1^2 + t_2^2 + (\alpha k_y)^2 \\ &\pm 2\sqrt{\epsilon_\parallel^2[t_1^2 + (\alpha k_y)^2] + t_1^2 t_2^2 \cos^2(k_z a_z/2)}, \end{aligned} \tag{3.5.4}$$

with $\epsilon_\parallel = \hbar^2 k_\parallel^2/2m$. If $t_1 < t_2$, the spectrum has a bulk gap. For $t_1 > t_2$ there are two doubly degenerate gapless bulk states at $\pm\mathbf{k}_D$ with $\mathbf{k}_D = (k_x^*, 0, 0)$ and $k_x^* = \sqrt{\frac{2m}{\hbar^2}}(t_1^2 - t_2^2)^{1/4}$. These are Dirac nodes hosting two Weyl nodes of opposite chirality at the same point. The two Weyl nodes are not coupled in the absence of disorder and, therefore, do not annihilate each other. Such Dirac nodes can, however, be stable only if additional crystal symmetries are present that stabilize these nodes [65].

Next, we would like to eliminate the twofold degeneracy of the Dirac node by splitting it into two Weyl nodes. This can be achieved if the time-reversal symmetry is broken, for example, via magnetic impurities which order ferromagnetically (FM) along a direction orthogonal to the SOI direction, say, in the y direction [66–69]. The exchange interaction between the electron spins and the magnetic impurities reads,

$$H_J = -J \sum_{n\eta\tau} \sum_{\sigma\sigma'} \int d^3x \; \Psi^\dagger_{n\eta\tau\sigma}(\sigma_2)_{\sigma\sigma'}\Psi_{n\eta\tau\sigma'}, \tag{3.5.5}$$

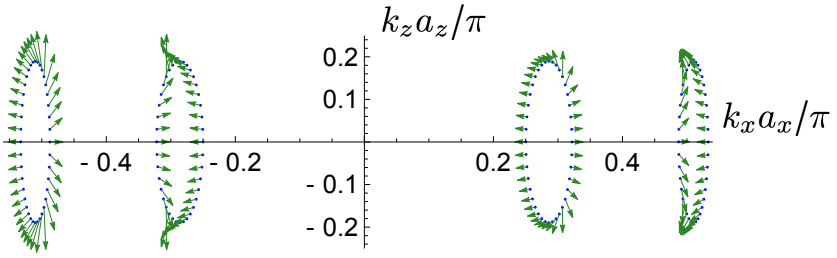

Figure 3.9: Spin structure of the states on the Weyl cones at an energy of $E/t = 0.02$ at $y/a_y = 260$ ($N_y = 400$). For clarity we projected the spin onto the $k_x k_z$ plane. The parameters used for the numerics are $t_1/t = 0.2$, $t_2/t = 0.1$, $\bar{\alpha}/t = 0.4$, and $J/t = 0.07$.

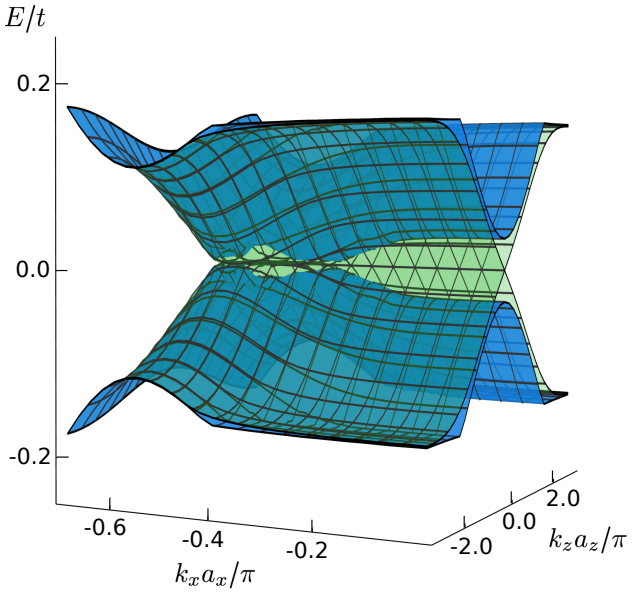

Figure 3.10: Spectrum in the Weyl semimetal phase in half of the BZ as a function of momenta (k_x, k_z). The spectrum of semi-infinite system ($y > 0$) was obtained numerically [cf. Eq. (3.A.5)] for $N_y = 800$, $\bar{\alpha}/t = 0.45$, $t_1/t = 0.3$, $t_2/t = 0.19$, and $J/t = 0.08$, *i.e.* in the regime $J < t_1 - t_2$ where we expect four Weyl nodes from the analytical anlaysis. The bulk (surface) states are colored in blue (green). The spectrum is cut in half along the line connecting the gap closing points. The spectrum indeed features two (since we show only one half) gapless points as well as the Fermi arcs.

with $J > 0$. Gapless states only exist in the $k_z = 0$ plane where the spectrum is given by

$$\tilde{E}_{\pm,\pm,}(k_x, k_y, 0) = \epsilon_{\parallel}^2 + (J \pm t_1)^2 + t_2^2 + (\alpha k_y)^2 \pm 2\sqrt{(\epsilon_{\parallel}^2 + t_2^2)(J \pm t_1)^2 + \epsilon_{\parallel}^2 (\alpha k_y)^2}. \tag{3.5.6}$$

If $|J - t_1| > t_2$ the bulk spectrum has four gapless states at $\pm\mathbf{k}_{\pm}$ with $\mathbf{k}_{\pm} = (k^*_{x,\pm}, 0, 0)$ and $k^*_{x,\pm} = \sqrt{\frac{2m}{\hbar^2}}\Big[(J \pm t_1)^2 - t_2^2\Big]^{1/4}$. This means that the initial twofold degeneracy gets lifted and we end up with four distinct nodes [see Fig. 3.8]. The nodes at $\mathbf{k}_{\pm}$ and $-\mathbf{k}_{\pm}$ have opposite chirality [see Fig. 3.9]. If the exchange interaction strength is tuned to $J = t_1 - t_2$, the two inner nodes meet and annihilate. As long as $|J - t_1| < t_2$, only the nodes at $\pm\mathbf{k}_{+}$ exist, while at $J = t_1 + t_2$ the two inner nodes reappear and separate when J is increased further.

In the Appendix 3.B, we find explicitly the spectrum and the wavefunctions of surface states in the WSM phase. Here, we present the numerical spectrum obtained from a tight-binding model defined in Appendix 3.A with polarized mag-

netic impurities in the regime $J < t_1 - t_2$; see Fig. 3.10. We confirm the existence of gapless bulk states and of surface states that are dispersionless in x direction. The surface states have a linear dispersion in the z direction as expected. In order to check the chirality of the Weyl nodes, we also access the spin structure of the states on the Weyl cones; see Fig. 3.9. Indeed, the overall chirality of four Weyl cones is zero. We note that the Weyl phase is defined strictly at the absence of disorder. Strictly speaking, any finite amount of disorder will scatter between Weyl cones as discussed in literature [66]. However, if the typical disorder correlation length is much smaller than the Fermi wavelength, the disorder effects will be averaged out in leading order such that the Weyl cones still can be observed.

3.6 Conclusions

We considered a layered system that realizes a 3D fractional strong TI. We constructed a simple model that solely consists of weakly coupled 2D layers with Rashba SOI. We also show that if Dresselhaus and Rashba SOI term are of the same strength, the system can be brought into the Weyl semimetal phase. The motivation for such setups is given by the vast progress in fabricating superlattices and van der Waals heterostructures. We believe that these engineered materials provide a promising route towards realizing 3D (fractional) TIs and Weyl semimetals as proposed in this work.

Acknowledgements

We acknowledge support from the Swiss National Science Foundation and NCCR QSIT, and the Marie Sklodowska-Curie Innovative Training Network (ITN-ETN) Spin-NANO.

3.A Tight-Binding Models

In Sect. 3.3, we address the question of whether a helical Dirac cone exists at any boundary numerically by implementing a tight-binding model [34] for a system with N_y lattice sites. We impose a hard wall boundary at $y = 0$ and consider the system to be infinitely extended along the x and z directions such that we can introduce momenta k_x and k_z. The tight-binding Hamiltonian $H = \sum_{k_x k_z} H_{k_x k_z}$ for this setup reads

$$H_{k_x k_z} = \sum_{\eta\tau} H_{0k_x k_z \eta\tau} + \sum_{i=1,2} H_{t_i k_x k_z}, \tag{3.A.1}$$

$$\begin{aligned} H_{0k_x k_z \eta\tau} = &-\sum_{n\sigma}\Big[\eta\left(t\cos(k_x a_x) - \mu/2\right) c^\dagger_{\eta\tau n\sigma} c_{\eta\tau n\sigma} + \eta t c^\dagger_{\eta\tau(n+1)\sigma} c_{\eta\tau n\sigma}\Big] \\ &+ \tau\tilde{\alpha}\sum_n \Big[i(c^\dagger_{\eta\tau(n+1)\uparrow} c_{\eta\tau n\downarrow} - c^\dagger_{\eta\tau(n-1)\uparrow} c_{\eta\tau n\downarrow}) + 2i\sin(k_x a_x) c^\dagger_{\eta\tau n\uparrow} c_{\eta\tau n\downarrow}\Big] + \text{H.c.}, \end{aligned} \tag{3.A.2}$$

$$H_{t_1 k_x k_z} = t_1 \sum_{n\sigma}\Big[c^\dagger_{1\bar{1}n\sigma} c_{11n\sigma} + c^\dagger_{\bar{1}\bar{1}n\sigma} c_{\bar{1}1n\sigma} + \text{H.c.}\Big], \tag{3.A.3}$$

$$H_{t_2 k_x k_z} = t_2 \sum_{n\sigma}\Big[e^{-ik_z a_z} c^\dagger_{\bar{1}1n\sigma} c_{1\bar{1}n\sigma} + c^\dagger_{11n\sigma} c_{\bar{1}\bar{1}n\sigma} + \text{H.c.}\Big]. \tag{3.A.4}$$

Here, $c_{\eta\tau n\sigma} \equiv c_{\eta\tau n\sigma k_x k_y}$ is the annihilation operator for an electron with spin σ in the layer $(\eta\tau)$ with momentum (k_x, k_z) at position $y = na_y$, where a_y is the lattice constant along the y direction. The spin-flip hopping amplitude is related to the SOI parameter by $\tilde{\alpha} = \alpha/2a_y$ (we take the lattice constants $a_x = a_y$) [70].

To describe the Weyl phase in Sect. 3.5, we use the same Hamiltonian as in Eq. (3.A.1) besides adding exchange interaction term and modifying the SOI term, such as

$$\begin{aligned} \tilde{H}_{0k_x k_z \eta\tau} = &-\sum_{n\sigma}\Big[\eta\left(t\cos(k_x a_x) - \mu/2\right) c^\dagger_{\eta\tau n\sigma} c_{\eta\tau n\sigma} + \eta t c^\dagger_{\eta\tau(n+1)\sigma} c_{\eta\tau n\sigma}\Big] \\ &+ i\tau\tilde{\alpha}\sum_n \Big[c^\dagger_{\eta\tau(n+1)\uparrow} c_{\eta\tau n\downarrow} - c^\dagger_{\eta\tau(n-1)\uparrow} c_{\eta\tau n\downarrow}\Big] - iJ\sum_n c^\dagger_{\eta\tau n\uparrow} c_{\eta\tau n\downarrow} + \text{H.c.}, \end{aligned} \tag{3.A.5}$$

with the magnetic impurities of the strength J polarized along y direction.

3.B Analytical Calculation of Surface States in Weyl Semimetal Phase

In this appendix we explicitly show the analytical calculation of the surface states that appear in the WSM phase. We restrict the discussion to the regime where $t_1 - t_2 < J < t_1 + t_2$ with $t_1 > t_2$. Without loss of generality all three parameters are considered to be positive. In this range of the exchange interaction strength there exist two Weyl nodes at $\pm\mathbf{k}_+$ (see above) and the associated Fermi arcs are located on the xz and xy surface BZ. For simplicity we calculate the surface states on the xz surface for $y = 0$. In order to perform the linearization of the Hamiltonian [see Eq. (3.5.3)] we again assume $t_1, t_2 \ll E_{so}$ (see also text above). The chemical potential is tuned to the Weyl nodes.

We start with the full 3D bulk Hamiltonian $\tilde{h}(k_x, k_y, k_z)$. Since the Fermi arc is the line connecting the projections of the Weyl nodes on the corresponding surface

BZ, it is clear that the surface states occur with $(k_x, 0)$ in the $k_x k_z$ plane. Before linearization the Hamiltonian reads

$$\tilde{h}(k_x, k_y, 0) = \frac{\hbar^2}{2m}(k_x^2 + k_y^2)\eta_3 - \alpha k_y \tau_3 \sigma_3 + t_1 \tau_1 + t_2 \eta_1 \tau_1 + J\sigma_2. \tag{3.B.1}$$

For a clean surface (k_x, k_z) are good quantum numbers and we can solve Eq. (3.B.1) for fixed k_x, k_z, *i.e.* the problem reduces to a one-dimensional problem solving for the zero-energy eigenstates of $\tilde{h}_{k_x}(k_y \to -i\partial_y)$ (k_z is fixed to zero). Since k_x is fixed in Eq. (3.B.1) we treat the term containing k_x as a detuning of the chemical potential from the spin-orbit energy. This procedure is justified since $k_x^2 \in [0, \frac{2m}{\hbar^2}\sqrt{(J+t_1)^2 - t_2^2}]$ and therefore k_x^2 is bounded from above by $k_x^2 < \frac{4\sqrt{2}m}{\hbar^2} t_1$. This yields $\delta\mu_{k_x} = \frac{\hbar^2 k_x^2}{2m} < 4\sqrt{2} t_1 \ll E_{so}$ in the perturbative regime t_1, $t_2 \ll E_{so}$. Linearizing the Hamiltonian in Eq. (3.B.1) gives

$$\begin{aligned}\tilde{h} = v_F \hat{k}\gamma_3 + t_1(\tau_1\gamma_1 - \tau_2\gamma_2)/2 + t_2\eta_1\tau_1\gamma_1 \\ + J(\sigma_2\gamma_1 + \sigma_1\tau_3\gamma_2)/2 + \delta\mu_{k_x}\eta_3,\end{aligned} \tag{3.B.2}$$

with $\hat{k} = -i\hbar\partial_y$ the momentum operator around the Fermi points and γ_i acts in left/right mover space. The effect of spin-orbit coupling enters in two ways, firstly it determines the Fermi velocity (since $v_F = \alpha/\hbar$) and secondly it prevents the exchange interaction term from being diagonal in spin space, which would otherwise just lead to an energy shift of the two spin subbands and not produce any interesting effects. For the eigenstate we make the Ansatz $\psi_{k_x}(x, y, z) = e^{ik_x x}\psi(y) = e^{ik_x x} e^{i\lambda y}\phi_\lambda$, where ϕ_λ is a 16-component vector. Acting with the Hamiltonian in Eq. (3.B.2) on ψ_{k_x} one ends up with the matrix equation

$$\tilde{h}(k_x, \partial_y \to i\lambda)\phi_\lambda = E_\lambda \phi_\lambda. \tag{3.B.3}$$

The surface states are the zero-energy eigenstates which decay for $y > 0$ (this translates into the criterion $\mathrm{Re}(i\lambda) < 0$). The zero-energy states can simply be found by solving $\mathrm{Det}(\tilde{h}(k_x, i\lambda)) = 0$. In the regime $t_1 - t_2 < J < t_1 + t_2$ we find the following decaying solutions characterized by

$$\lambda_{1,\pm} = \frac{it_2 \pm \delta\mu_{k_x}}{\hbar v_F}, \tag{3.B.4}$$

$$\lambda_{2,\rho,\kappa} = \rho^{1-\kappa} i \frac{\sqrt{(J + \rho t_1)^2 - \delta\mu_{k_x}^2} + \kappa t_2}{\hbar v_F}, \tag{3.B.5}$$

where $\rho, \kappa \in \{-1, 1\}$ and the corresponding eigenvectors (suppressing the normalization factors) are given by

$$\begin{aligned}
\phi_1 &= (0,0,0,0,0,0,0,0,i,0,0,0,0,0,0,1),\\
\phi_2 &= (0,0,i,0,0,1,0,0,0,0,0,0,0,0,0,0),\\
\phi_3 &= (0,0,0,0,0,0,0,0,0,0,0,-i,1,0,0,0),\\
\phi_4 &= (0,-i,0,0,0,0,1,0,0,0,0,0,0,0,0,0),\\
\phi_5 &= (ig_-^*,0,0,i,-1,0,0,g_-^*,0,-i,-ig_-^*,0,0,-g_-^*,1,0),\\
\phi_6 &= (ig_-,0,0,i,-1,0,0,g_-,0,-i,-ig_-,0,0,-g_-,1,0),\\
\phi_7 &= (-ig_+,0,0,i,1,0,0,g_+,0,i,-ig_+,0,0,g_+,1,0),\\
\phi_8 &= (ig_+,0,0,-i,1,0,0,g_+,0,-i,ig_+,0,0,g_+,1,0),
\end{aligned} \tag{3.B.6}$$

with $g_\pm = \frac{\delta\mu_{k_x} - i\sqrt{(J\pm t_1)^2 - \delta\mu_{k_x}^2}}{J\pm t_1}$. Some of these solutions seem to be ill-defined at $J = t_1$, but they actually have a finite limit once they are normalized. However, the expressions are too lengthy to be displayed here.
We write the general solution as linear combination in the basis

$$\Psi = (\Psi_{1\bar{1}\uparrow}, \Psi_{11\uparrow}, \Psi_{\bar{1}\bar{1}\uparrow}, \Psi_{\bar{1}1\uparrow}, \Psi_{1\bar{1}\downarrow}, \Psi_{11\downarrow}, \Psi_{\bar{1}\bar{1}\downarrow}, \Psi_{\bar{1}1\downarrow}), \tag{3.B.7}$$

and impose a hard-wall boundary condition at $y = 0$. Dropping rapidly oscillating terms, we write

$$\psi(y) = \frac{1}{\sqrt{N}} \sum_{j=1}^{8} c_j e^{i\lambda_j y} \tilde{\phi}_{\lambda_j}, \tag{3.B.8}$$

with N as a normalization constant and $\tilde{\phi}$ an 8 component vector. We find a non-trivial zero energy solution characterized by coefficients ($c_5 = c_6 = c_8 = 0$),

$$c_2/c_1 = -c_7/c_1 = 1, \;\; c_3/c_1 = c_4/c_1 = g_+. \tag{3.B.9}$$

Bibliography

[1] C. L. Kane and E. J. Mele, Phys. Rev. Lett. **95**, 226801 (2005).

[2] C. L. Kane and E. J. Mele, Phys. Rev. Lett. **95**, 146802 (2005).

[3] C. Wu, B. A. Bernevig, and S. Zhang, Phys. Rev. Lett. **96**, 106401 (2006).

[4] B. A. Bernevig, T. L. Hughes, and S. Zhang, Science **314**, 5806 (2006).

[5] M. König, S. Wiedmann, C. Brüne, A. Roth, H. Buhmann, L. W. Molenkamp, X. Qi, and S. Zhang, Science **318**, 5851 (2007).

[6] L. Fu, C. L. Kane, and E. J. Mele, Phys. Rev. Lett. **98**, 106803 (2007).

[7] J. E. Moore and L. Balents, Phys. Rev. B **75**, 121306(R) (2007).

[8] D. Hsieh, D. Qian, L. Wray, Y. Xia, Y. S. Hor, R. J. Cava, and M. Z. Hasan, Nature **452**, 970 (2008).

[9] D. Hsieh, Y. Xia, L. Wray, D. Qian, A. Pal, J. H. Dil, J. Osterwalder, F. Meier, G. Bihlmayer, C. L. Kane, Y. S. Hor, R. J. Cava, and M. Z. Hasan, Science **323**, 919 (2009).

[10] M. Levin and A. Stern, Phys. Rev. Lett. **103**, 196803 (2009).

[11] J. Maciejko, X. Qi, A. Karch, and S. Zhang, Phys. Rev. B **86**, 235128 (2011).

[12] J. Klinovaja and Y. Tserkovnyak, Phys. Rev. B **90**, 115426 (2014).

[13] M.H. Freedman, M. J. Larsen, and Z. Wang, Commun. Math. Phys. **227**, 605 (2002).

[14] M. Cheng, Phys. Rev. B **86**, 195126 (2012).

[15] N. H. Lindner, E. Berg, G. Refael, and A. Stern, Phys. Rev. X **2**, 041002 (2012).

[16] A. Vaezi, Phys. Rev. B 87, 035132 (2013).

[17] D. Clarke, J. Alicea, and K. Shtengel, Nat. Commun. 4, 1348 (2013).

[18] J. Klinovaja and D. Loss, Phys. Rev. Lett. **112**, 246403 (2014).

[19] J. Klinovaja and D. Loss, Phys. Rev. B **90**, 045118 (2014).

[20] C. L. Kane, R. Mukhopadhyay, and T. C. Lubensky, Phys. Rev. Lett. **88**, 036401 (2002).

[21] D. Poilblanc, G. Montambaux, M. Héritier, and P. Lederer, Phys. Rev. Lett. **58**, 270 (1987).

[22] L. P. Gor'kov and A. G. Lebed, Phys. Rev. B **51**, 3285 (1995).

[23] J. Klinovaja and D. Loss, Phys. Rev. Lett. **111**, 196401 (2013).

[24] J. C. Y. Teo and C. L. Kane, Phys. Rev. B **89**, 085101 (2014).

[25] J. Klinovaja and D. Loss, Eur. Phys. J. B **87**, 171 (2014).

[26] T. Meng, P. Stano, J. Klinovaja, and D. Loss, Eur. Phys. J. B **87**, 203 (2014).

[27] T. Neupert, C. Chamon, C. Mudry, and R. Thomale, Phys. Rev. B **90**, 205101 (2014).

[28] E. Sagi and Y. Oreg, Phys. Rev. B **90**, 201102 (2014).

[29] J. Klinovaja, Y. Tserkovnyak, and D. Loss, Phys. Rev. B **91**, 085426 (2015).

[30] J. Klinovaja, P. Stano, and D. Loss, Phys. Rev. Lett. **116**, 176401 (2016).
[31] S. Sahoo, Z. Zhang, and J. C. Y. Teo, arXiv:1509.07133.
[32] T. Meng, Phys. Rev. B **92**, 115152 (2015).
[33] E. Sagi and Y. Oreg, Phys. Rev. B **92**, 195137 (2015).
[34] L. Trifunovic, D. Loss, and J. Klinovaja, Phys. Rev. B **93**, 205406 (2016).
[35] J. Nitta, T. Akazaki, H. Takayanagi, and T. Enoki, Phys. Rev. Lett. **78**, 1335 (1997).
[36] F. Dettwiler, J. Fu, S. Mack, P. J. Weigele, J. C. Egues, D. D. Awschalom, D. M. Zumbühl, arxiv: 1702.05190 (2017).
[37] K. S. Novoselov, A. Mishchenko, A. Carvalho, and A. H. Castro Neto, Science **353**, 6298 (2016).
[38] B. Sachs, L. Britnell, T. O. Wehling, A. Eckmann, R. Jalil, B. D. Belle, A. I. Lichtenstein, M. I. Katsnelson, and K. S. Novoselov, App. Phys. Lett. **103** 251607 (2013).
[39] K. Novoselov, V. Fal'ko, L. Colombo, P. Gellert, M. Schwab, and K. Kim, Nature **490**, 192 (2012).
[40] R. A. Deutschmann, W. Wegscheider, M. Rother, M. Bichler, G. Abstreiter, C. Albrecht, and J. H. Smet, Phys. Rev. Lett. **86**, 1857 (2001).
[41] D. Tanmoy and A. V. Balatsky, Nat. Commun. **4**, 1972 (2013).
[42] S. I. Erlingsson and J. C. Egues, Phys. Rev. B **91**,035312 (2015).
[43] J. Maciejko, X. Qi, A. Karch, and S. Zhang, Phys. Rev. Lett. **105**, 246809 (2010).
[44] M. D. Johannes and I. I. Mazin, Phys. Rev. B **77**, 165135 (2008).
[45] K. Kuroki, S. Onari, R. Arita, H. Usui, Y. Tanaka, H. Kontani, and H. Aoki Phys. Rev. Lett. **101**, 087004 (2008).
[46] R. Nandkishore, L. S. Levitov and A. V. Chubukov, Nature Physics **8**, 158 (2012).
[47] D. Chowdhury and S. Sachdev, Phys. Rev. B **90**, 245136 (2014).
[48] I. Affleck and A.W.W. Ludwig, Nucl. Phys. B **360**, 641 (1991).
[49] I. Affleck, *Conformal Field Theory Approach to the Kondo Effect*, Lectures notes, Acta Phys. Polon. B **26**, 1869 (1995).
[50] A. Altland and M. R. Zirnbauer, Phys. Rev. B **55**, 1142 (1997).
[51] M. R. Zirnbauer, J. Math. Phys. **37**, 4986 (1996).
[52] S. Ryu, A. P. Schnyder, A. Furusaki, and A. W. W. Ludwig, New J. Phys. **12**, 065010 (2010).
[53] X. Qi, T. L. Hughes, and S. Zhang, Phys. Rev. B **78**, 195424 (2008).
[54] J. Klinovaja and D. Loss, Phys. Rev. B **86**, 085408 (2012).
[55] T. Giamarchi, *Quantum Physics in One Dimension* (Oxford University Press, Oxford, 2004).
[56] Y. Oreg, E. Sela, and A. Stern, Phys. Rev. B **89**, 115402 (2014).
[57] J. Schliemann, J. C. Egues, and D. Loss, Phys. Rev. Lett. **90**, 146801 (2003).
[58] B. A. Bernevig, J. Orenstein, and S. Zhang, Phys. Rev. Lett **97**, 236601 (2006).
[59] L. Meier, G. Salis, I. Shorubalko, E. Gini, S. Schön, and K. Ensslin, Nat. Phys. **3**, 650 (2007).
[60] J. D. Koralek, C. P. Weber, J. Orenstein, B. A. Bernevig, S. Zhang, S. Mack, and D. D. Awschalom, Nature **458**, 610 (2009).
[61] M. P. Walser, C. Reichl, W. Wegscheider, and G. Salis, Nat. Phys. **8**, 757 (2012).
[62] T. Meng, J. Klinovaja, and D. Loss, Phys. Rev. B **89**, 205133 (2014).
[63] F. Dettwiler, J. Fu, S. Mack, P. J. Weigele, J. C. Egues, D. D. Awschalom, and D. M. Zumbühl, Phys. Rev. X **7**, 031010 (2017).
[64] A. J. A. Beukman, F. K. de Vries, J. van Veen, R. Skolasinski, M. Wimmer, F. Qu, D. T. de Vries, B. Nguyen, W. Yi, A. A. Kiselev, M. Sokolich, M. J. Manfra, F. Nichele, C. M. Marcus, and L. P. Kouwenhoven, arXiv:1704.03482 (2017).

[65] S. M. Young, S. Zaheer, J. C. Y. Teo, C. L. Kane, E. J. Mele, and A. M. Rappe, Phys. Rev. Lett. **108**, 140405 (2012).

[66] A. A. Burkov and L. Balents, Phys. Rev. Lett. **107**, 127205 (2011).

[67] Y. L. Chen *et al.*, Science **329**, 659 (2010).

[68] M. V. Hosseini and M. Askari, Phys. Rev. B **92**, 224435 (2015).

[69] H. Chang, J. Zhou, S. Wang, W. Shan, and D. Xiao, Phys. Rev. B **92**, 241103(R) (2015).

[70] D. Rainis, L. Trifunovic, J. Klinovaja, and D. Loss, Phys. Rev. B **87**, 024515 (2013).

Chapter 4

Rashba Sandwiches with Topological Superconducting Phases

Adapted from:
Yanick Volpez, Daniel Loss, and Jelena Klinovaja
"Rashba sandwiches with topological superconducting phases",
Phys. Rev. B **97**, 195421 (2018).

We introduce a versatile heterostructure harboring various topological superconducting phases characterized by the presence of helical, chiral, or unidirectional edge states. Changing parameters, such as an effective Zeeman field or chemical potential, one can tune between these three topological phases in the same setup. Our model relies only on conventional nontopological ingredients. The bilayer setup consists of an s-wave superconductor sandwiched between two two-dimensional electron gas layers with strong Rashba spin-orbit interaction. The interplay between two different pairing mechanisms, proximity induced direct and crossed Andreev superconducting pairings, gives rise to multiple topological phases. In particular, helical edge states occur if crossed Andreev superconducting pairing is dominant. In addition, an in-plane Zeeman field leads to a two-dimensional gapless topological phase with unidirectional edge states, which were previously predicted to exist only in non-centrosymmetric superconductors. If the Zeeman field is tilted out of the plane, the system is in a topological phase hosting chiral edge states.

4.1 Introduction

The discovery that certain properties of quantum states of matter can be captured in terms of topological invariants [1–3] immune to microscopic details of a system has triggered enormous interest in the exploration of topological phases of matter [4–7]. Currently, a great effort is put into the search for localized Majorana quasiparticles that are predicted to appear in one-dimensional topological superconductors (TSCs) [8–22]. Two-dimensional (2D) TSCs are the particle-hole symmetric analogs of the experimentally more extensively studied topological insulators (TI) [23–47]. One-dimensional (1D) TSCs have been the subject of intense experimental research [48–65], while 2D TSCs are not yet so well developed experimentally. However, various setups hosting chiral [66–74] and helical [75–84] superconducting edge states were proposed theoretically. In addition to gapped TSCs, there exist gapless TSCs, which are predicted to be realized in nodal superconductors with mixed singlet-triplet pairing and Rashba spin-orbit interaction (SOI) or in various heterostructures [85–95]. The majority of these proposals involve topological insulators and/ or unconventional superconductors with p-, d-wave pairing symmetry.

In this work, we propose a bilayer heterostructure which can be brought into all the 2D topological phases mentioned above without the need of including topological materials and/or unconventional superconductors (SCs). The setup is composed of only conventional components: an s-wave superconductor sandwiched between two two-dimensional electron gas (2DEG) layers with strong Rashba spin-orbit interaction (SOI) [see Fig. 4.1]. The proximity to the superconductor induces superconducting correlations in the 2DEG layers with direct and crossed Andreev pairings [96–107]. In the former case, a Cooper pair tunnels into one layer, whereas, in the latter case, a Cooper pair splits and the electrons tunnel to opposite layers respectively. When crossed Andreev pairing is dominant, the system is in a gapped phase with a Kramers pair of helical edge states, *i.e.*, it is a helical TSC.

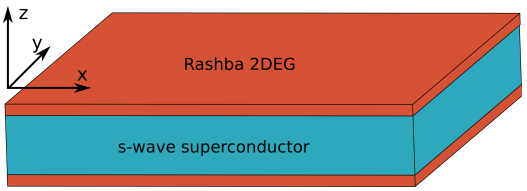

Figure 4.1: Sketch of the bilayer setup consisting of an s-wave superconductor (blue) sandwiched between two two-dimensional electron gas layers (red) with strong Rashba spin-orbit interaction.

Interestingly, if an effective Zeeman field is introduced, *e.g.*, due to externally applied magnetic fields or due to the ordering of magnetic impurities, the bilayer setup has the potential to realize either a chiral or a gapless TSC. If the Zeeman field lies in the plane, then, above a certain critical field strength, the system enters a gapless topological phase with unidirectional edge states. Unidirectional edge states, which are states that propagate in the same direction on opposite edges, appear on the edge orthogonal to the direction of the in-plane field [93]. If the Zeeman field points out of the plane with an angle larger than a model parameter dependent threshold, the system enters again a fully gapped phase with chiral edge states. In contrast to the unidirectional states, the chiral edge states propagate in opposite directions on opposite edges and appear on all boundaries of the system.

To the best of our knowledge, none of the theoretical proposals for realizing 2D TSCs by solely including conventional non-topological ingredients was reported to be able to obtain all of the topological phases mentioned above.

The paper is organized as follows. In Section 4.2, we introduce the effective model describing our setup and discuss its bulk properties in the absence of a Zeeman field. In Section 4.3, we show in which parameter regimes the system is a helical TSC, characterize the spin and charge properties of the helical edge states, and derive the effective low-energy Hamiltonian for the edge states. In Section 4.4, we study the possible topological phases in the presence of a Zeeman field. We show that the helical TSC, protected by time-reversal symmetry, gets immediately destroyed, and the topological phases with chiral and gapless edge states become accessible.

4.2 Model

We consider a bilayer setup consisting of two 2DEG layers with strong Rashba SOI coupled to an s-wave superconductor [see Fig. 4.1]. Each layer is characterized by the SOI strength α_τ, where we label the upper (lower) layer by the index $\tau = 1$ ($\tau = \bar{1}$). In the following, we restrict the discussion to the case $\alpha_1 > \alpha_{\bar{1}} > 0$. The z axis is normal to the layers and $\boldsymbol{k} = (k_x, k_y)$ is the in-plane momentum. The Hamiltonian describing the two uncoupled layers reads in momentum space as

$$H_\tau = \sum_{\sigma,\sigma'} \int d^2\boldsymbol{k}\ \psi^\dagger_{\tau\sigma,\mathbf{k}} h_{\tau\sigma\sigma'}(\boldsymbol{k}) \psi_{\tau\sigma',\mathbf{k}}, \tag{4.2.1}$$

where $h_{\tau\sigma\sigma'}(\boldsymbol{k}) = [\epsilon_k - \mu_\tau + \alpha_\tau \boldsymbol{g}\cdot\boldsymbol{\sigma}]_{\sigma\sigma'}$ with $\epsilon_k = \hbar^2|\boldsymbol{k}|^2/2m$ and $\boldsymbol{g} = (k_y, -k_x, 0)$. The field operator $\psi_{\tau\sigma,\mathbf{k}}$ annihilates an electron in the layer $\tau = \{1, \bar{1}\}$ with spin projection $\sigma = \{1, \bar{1}\}$ and momentum $\boldsymbol{k}$. For simplicity, in what follows, we assume that

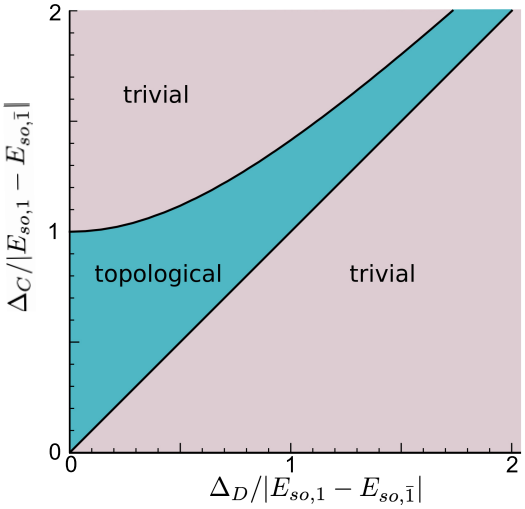

Figure 4.2: Topological phase diagram as a function of direct (Δ_D) and crossed (Δ_C) Andreev superconducting pairing amplitude. Topological phase transitions occur for $\Delta_D = \Delta_C$ and $\Delta_C^2 = \Delta_D^2 + (E_{so,1} - E_{so,\bar{1}})^2$ (black lines). The topological phase (blue area) hosts a Kramers pair of edge states, whereas in the trivial phase there are no edge states. The larger the difference of the spin-orbit energies of the two layers, the larger is the topological region.

the chemical potentials μ_τ are tuned to the spin-orbit energy of the respective layer $E_{so,\tau} = m\alpha_\tau^2/2\hbar^2$. This assumption allows us to solve the problem analytically. A detuning of the chemical potential $\delta\mu_\tau$ (away from $E_{so,\tau}$) leads to a suppression of the crossed Andreev pairing. However, as we have checked numerically, all results remain valid as long as $\delta\mu_\tau$ is the smallest energy scale, $\delta\mu_\tau < \min(\Delta_D, \Delta_C, \Delta_Z)$, where Δ_Z is the Zeeman energy to be introduced later.

The proximity-induced superconductivity opens gaps in the spectrum of the bilayer system and is responsible for the topological phase. Generally, there are two types of superconducting terms: direct and crossed Andreev pairing terms of strength Δ_D and Δ_C, respectively. The direct (crossed Andreev) proximity-induced superconductivity induces coupling between two electrons from the same layer (from two different layers),

$$H_D = \frac{\Delta_D}{2} \sum_{\substack{\tau \\ \sigma,\sigma'}} \int d^2\boldsymbol{k} \left(\psi^\dagger_{\tau\sigma,\boldsymbol{k}} [i\sigma_2]_{\sigma\sigma'} \psi^\dagger_{\tau\sigma',-\boldsymbol{k}} + \text{H.c.} \right), \tag{4.2.2}$$

$$H_C = \frac{\Delta_C}{2} \sum_{\substack{\tau \\ \sigma,\sigma'}} \int d^2\boldsymbol{k} \left(\psi^\dagger_{\tau\sigma,\boldsymbol{k}} [i\sigma_2]_{\sigma\sigma'} \psi^\dagger_{\bar{\tau}\sigma',-\boldsymbol{k}} + \text{H.c.} \right). \tag{4.2.3}$$

Without loss of generality we assume Δ_C, $\Delta_D > 0$ throughout this work.

The total Hamiltonian is given by $H = H_1 + H_{\bar{1}} + H_D + H_C$ and can be rewritten

in terms of Pauli matrices $H = \frac{1}{2}\int d^2\boldsymbol{k}\ \Psi^\dagger_{\boldsymbol{k}} h(\boldsymbol{k})\Psi_{\boldsymbol{k}}$ with

$$\begin{aligned} h(\boldsymbol{k}) = &\epsilon_k\eta_3 + (\alpha_+ + \alpha_-\tau_3)(\sigma_1 k_y - \eta_3\sigma_2 k_x) \\ &- \Delta_D\eta_2\sigma_2 - \Delta_C\tau_1\eta_2\sigma_2, \end{aligned} \tag{4.2.4}$$

where we have introduced $\alpha_\pm = (\alpha_1 \pm \alpha_{\bar{1}})/2$ and the Pauli matrices τ_i, η_i, and σ_i acting in layer, particle-hole, and spin space, respectively. One can check that H is time-reversal invariant with the time-reversal operator given by $\Theta = -i\sigma_2\mathcal{K}$, where $\mathcal{K}$ is the complex conjugation operator. The particle-hole symmetry operator is given by $\mathcal{P} = \eta_1$. Therefore, H belongs to the DIII symmetry class which has a $\mathbb{Z}_2$ classification for 2D systems [108]. The bulk spectrum of the bilayer setup is given by

$$\begin{aligned} E^2_{\pm,\pm}(k) = &\tilde{\epsilon}^2_{\pm,k} + \alpha_-^2 k^2 + \Delta_D^2 + \Delta_C^2 \\ &\pm 2\sqrt{\alpha_-^2 k^2(\tilde{\epsilon}^2_{\pm,k} + \Delta_C^2) + \Delta_C^2\Delta_D^2}, \end{aligned} \tag{4.2.5}$$

where $\tilde{\epsilon}_{\pm,k} = \epsilon_k \pm \alpha_+ k$. The bulk spectrum is gapped except in two special cases. First, if $\Delta_C = \Delta_D$, the bulk gap closes at $k = 0$. Second, if $\Delta_C = \tilde{\Delta}_C$, where $\tilde{\Delta}_C^2 = \Delta_D^2 + (E_{so,1} - E_{so,\bar{1}})^2$, the bulk gap closes at $k = 2m\alpha_+/\hbar^2$. Here the bulk gap is not closed at one point in momentum space, as in the first case, but along a circular nodal line. Both bulk gap closings correspond to a topological phase transition. The topological phase diagram is presented in Fig. 4.2, and contains one topological and two trivial regions. It is obvious to see that the system is in a trivial phase when $\Delta_C = 0$ and $\Delta_D > 0$. The system is therefore in the trivial phase for the parameter regime $\Delta_C < \Delta_D$. In the regime $\Delta_D < \Delta_C < \tilde{\Delta}_C$, the system is in the topological phase, where, as we will show below, a Kramers pair of edge states exists at each edge. For large Δ_C, *i.e.*, $\Delta_C > \tilde{\Delta}_C$, the edge states disappear, which is again a trivial phase.

4.3 Helical Topological Superconductor

4.3.1 Helical Edge States

In order to confirm the phase diagram obtained from the bulk spectrum in the previous section, we now investigate a finite-size system and focus on the properties of the edges. We first solve the problem numerically by implementing a tight-binding model for the bilayer setup [109]. Without loss of generality, the layers are taken to be finite along the y direction, of length L (N_y lattice sites separated by lattice constant a), and translationally invariant along the x direction, allowing

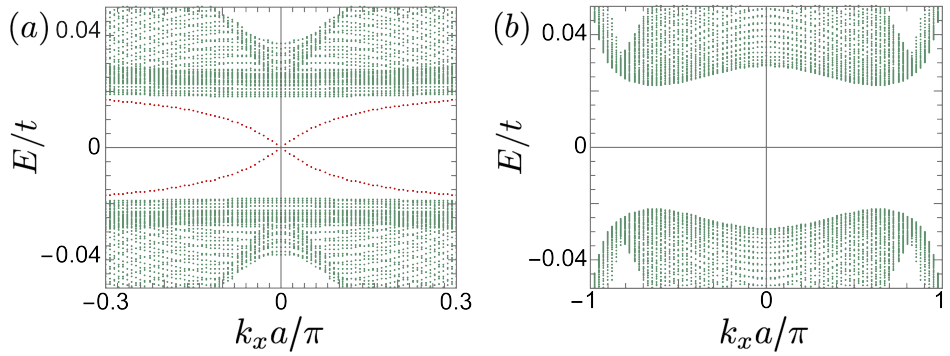

Figure 4.3: Energy spectrum of the bilayer setup in (a) the topological phase ($\Delta_C/t = 0.11$) and (b) the trivial phase ($\Delta_C/t = 0.22$). In both cases the bulk states (green) have a spectral gap, while a Kramers pair of edge states (red) is only present in (a). The edge states are localized at both edges and have a linear dispersion around $k_x = 0$. The numerical parameters are chosen as $N_y = 300$, $\mu/t = -4$, $\alpha_1/t = 0.55$, $\alpha_{\bar{1}}/t = 0.35$, and $\Delta_D/t = 0.06$.

us to use k_x as a good quantum number. The Hamiltonian for this setup is given by $H = H_1 + H_{\bar{1}} + H_D + H_C$ with

$$
\begin{aligned}
H_\tau = \frac{1}{2}\sum_{k_x,n}\Big\{\sum_\sigma\Big(& -tc^\dagger_{k_x\tau(n+1)\sigma}c_{k_x\tau n\sigma} + tc_{-k_x\tau n\sigma}c^\dagger_{-k_x\tau(n+1)\sigma} \\
& + [-t\cos(k_x a_x) + \mu_\tau/2]c^\dagger_{k_x\tau n\sigma}c_{k_x\tau n\sigma} - [-t\cos(k_x a_x) + \mu_\tau/2]c_{-k_x\tau n\sigma}c^\dagger_{-k_x\tau n\sigma} + \text{H.c.}\Big) \\
& + \tilde{\alpha}_\tau\Big[i(c^\dagger_{k_x\tau(n+1)\uparrow}c_{k_x\tau n\downarrow} - c^\dagger_{k_x\tau(n-1)\uparrow}c_{k_x\tau n\downarrow}) + 2i\sin(k_x a_x)c^\dagger_{k_x\tau n\uparrow}c_{k_x\tau n\downarrow} \\
& i(c_{-k_x\tau n\downarrow}c^\dagger_{-k_x\tau(n+1)\uparrow} - c_{-k_x\tau n\downarrow}c^\dagger_{-k_x\tau(n-1)\uparrow}) - 2i\sin(k_x a_x)c_{-k_x\tau n\downarrow}c^\dagger_{-k_x\tau n\uparrow} + \text{H.c.}\Big]\Big\}, \\
H_C = \frac{\Delta_C}{2}\sum_{k_x}\sum_{n,\tau}\Big(c^\dagger_{k_x\tau n\sigma}[i\sigma_2]_{\sigma\sigma'}c^\dagger_{-k_x\bar{\tau}n\sigma'} + \text{H.c.}\Big), \\
H_D = \frac{\Delta_D}{2}\sum_{k_x}\sum_{n,\tau}\Big(c^\dagger_{k_x\tau n\sigma}[i\sigma_2]_{\sigma\sigma'}c^\dagger_{-k_x\tau n\sigma'} + \text{H.c.}\Big).
\end{aligned}
\tag{4.3.1}
$$

Here, t denotes the hopping amplitude. The operator $c_{k_x\tau n\sigma}$ acts on an electron at position $y = na$ in the layer $\tau(= -\bar{\tau})$ with momentum k_x and spin projection σ. The spin-flip hopping amplitude is related to the SOI parameter by $\tilde{\alpha} = \alpha/2a_y$ [110]. Solving the Hamiltonian H, one finds that there are no edge states in the regimes $\Delta_C < \Delta_D$ and $\Delta_C > \tilde{\Delta}_C$ [see Fig. 4.3(b)], which confirms that these parameter regimes correspond to the trivial phases (see Fig. 4.2). In the regime $\Delta_D < \Delta_C < \tilde{\Delta}_C$ both edges host a Kramers pair of subgap states. These states are localized on the edges and have a linear dispersion around $k_x = 0$ [see Fig. 4.3(a)]. This is the hallmark of a helical TSC and confirms our expectation that this parameter

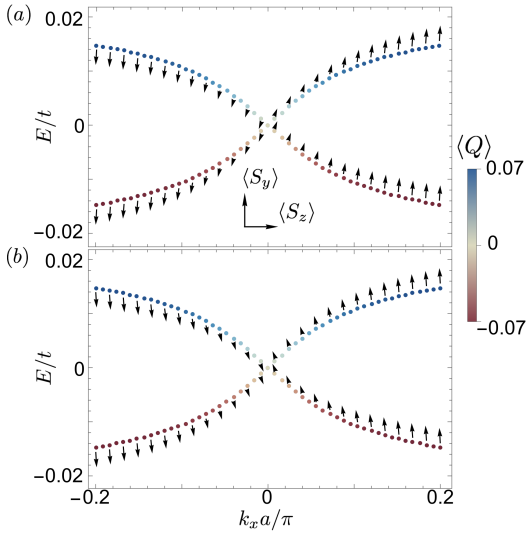

Figure 4.4: Energy spectrum of helical edge states (a) on the left edge ($y = 0$) and (b) on the right edge ($y = L$). The average of the charge operator is encoded in the coloring of the data points and given in units of e. One can see that for a given energy $\langle Q(k_x)\rangle = \langle Q(-k_x)\rangle$ as is expected, since time-reversal does not invert the sign of the charge. The average spin as a function of k_x is encoded in the black arrows. The average spin component along the x axis is zero for all momenta, while the other components are non-zero, and for the Kramers partner the relation $\langle S_i(k_x)\rangle_1 = -\langle S_i(-k_x)\rangle_2$ holds. The wavefunctions on opposite edges are related by the reflection symmetry operator $\mathcal{I} = \sigma_y$. Thus, states on opposite edges, which propagate in the same direction, have the same average spin along the y axis whereas their average spins along the z axis are opposite. The numerical parameters are the same as in Fig. 4.3.

regime corresponds to the topological phase.

Further, we investigate the spin and charge properties of the edge states. Since in our setup spin and charge are not conserved quantities, we calculate the expectation value of the spin (charge) operator $\boldsymbol{S}$ (Q). In the following, $\langle O\rangle_\beta = \langle\Phi_\beta|O|\Phi_\beta\rangle$ denotes the expectation value for some operator O, where the ket $|\Phi_\beta\rangle$ describes the two edge states labeled by $\beta \in \{1, 2\}$ (for further details we refer to Appendix 4.A). At $k_x = 0$, where the system can be mapped to the 1D analog of our setup [111, 112], the edge states have zero average spin and charge. This is consistent with previous works. For all other values of k_x the expectation values are generally non-zero and, as is expected, for fixed energy the two Kramers partners have the same charge. The average of the x component of the spin vanishes, $\langle S_x\rangle = 0$, for all values of k_x, while the remaining components satisfy $\langle S_i(k_x)\rangle_1 = -\langle S_i(-k_x)\rangle_2$ [see Fig. 4.4]. In this sense, the edge states are helical and protected from back-scattering by time-reversal symmetry. Note that the edge states on the left and the right edge

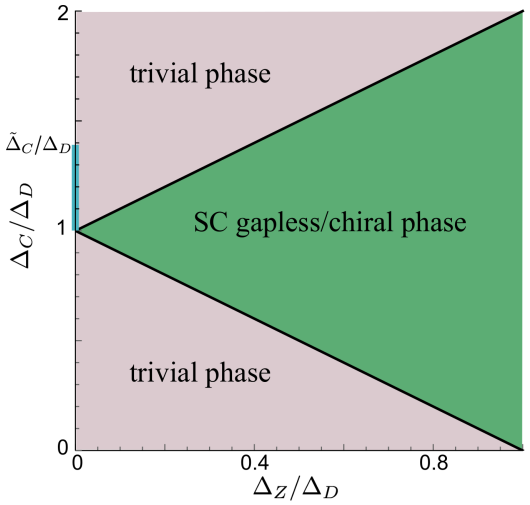

Figure 4.5: Topological phase diagram as a function of the Zeeman energy (Δ_Z) and the crossed Andreev superconducting pairing amplitude (Δ_C). Topological phase transitions occur for $\Delta_C = |\Delta_D \pm \Delta_Z|$ (black lines) and for $\Delta_C = \tilde{\Delta}_C$ and $\Delta_Z = 0$. In the absence of a Zeeman field there exists a helical topological phase for $\Delta_D < \Delta_C < \tilde{\Delta}_C$, which is indicated by the blue line. We note that $\tilde{\Delta}_C$ depends on both Δ_D and the difference in SOI energies, and in this plot we assume $\Delta_D = |E_{so,1} - E_{so,\bar{1}}|$ such that $\tilde{\Delta}_C/\Delta_D = \sqrt{2}$. In the green region the system is in a 2D superconducting gapless (chiral) phase for an in-plane (out-of-plane) Zeeman field. For details on the transition from the gapless to the chiral phase as a function of the out-of-plane angle we refer to the main text.

are connected by reflection symmetry, where the symmetry operator is given by $\mathcal{I} = \sigma_y$. Thus, the wavefunctions of the edge states on opposite edges and their properties are related by $\mathcal{I}$. Therefore, states on opposite edges that propagate in the same direction have the same average spin projection on the y axis. In contrast, their average spin projections on the z axis are opposite (differ by a minus sign) [see Fig. 4.4].

4.3.2 Effective Low-Energy Hamiltonian

As shown in the previous section, the topological phase hosts a Kramers pair of helical edge states with a linear dispersion around $k_x = 0$ on both edges. Next, we derive the effective low-energy Hamiltonian describing the properties of these states localized at the left ($y = 0$) edge. As in the tight-binding model, we assume that the system is translationally invariant along the x direction and we solve an effectively 1D Hamiltonian parametrized by k_x. For the moment, we assume that the right edge ($y = L$) is infinitely far away. This assumption allows us to treat

the edge states as if the width of the sample was much larger than the localization length ξ of the edge states. Due to particle-hole symmetry, the edge states are at zero energy at $k_x = 0$ [see Fig. 4.3(a)], and we first determine the wavefunctions at this special point. In a next step, we treat the k_x-terms perturbatively for $k_x\xi \ll 1$, and keep only terms linear in k_x. Using $h(0, k_y)$ [see Eq. (4.2.4)] we obtain two wavefunctions Φ_β ($\beta \in \{1, 2\}$) in the strong SOI regime for $\alpha_1 \gg \alpha_{\bar{1}}$ (see Appendix 4.B). These two wavefunctions correspond to a Kramers pair of edge states and exist only if $\Delta_D < \Delta_C < \tilde{\Delta}_C$, which is consistent with our previous results. The wavefunctions have support in momentum space around $k_{F\tau} = 2k_{so\tau}$ and $k_{F,i} = 0$. The corresponding localization length ξ is determined by the bulk gaps at these Fermi points [113] and, thus, is given by the maximum of four length scales: $\xi_\tau = \hbar v_{F,\tau}/\Delta_D$ and

$$\xi_\pm = \frac{2\hbar v_{F,1} v_{F,\bar{1}}}{\sqrt{\Delta_D^2 (v_{F,1} - v_{F,\bar{1}})^2 + 4\Delta_C^2 v_{F,1} v_{F,\bar{1}}} \pm \Delta_D (v_{F,1} + v_{F,\bar{1}})}, \tag{4.3.2}$$

respectively, where we have introduced the Fermi velocities $v_{F\tau} = \alpha_\tau/\hbar$.

For $k_x\xi \ll 1$, the perturbation term linear in k_x is given by $h_{k_x} = (\alpha_+ + \alpha_-\tau_3)\eta_3\sigma_2 k_x$ [see Eq. (4.2.4)], and the first order correction to the energy can be found by calculating the matrix elements $\langle\Phi_\beta|h_{k_x}|\Phi_{\beta'}\rangle$. As a result the effective low-energy Hamiltonian is given by

$$h_{eff} = \hbar\tilde{v}\beta_3 k_x. \tag{4.3.3}$$

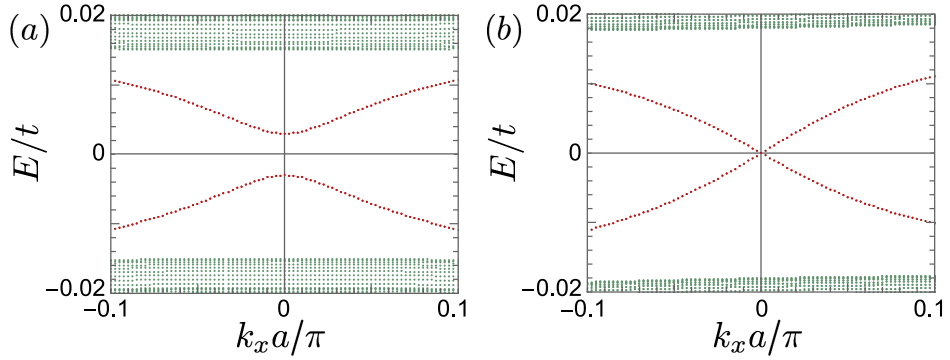

Figure 4.6: Energy spectrum in the presence of an in-plane Zeeman field aligned (a) in the x direction ($\phi = 0$) and (b) in the y direction ($\phi = \pi/2$). Green (red) dots represent bulk (edge) states. The edge states become gapped once the Zeeman field has a component along the respective edge. The size of the gap opened in the edge state spectrum is given by the projection of the Zeeman field on the propagation direction, $\Delta E = \Delta_Z \cos\phi$. The numerical parameters are chosen as $N_x = 800$, $\alpha_1/t = 0.35$, $\alpha_{\bar{1}}/t = 0.15$, $\mu = -4t$, $\Delta_D/t = 0.06$, $\Delta_C/t = 0.12$, and $\Delta_Z/t = 0.006$

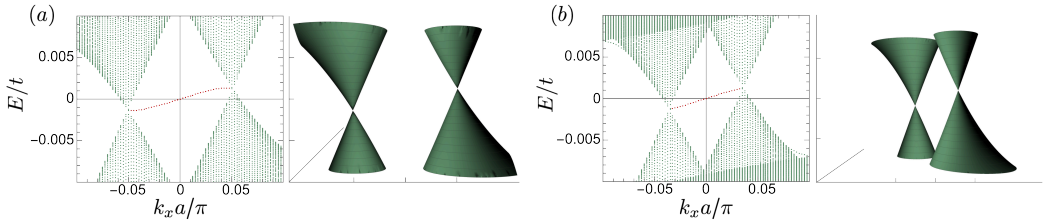

Figure 4.7: Energy spectra in the presence of an inplane Zeeman field (a) $\phi = \pi/2$ and (b) $\phi = \pi/4$. In the left subfigures the bulk (edge) states are represented by green (red) dots and obtained from the tight-binding model. In the right subfigure, we show the bulk spectrum of the translationally invariant system. The line connecting centers of two Weyl cones is orthogonal to the direction of the Zeeman field. The degenerate edge states (one per edge) connect the two Weyl cones. The numerical parameters are chosen as $N_y = 2000$, $\alpha_1/t = 0.35$, $\alpha_{\bar{1}}/t = 0.15$, $\mu = -4t$, $\Delta_D/t = 0.05$, $\Delta_C = \Delta_D$, and $\Delta_Z/t = 0.025$.

Here β_3 is the third Pauli matrix acting in the low-energy subspace spanned by Φ_β and $\tilde{v}$ the effective Fermi velocity. The effective Hamiltonian h_{eff} has a form typical for helical TSCs. The helical edge states have a linear dispersion inside the bulk gap.

4.4 Effect of a Zeeman field. 2D Gapless vs. Chiral Superconducting Topological Phase

Having discussed the helical topological superconducting phase in the previous section, we now investigate the possible topological phases in the presence of an effective Zeeman field, which could arise due to presence of polarized magnetic impurities in both layers, similarly, as was already discussed in the literature for magnetic islands on superconductors, Weyl semimetals or quantum anomalous Hall effect [73, 74, 114–120]. We consider an effective Zeeman field in the direction determined by the unit vector $\boldsymbol{n} = (\cos\phi\cos\theta, \sin\phi\cos\theta, \sin\theta)^T$, then the Zeeman term reads

$$H_Z = \Delta_Z \sum_{\tau} \sum_{\sigma,\sigma'} \int d^2\boldsymbol{k}\ \psi^\dagger_{\tau\sigma,\boldsymbol{k}} [\boldsymbol{n}\cdot\boldsymbol{\sigma}]_{\sigma\sigma'} \psi_{\tau\sigma',\boldsymbol{k}}, \tag{4.4.1}$$

where Δ_Z denotes the Zeeman energy.

Again, we first focus on the phase diagram in the presence of an in-plane Zeeman field ($\theta = 0$), which breaks time-reversal symmetry, see Fig. 4.5. If $\Delta_Z > \Delta_D$, superconductivity is strongly suppressed and the system is gapless. If $\Delta_C = |\Delta_Z \pm \Delta_D|$, the Zeeman term leads to a closing of the bulk gap at $\boldsymbol{k} = 0$ (black lines in Fig. 4.5). If $\Delta_C < \Delta_D$ and $\Delta_Z = 0$ the system is in a trivial phase as was shown above, and therefore, in the whole region $\Delta_C < |\Delta_Z - \Delta_D|$ of the phase

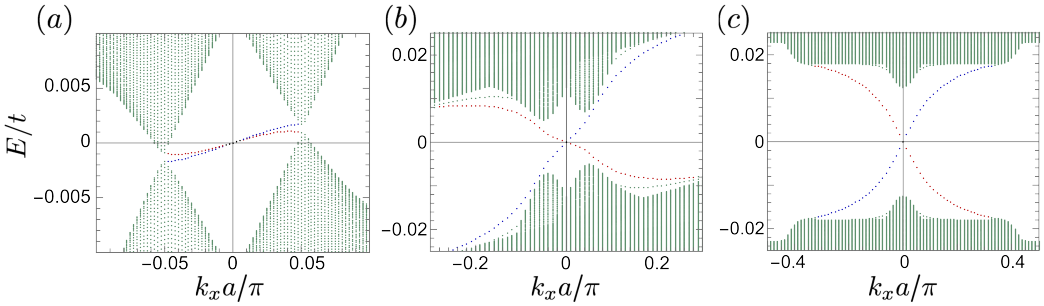

Figure 4.8: Energy spectra in the presence of an out-of-plane Zeeman field for $\phi = \pi/2$ and (a) $\theta = \pi/90$, (b) $\theta = \pi/6$, and (c) $\theta = \pi/2$. The Zeeman field component along the z direction leads to an opening of a gap in the bulk spectrum (green dots) at the position of the nodes. The gap increases with the out-of-plane angle θ. At the same time the degeneracy of the edge states (see Fig. 4.7) gets lifted as the out-of-plane angle increases, and the edge states become chiral, *i.e.*, counterpropagating on opposite edges (red and blue dots) for $\theta > \pi/15$. The other numerical parameters are the same as in Fig. 4.7.

diagram, the system is in the trivial phase. In the regime $\Delta_D < \Delta_C < \tilde{\Delta}_C$ and $\Delta_Z = 0$ the system is in the helical TSC phase with a Kramers pair of gapless edge states (blue line in Fig. 4.5). When $\Delta_Z > 0$, time-reversal symmetry is broken and, thus, the helical edge states are no longer protected against backscattering. If the Zeeman field has a component along a given edge, it leads to a coupling between the Kramers partners and thereby gaps out the edge states. The size of the gap is given by the projection of the Zeeman field on the given edge, which for our tight-binding model translates into $\Delta E = \Delta_Z \cos\phi$ [see Fig. 4.6]. In the special case of $\phi = \pi/2$, the pair of edge states propagating along the x axis stay gapless. However, if the system was finite in both x and y directions, one can make use of the spatial symmetries of the setup to conclude that the spectrum of the edge states propagating along the y direction is gapped. Thus, we conclude that a weak in-plane Zeeman field leads to a gap in the spectrum of the helical edge states at least along one of the edges, so the region $\Delta_C > |\Delta_Z + \Delta_D|$ corresponds to a trivial phase.

Next, we analyze the parameter region of the phase diagram that is bounded by the two gap closing lines $\Delta_C = |\Delta_Z \pm \Delta_D|$ (green area in Fig. 4.5). In this regime, the bulk spectrum contains two Weyl cones. Their position in the Brillouin zone is determined by the polar angle ϕ of the Zeeman field: the line connecting the two Weyl cones is orthogonal to the direction of the effective Zeeman field (see insets in Fig. 4.7). Localized edge states connect the two Weyl nodes in momentum space, where they coexist with bulk modes. Since the nodes are not at zero energy the

edge states have a finite group velocity (see Fig. 4.7). There is one state per edge and they have the same direction of propagation on opposite edges, *i.e.* the system hosts unidirectional edge states [90, 93]. As is the case for Weyl semimetals, in order to determine whether edge states appear on a given edge, one has to project the Weyl nodes onto the edge direction; edge states appear only on edges where the Weyl nodes are not projected onto the same point. For our tight-binding model, this means that the unidirectional edge states do not appear on the edge along the x direction if $\phi = 0$. A gap can be opened in the 2D Weyl spectrum if a perturbation proportional to σ_z is added, *i.e.*, an effective Zeeman field has an out-of-plane component along the z direction. Thus, it is interesting to investigate the evolution of the edge states as the out-of-plane angle θ of the Zeeman field is increased. The larger the angle the larger is the gap, which is opened in the spectrum of Weyl cones. For small θ, the bulk spectrum stays gapless and the edge states remain unidirectional although their two-fold degeneracy gets lifted (see Fig. 4.8). For the parameter settings used in our numerics this holds for $\theta \leq \pi/15$. If θ is larger than this threshold, the bulk spectrum is fully gapped and the edge states evolve from unidirectional to chiral edge states (see Fig. 4.8). We conclude that a 2D gapless topological phase with unidirectional edge states is only achieved if the out-of-plane angle of the Zeeman field is "small" otherwise the system is a fully gapped chiral topological superconductor.

4.5 Conclusions

We have shown how three distinct topological superconducting phases can be engineered in a heterostructure composed of two 2DEG layers with strong Rashba SOI and an s-wave superconductor sandwiched between these two layers. Such a setup could be realized in semiconductor superlattices [121–123] or using (quasi-) 2D materials with strong SOI [124–128].

In the time-reversal symmetric case, a pair of helical edge states exists when crossed Andreev superconducting pairing is dominant. When time-reversal symmetry is broken by a Zeeman field, the system can potentially be in two distinct topological phases. If the field is in-plane or if the out-of-plane component is small enough, a gapless topological superconducting phase with unidirectional edge states can be realized. If the out-of-plane angle is large enough, the system can be tuned into a gapped topological superconducting phase with chiral edge states. It is well-known that the TSCs with a bulk gap are the most stable against disorder. The helical TSC is, due to Kramers theorem, stable against non-magnetic disorder, while a chiral TSC is stable against both non-magnetic and magnetic

disorder. However, in both cases, this only holds as long as the disorder strength is not comparable to the size of the superconducting gap and Weyl cones are well separated, which is the case for long-range disorder [114].

Acknowledgments

We acknowledge support from the Swiss National Science Foundation and NCCR QSIT, and the Marie Sklodowska-Curie Innovative Training Network (ITN-ETN) Spin-NANO. This project has received funding from the European Union's Horizon 2020 research and innovation program (ERC Starting Grant, grant agreement No 757725). We acknowledge helpful discussions with Christopher Reeg and Denis Chevallier.

4.A Numerical Evaluation of Charge and Spin Expection Values

In the main text we discussed the expectation values of the spin (charge) operator for the helical edge states. In this appendix we complete the discussion by providing the detailed expressions. Solving numerically the tight-binding model defined by Eq. (4.3.1), we obtain $8N_y$ energy states for each fixed momentum k_x, *i.e.*, the energy states can be parametrized as $E_n(k_x)$ with the corresponding eigenfunctions $\Phi_n(j,k_x)$, where $n \in \{1,\dots,8N_y\}$ is the band index and $j \in \{1,\dots,N_y\}$ denotes the lattice site. Here, Φ_n is an eight component spinor in Nambu space written in the basis $(c_{k_x 1\uparrow n}, c_{k_x 1\downarrow n}, c^\dagger_{-k_x 1\uparrow n}, c^\dagger_{-k_x 1\downarrow n}, c_{k_x \bar{1}\uparrow n}, c_{k_x \bar{1}\downarrow n}, c^\dagger_{-k_x \bar{1}\uparrow n}, c^\dagger_{-k_x \bar{1}\downarrow n})$.

The average spin and charge of the nth energy eigenstate with k_x fixed is computed as [129]

$$\begin{aligned}\langle \boldsymbol{S}(k_x)\rangle_n &= \sum_j \Phi_n^\dagger(j,k_x)\boldsymbol{S}\Phi_n(j,k_x),\\ \langle Q(k_x)\rangle_n &= \sum_j \Phi_n^\dagger(j,k_x)Q\Phi_n(j,k_x),\end{aligned} \tag{4.A.1}$$

where $\boldsymbol{S}$ (Q) is the spin (charge) operator measured in units of $\hbar/2$ (e) and represented in Nambu space $S_i = \mathrm{diag}(\sigma_i, -\sigma_i^T, \sigma_i, -\sigma_i^T)$ [$Q = \mathrm{diag}(\sigma_0, -\sigma_0, \sigma_0, -\sigma_0)$], where σ_i are the Pauli matrices and σ_0 is the 2×2 identity matrix.

4.B Derivation of the Effective Low-Energy Hamiltonian

In this appendix we present the detailed calculation of the wavefunctions at $k_x = 0$ and derive the effective low-energy Hamiltonian describing helical edge states [see Eq. (4.3.3) in Sec. 4.3].

The wavefunctions at $k_x = 0$ should be related by time-reversal symmetry Θ and also can be chosen to respect the particle-hole symmetry [111]. As a result, they can be represented in the basis $(\psi_{1\uparrow}, \psi_{1\downarrow}, \psi^\dagger_{1\uparrow}, \psi^\dagger_{1\downarrow}, \psi_{\bar{1}\uparrow}, \psi_{\bar{1}\downarrow}, \psi^\dagger_{\bar{1}\uparrow}, \psi^\dagger_{\bar{1}\downarrow})$ in the following form [113]:

$$\Phi_1(y) = \begin{pmatrix} f_1(y) \\ g_1(y) \\ f_1^*(y) \\ g_1^*(y) \\ f_{\bar{1}}(y) \\ g_{\bar{1}}(y) \\ f_{\bar{1}}^*(y) \\ g_{\bar{1}}^*(y) \end{pmatrix}, \quad \Phi_2(y) = \begin{pmatrix} g_1^*(y) \\ -f_1^*(y) \\ g_1(y) \\ -f_1(y) \\ g_{\bar{1}}^*(y) \\ -f_{\bar{1}}^*(y) \\ g_{\bar{1}}(y) \\ -f_{\bar{1}}(y) \end{pmatrix}. \tag{4.B.1}$$

We start with $h(0, k_y)$ [see Eq. (4.2.4)], which after the unitary transformation $U = e^{-(i\pi/4)\sigma_2}$ reads

$$\begin{aligned} h(0,k_y) =& \frac{\hbar^2 k_y^2}{2m}\eta_3 + (\alpha_+ + \alpha_-\tau_3)\sigma_3 k_y - \Delta_D \eta_2 \sigma_2 \\ & - \Delta_C \tau_1 \eta_2 \sigma_2. \end{aligned} \tag{4.B.2}$$

In the next step, we linearize [130] the spectrum around the Fermi points $k_i = 0$, $k_{F\tau} = \pm 2k_{so,\tau}$ such that the field operators $\psi_{\tau\sigma}$ are approximated as

$$\begin{aligned} \psi_{\tau\uparrow} &= L_{\tau\uparrow}(y) + R_{\tau\uparrow}(y) e^{ik_{F\tau}y}, \\ \psi_{\tau\downarrow} &= L_{\tau\downarrow}(y) e^{-ik_{F\tau}y} + R_{\tau\downarrow}(y), \end{aligned} \tag{4.B.3}$$

where $R_{\tau\sigma}(y)$ $[L_{\tau\sigma}(y)]$ are slowly varying right (left) moving fields with spin projection σ along the x-axis (due to the unitary transformation U above) in the τ layer. In the limit of strong SOI energy and $\alpha_1 \gg \alpha_{\bar{1}}$, the crossed Andreev pairing term only couples fields at $k = 0$ [111]. As a result, the linearized Hamiltonian reads

$$\begin{aligned} \bar{h} =& v_{F1}\hat{k}\frac{1+\tau_3}{2}\rho_3 + v_{F\bar{1}}\hat{k}\frac{1-\tau_3}{2}\rho_3 - \Delta_D \eta_2 \sigma_2 \rho_1 \\ & - \Delta_C \tau_1 \eta_2 (\sigma_2\rho_1 - \sigma_1\rho_2)/2, \end{aligned} \tag{4.B.4}$$

with $\hat{k} = -i\hbar\partial_y$ the momentum operator around the Fermi points and ρ_i acting in left/right mover space. We make the Ansatz $\phi_\xi(y) = \phi_\xi e^{-y/\xi}$ with ϕ_ξ being a 16-component vector and search for decaying zero energy solutions satisfying $\bar{h}\phi_\xi = 0$.

We find eight decaying eigenmodes with localization lengths given by

$$\xi_1 = \frac{\hbar v_{F,1}}{\Delta_D},\ \xi_2 = \frac{\hbar v_{F,\bar{1}}}{\Delta_D}, \tag{4.B.5}$$
$$\xi_3 = \frac{2\hbar v_{F,1} v_{F,\bar{1}}}{-\Delta_D(v_{F,1}+v_{F,\bar{1}}) + \sqrt{\Delta_D^2(v_{F,1}-v_{F,\bar{1}})^2 + 4\Delta_C^2 v_{F,1} v_{F,\bar{1}}}},$$
$$\xi_4 = \frac{2\hbar v_{F,1} v_{F,\bar{1}}}{\Delta_D(v_{F,1}+v_{F,\bar{1}}) + \sqrt{\Delta_D^2(v_{F,1}-v_{F,\bar{1}})^2 + 4\Delta_C^2 v_{F,1} v_{F,\bar{1}}}}.$$

By imposing vanishing boundary condition $\Phi_\beta(0) \stackrel{!}{=} 0$ on a linear combination of these eigenmodes, we find that the edge state wavefunctions are determined by

$$f_1(y) = i g_1^*(y) = -i(e^{-y/\xi_4} - e^{-ik_{F1}y} e^{-y/\xi_1}),$$
$$f_{\bar{1}}(y) = i g_{\bar{1}}^*(y) = -\frac{i}{g_-}(e^{-ik_{F\bar{1}}y} e^{-y/\xi_2} - e^{-y/\xi_4}), \tag{4.B.6}$$

with

$$g_- = \frac{\Delta_D(v_{F1} - v_{F\bar{1}}) + \sqrt{\Delta_D^2(v_{F1}-v_{F\bar{1}})^2 + 4\Delta_C^2 v_{F1} v_{F\bar{1}}}}{2\Delta_C v_{F1}}. \tag{4.B.7}$$

In the limit $v_{F1} = v_{F\bar{1}}$ this solution reproduces the wavefucntions of Kramers pair of Majorana fermions found in Ref. [111]. We note that if $\Delta_D > \Delta_C$, eight eigenmodes are linearly independent and their linear combination cannot satisfy vanishing boundary condition. Therefore, edge states do not exist in this regime.

For $k_x\xi \ll 1$, the perturbation linear in k_x reads $h_{k_x} = (\alpha_+ + \alpha_-\tau_3)\eta_3\sigma_2 k_x/2$. The first-order correction to the energy is calculated by evaluating the matrix elements $\langle \Phi_n | h_{k_x} | \Phi_{n'} \rangle$. Using Eqs. (4.B.1) and (4.B.6), we arrive at

$$\begin{aligned}
\langle \Phi_1 | h_{k_x} | \Phi_1 \rangle &= -2k_x \sum_{\tau=\{1,\bar{1}\}} \alpha_\tau \int_0^\infty dy \left([f_\tau^*]^2 + [f_\tau]^2 \right) \\
&= -\langle \Phi_2 | h_{k_x} | \Phi_2 \rangle , \\
\langle \Phi_1 | h_{k_x} | \Phi_2 \rangle &= -2ik_x \sum_{\tau=\{1,\bar{1}\}} \alpha_\tau \int_0^\infty dy \left([f_\tau^*]^2 - [f_\tau]^2 \right) \\
&= \langle \Phi_2 | h_{k_x} | \Phi_1 \rangle ,
\end{aligned} \tag{4.B.8}$$

where for compactness we express the matrix elements in terms of $f_1(f_{\bar{1}})$ only. Decomposing the functions $f_\tau(y) = \mathrm{Re}[f_\tau(y)] + i\mathrm{Im}[f_\tau(y)]$ into real and imaginary parts we rewrite the matrix elements above as

$$\begin{aligned}
\langle \Phi_1 | h_{k_x} | \Phi_1 \rangle &= -4k_x \sum_{\tau=\{1,\bar{1}\}} \alpha_\tau \int_0^\infty dy \left([\mathrm{Re}(f_\tau)]^2 - [\mathrm{Im}(f_\tau)]^2 \right), \\
\langle \Phi_1 | h_{k_x} | \Phi_2 \rangle &= -8k_x \sum_{\tau=\{1,\bar{1}\}} \alpha_\tau \int_0^\infty dy\ \mathrm{Re}(f_\tau)\mathrm{Im}(f_\tau),
\end{aligned} \tag{4.B.9}$$

which now can be seen to be purely real. For completeness we give the expressions for the decomposition of f_τ into real and imaginary parts

$$\begin{aligned}
\mathrm{Re}(f_1) &= \sin(k_{F1}y)e^{-y/\xi_1},\\
\mathrm{Im}(f_1) &= \cos(k_{F1}y)e^{-y/\xi_1} - e^{-y/\xi_4},\\
\mathrm{Re}(f_{\bar{1}}) &= -\frac{\sin(k_{F\bar{1}}y)e^{-y/\xi_2}}{g_-},\\
\mathrm{Re}(f_{\bar{1}}) &= \frac{1}{g_-}\big[e^{-y/\xi_4} - \cos(k_{F\bar{1}}y)e^{-y/\xi_2}\big].
\end{aligned} \tag{4.B.10}$$

Plugging these equations into (4.B.9), we find the following effective Hamiltonian

$$h_{\mathrm{eff}} = \begin{pmatrix} \langle\Phi_1|h_{k_x}|\Phi_1\rangle & \langle\Phi_1|h_{k_x}|\Phi_2\rangle \\ \langle\Phi_2|h_{k_x}|\Phi_1\rangle & \langle\Phi_2|h_{k_x}|\Phi_2\rangle \end{pmatrix} = \begin{pmatrix} A & B \\ B & -A \end{pmatrix} k_x. \tag{4.B.11}$$

where the real constants A and B are found to be given by

$$\begin{aligned}
A = -4\Big[&\frac{2\alpha_1\xi_1}{1+k_{F1}^2\xi_1^2} + 2\alpha_1\xi_4 - \frac{8\alpha_1\xi_1\xi_4(\xi_1+\xi_4)}{(\xi_1+\xi_4)^2 + k_{F1}^2\xi_1^2\xi_4^2} + \frac{2\alpha_{\bar{1}}\xi_2}{g_-^2(1+k_{F\bar{1}}^2\xi_2^2)} + \frac{2\alpha_{\bar{1}}\xi_4}{g_-^2}\\
&- \frac{8\alpha_{\bar{1}}\xi_2\xi_4(\xi_2+\xi_4)}{g_-^2[(\xi_2+\xi_4)^2 + k_{F\bar{1}}^2\xi_2^2\xi_4^2]}\Big],\\
B = 2\alpha_1 k_{F1}&\Big(\frac{4\xi_1^2\xi_4^2}{(\xi_1+\xi_4)^2 + k_{F1}^2\xi_1^2\xi_4^2} - \frac{\xi_1^2}{1+k_{F1}^2\xi_1^2}\Big)\\
+ \frac{2\alpha_{\bar{1}}k_{F_{\bar{1}}}}{g_-^2}&\Big(\frac{4\xi_2^2\xi_4^2}{(\xi_2+\xi_4)^2 + k_{F1}^2\xi_2^2\xi_4^2} - \frac{\xi_2^2}{1+k_{F1}^2\xi_2^2}\Big).
\end{aligned} \tag{4.B.12}$$

We find that this matrix is diagonal in the basis $\Phi^\pm$ with eigenvalues $\pm\hbar\tilde{v}k_x$, where $\tilde{v} = \sqrt{A^2+B^2}/\hbar$ and

$$\Phi^\pm = \frac{B\Phi_1 \pm (\sqrt{A^2+B^2} \mp A)\Phi_2}{\sqrt{B^2 + (\sqrt{A^2+B^2} \mp A)^2}}. \tag{4.B.13}$$

Bibliography

[1] D. J. Thouless, M. Kohmoto, M. P. Nightingale, and M. den Nijs, Phys. Rev. Lett. **49**, 405 (1982).

[2] C. L. Kane and E. J. Mele, Phys. Rev. Lett. **95**, 146802 (2005).

[3] A. Kitaev, AIP Conference Proceedings **1134**, 22 (2009).

[4] M. Z. Hasan and C. L. Kane, Rev. Mod. Phys. **82**, 3045 (2010).

[5] X. L. Qi and S. C. Zhang, Rev. Mod. Phys. **83**, 1057 (2011).

[6] M. Sato and Y. Ando, Rep. Prog. Phys. **80**, 076501 (2017).

[7] A. Stern, Annual Review of Condensed Matter Physics **7**, 349-368 (2016).

[8] A. Y. Kitaev, Phys.-Usp. **44**, 131 (2001).

[9] D. A. Ivanov, Phys. Rev. Lett. **86**, 268 (2001).

[10] R. M. Lutchyn, J. D. Sau, and S. Das Sarma, Phys. Rev. Lett. **105** , 077001 (2010).

[11] Y. Oreg, G. Refael, and F. v. Oppen, Phys. Rev. Lett. **105**, 177002 (2010).

[12] J. Alicea, Phys. Rev. B **81**, 125318 (2010).

[13] A. C. Potter and P. A. Lee, Phys. Rev. B **83**, 094525 (2011).

[14] D. Chevallier, D. Sticlet, P. Simon, and C. Bena, Phys. Rev. B **85**, 235307 (2012).

[15] J. Klinovaja, S. Gangadharaiah, and D. Loss, Phys. Rev. Lett. **108**, 196804 (2012).

[16] D. Sticlet, C. Bena, and P. Simon, Phys. Rev. Lett. **108**, 096802 (2012).

[17] J. Klinovaja, P. Stano, and D. Loss, Phys. Rev. Lett. **109**, 236801 (2012).

[18] B. I. Halperin, Y. Oreg, A. Stern, G. Refael, J. Alicea, and F. von Oppen, Phys. Rev. B **85**, 144501 (2012).

[19] S. Nadj-Perge, I. K. Drozdov, B. A. Bernevig, and A. Yazdani, Phys. Rev. B **88**, 020407 (R) (2013).

[20] J. Klinovaja, P. Stano, A. Yazdani, and D. Loss, Phys. Rev. Lett. **111**, 186805 (2013).

[21] B. Braunecker and P. Simon, Phys. Rev. Lett. **111**, 147202 (2013).

[22] M. Vazifeh and M. Franz, Phys. Rev. Lett. **111**, 206802 (2013).

[23] O. A. Pankratov, Phys. Rev. A **121**, 360 (1987).

[24] B. A. Bernevig and S.C. Zhang, Phys. Rev. Lett. **96**, 106802 (2005).

[25] C. L. Kane and E. J. Mele, Phys. Rev. Lett. **95**, 226801 (2005).

[26] M. König, S. Wiedmann, C. Brüne, A. Roth, H. Buhmann, L. W. Molenkamp, X. L. Qi, and S. C. Zhang, Science **318**, 5851, 776-770 (2007).

[27] A. Roth, C. Brüne, H. Buhmann, L. W. Molenkamp, J. Maciejko, X. L. Qi, and S. C. Zhang, Sciene **325**, 5938, 294-297 (2009).

[28] G. M. Gusev, E. B. Olshanetsky, Z. D. Kvon, O. E. Raichev, N. N. Mikhailov, and S. A. Dvoretsky, Phys. Rev. B **88**, 195305 (2013).

[29] G. M. Gusev, Z. D. Kvon, E. B. Olshanetsky, A. D. Levin, Y. Krupko, J. C. Portal, N. N. Mikhailov, and S. A. Dvoretsky, Phys. Rev. B **89**, 125305 (2014).

[30] E. Y. Ma, M. R. Calvo, J. Wang, B. Lian, M. Mühlbauer, C. Brüne, Y. T. Cui, K. Lai, W. Kundhikanjana, Y. Yang, M. Baenninger. M. König, C. Ames, H. Buhmann, P. Leubner, L. W. Molenkamp, S. C. Zhang, D. Goldhaber-Gordon, M. A. Kelly, and Z. X. Shen, Nat. Comm. **6**, 7252 (2015).

[31] E. B. Olshanetsky, Z. D. Kvon, G. M. Gusev, A. D. Levin, O. E. Raichev, N. N. Mikhailov, and S. A. Dvoretsky, Phys. Rev. Lett. **114**, 126802 (2015).

[32] R. S. Deacon, J. Wiedenmann, E. Bocquillon, F. Domínguez, T. M. Klapwijk, P. Leubner, C. Brüne, E. M. Hankiewicz, S. Tarucha, K. Ishibashi, H. Buhmann, and L. W. Molenkamp, Phys. Rev. X **7**, 021011 (2017).

[33] C. Liu, T. L. Hughes, X. L. Qi, K. Wang, S. C. Zhang, Phys. Rev. Lett. **100**, 236601 (2008).

[34] I. Knez, R. R. Du, and G. Sullivan, Phys. Rev. Lett. **107**, 136603 (2011).

[35] K. Suzuki, Y. Harada, K. Onomitsu, and K. Muraki, Phys. Rev. **87**, 235311 (2013).

[36] C. Charpentier, S. Fält, C. Reichl, F. Nichele, A. N. Pal, P. Pietsch, T. Ihn, K. Ensslin, and W. Wegscheider, Appl. Phys. Lett. **103**, 112102 (2013).

[37] I. Knez, C. T. Rettner, S. H. Yang, S. S. P. Parkin, L. Du, R. R. Du, and G. Sullivan, Phys. Rev. Lett. **112**, 026602 (2014).

[38] K. Suzuki, Y. Harada, K. Onomitsu, and K. Muraki, Phys. Rev. B **91**, 245309 (2015).

[39] S. Mueller, A. N. Pal, M. Karalic, T. Tschirky, C. Charpentier, W. Wegscheider, K. Ensslin, and T. Ihn, Phys. Rev. B **92**, 081303 (R) (2015).

[40] F. Qu, A. J. A. Beukman, S. Nadj-Perge, M. Wimmer, B. M. Nguyen, W. Yi, J. Thorp, M. Sokolich, A. A. Kiselev, M. J. Manfra, C. M. Marcus, and L. P. Kouwenhoven, Phys. Rev. Lett. **115**, 036803 (2015).

[41] T. Li, P. Wang, H. Fu, L. Du, K. A. Schreiber, X. Mu, X. Liu, G. Sullivan, G. A. Csáthy, X. Li, and R. R. Du, Phys. Rev. Lett. **115**, 136804 (2015).

[42] L. Du, I. Knez, G. Sullivan, and R. R. Du, Phys. Rev. Lett. **114**, 096802 (2015).

[43] F. Nichele, H. J. Suominen, M. Kjaergaard, C. M. Marcus, E. Sajadi, J. A. Folk, F. Qu, A. J. A. Beukman, F. K. de Vries, J. v. Veen, S. Nadj-Perge. L. P. Kouwenhoven, B. M. Nguyen, A. A. Kiselev, W. Yi, M. Sokolich, M. J. Manfra, E. M. Spanton, and K. A. Moler, New. J. Phys. **18**, 083005 (2016).

[44] F. Couëdo, H. Irie, K. Suzuki, K. Onomitsu, and K. Muraki, Phys. Rev. B. **94**, 035301 (2016).

[45] T. Akiho, F. Couëdo, H. Irie, K. Suzuki, K. Onomitsu, and K. Muraki, Appl. Phys. Lett. **109**, 192105 (2016).

[46] B. M. Nguyen, A. A. Kiselev, R. Noah, W. Yi, F. Qu, A. J. A. Beukman, F. K. de Vries, J. v. Veen, S. Nadj-Perge, L. P. Kouwenhoven, M. Kjaergaard, H. J. Suominen, F. Nichele, C. M. Marcus, M. J. Manfra, and M. Sokolich, Phys. Rev. Lett. **117**, 077701 (2016).

[47] S. Mueller, C. Mittag, T. Tschirky, C. Charpentier, W. Wegscheider, K. Ensslin, and T. Ihn, Phys. Rev. B **96**, 075406 (2017).

[48] V. Mourik, K. Zuo, S. M. Frolov, S. R. Plissard, E. P. A. M. Bakkers, and L. P. Kouwenhoven, Science **336**, 6084, 1003-1007 (2012).

[49] A. Das, Y. Ronen, Y. Most, Y. Oreg, M. Heiblum, and H. Shtrikman, Nature **8**, 887–895 (2012).

[50] M. T. Deng, C. L. Yu, G. Y. Huang, M. Larsson, P. Caroff, and H. Q. Xu, Nano Lett. **12**, 12, 6414-6419 (2012).

[51] H. O. H. Churchill, V. Fatemi, K. Grove-Rasmussen, M. T. Deng, P. Caroff, H. Q. Xu, and C. M. Marcus, Phys. Rev. B **87**, 241401(R) (2013).

[52] A. D. K. Finck, D. J. Van Harlingen, P. K. Mohseni, K. Jung, and X. Li, Phys. Rev. Lett. **110**, 126406 (2013).

[53] S. Nadj-Perge, I. K. Drozdov, J. Li, H. Chen, S. Jeon, J. Seo, A. H. MacDonald, B. A. Bernevig, and A. Yazdani, Science **346**, 6209, 602-607 (2014).

[54] M. Ruby, F. Pientka, Y. Peng, F. v. Oppen, B. W. Heinrich, and K. J. Franke, Phys. Rev. Lett. **115**, 197204 (2015).

[55] W. Chang, S. M. Albrecht, T. S. Jespersen, F. Kuemmeth, P. Korgstrup, J. Nygård, and C. M. Marcus, Nat. Nanotech. **10**, 232-236 (2015).

[56] M. T. Deng, S. Vaitiekenas, E. B. Hansen, J. Danon, M. Leijnse, K. Flensberg, J. Nygård, P. Krogstrup, and C. M. Marcus, Science **354**, 6319, 1557-1562 (2016).

[57] S. Gazibegovic, D. Car, H. Zhang, S. C. Balk, J. A. Logan, M. W. A. de Moor, M. C. Caddisy, R. Schmits, D. Xu, G. Wang, P. Krogstrup, R. L. M. Op het Veld, K. Zuo, Y. Vos, J. Shen, D. Bouman, B. Shojaei, D. Pennachio, J. S. Lee, P. J. v. Veldhoven, S. Koelling, M. A. Verheijen, L. P. Kouwenhoven, C. J. Palmstrøm, and E. P. A. M. Bakkers, Nature **548**, 434-438 (2017).

[58] H. Zhang, C. X. Liu, S. Gazibegovic, D. Xu, J. A. Logan, G. Wang, N. v. Loo, J. D. S. Bommer, M. W. A. de Moor, D. Car, R. L. M. Op het Veld, P. J. v. Veldhoven, S. Koelling, M. A. Verheijen, M. Pendharkar, D. J. Pennachio, B. Shojaei, J. S. Lee, C. J. Palmstrøm, E. P. A. M. Bakkers, S. Das Sarma, and L. P. Kouwenhoven, arXiv:1710.10701.

[59] M. Kjaergaard, F. Nichele, H. J. Suominen, M. P. Nowak, M. Wimmer, A. R. Akhmerov, J. A. Folk, K. Flensberg, J. Shabani, C. J. Palmstr øm, and C. M. Marcus, Nat. Comm. **7**, 12841 (2016).

[60] J. Shabani, M. Kjaergaard, H. J. Suominen, Y. Kim, F. Nichele, K. Pakrouski, T. Stankevic, R. M. Lutchyn, P. Krogstrup, R. Feidenhans'l, S. Kraemer, C. Nayak, M. Troyer, C. M. Marcus, and C. J. Palmstrøm, Phys. Rev. B **93**, 155402 (2016).

[61] M. Kjaergaard, H. J. Suominen, M. P. Nowak, A. R. Akhmerov, J. Shabani, C. J. Palmstrøm, F. Nichele, and C. M. Marcus, Phys. Rev. App. **7**, 034029 (2017).

[62] H. J. Suominen, M. Kjaergaard, A. R. Hamilton, J. Shabani, C. J. Palmstrøm, C. M. Marcus, and F. Nichele, Phys. Rev. Lett. **119**, 176805 (2017).

[63] F. Nichele, A. C. C. Drachmann, A. M. Whiticar, E. C. T. O'Farrell, H. J. Suominen, A. Fornieri, T. Wang, G. C. Gardner. C. Thomas, A. T. Hatke, P. Krogstrup, M. J. Manfra, K. Flensberg, and C. M. Marcus, Phys. Rev. Lett. **119**, 136803 (2017).

[64] S. M. Albrecht, A. P. Higginbotham, M. Madsen, F. Kuemmeth, T. S. Jespersen, J. Nygård, P. Krogstrup, and C. M. Marcus, Nature **531**, 206–209 (2016).

[65] R. Pawlak, M. Kisiel, J. Klinovaja, T. Meier, S. Kawai, T. Glatzel, D. Loss, E. Meyer, NpJ Quantum Information **2**, 16035 (2016).

[66] X. L. Qi, T. L. Hughes, and S.-C. Zhang, Phys. Rev. B **82**, 184516 (2010).

[67] X. L. Qi, T. L. Hughes, and S.C. Zhang, Phys. Rev. B **81**, 134508 (2010).

[68] J. Alicea, Y. Oreg, G. Refael, F. Oppen, and M. P. A. Fisher, Nature Physics **7**, 412 (2011).

[69] S. Nakosai, Y. Tanaka, and N. Nagaosa, Phys. Rev. B **88**, 180503(R) (2013).

[70] J. Röntynen and T. Ojanen, Phys. Rev. Lett. **114**, 236803 (2015).

[71] T. Yoshida and Y. Yanase, Phys. Rev. B **93**, 054504 (2016).

[72] A. Daido and Y. Yanase, Phys. Rev. B **94**, 054519 (2016).
[73] J. Li, T. Neupert, Z. Wang, A. H. MacDonald, A. Yazdani, and B. A. Bernevig, Nat. Comm. **7**, 12297 (2016).
[74] G. C. Ménard, S. Guissart, C. Brun, R. T. Leriche, M. Trif, F. Debontridder, D. Demaille, D. Roditchev, P. Simon, and T. Cren, Nature **8**, 2040 (2017).
[75] L. Fu and C. L. Kane, Phys. Rev. Lett. **100**, 096407 (2008).
[76] X. L. Qi, T. L. Hughes, S. Raghu, and S. C. Zhang, Phys. Rev. Lett. **102**, 187001 (2009).
[77] M. Sato and S. Fujimoto, Phys. Rev. B **79**, 094504 (2009).
[78] L. Fu and E. Berg, Phys. Rev. Lett. **105**, 097001 (2010).
[79] C.X. Liu and B. Trauzettel, Phys. Rev. B **83**, 220510(R) (2011).
[80] S. Nakosai, Y. Tanaka, and N. Nagaosa, Phys. Rev. Lett. **108**, 147003 (2012).
[81] S. Deng, L. Viola, and G. Ortiz, Phys. Rev. Lett. **108**, 036803 (2012).
[82] F. Zhang, C. L. Kane, and E. J. Mele, Phys. Rev. Lett. **111**, 056402 (2013).
[83] F. Parhizgar and A. M. Black-Schaffer, Sci. Rep. **7**, 9817 (2017).
[84] J. Wang, Phys. Rev. B **94**, 214502 (2016).
[85] Y. Tanaka, Y. Mizuno, T. Yokoyama, K. Yada, and M. Sato, Phys. Rev. Lett. **105**, 097002 (2010).
[86] M. Sato and S. Fujimoto, Phys. Rev. Lett. **105**, 217001 (2010).
[87] M. Sato, Y. Tanaka, K. Yada, and T. Yokoyama, Phys. Rev. B **83**, 224511 (2011).
[88] Andreas P. Schnyder and Shinsei Ryu, Phys. Rev. B **84**, 060504(R) (2011).
[89] T. Meng and L. Balents, Phys. Rev. B **86**, 054504 (2012).
[90] C. L. M. Wong, J. Liu, K. T. Law, and P. A. Lee, Phys. Rev. B **88**, 060504(R) (2013).
[91] S. Deng, G. Ortiz, A. Poudel, and L.Viola, Phys. Rev. B **89**, 140507(R) (2014).
[92] A. P. Schnyder and P. M. R. Brydon, J. Phys.: Condens. Matter **27**, 243201 (2015).
[93] A. Daido and Y. Yanase, Phys. Rev. B **95**, 134507 (2017).
[94] L. Hao and C. S. Ting, Phys. Rev. B **95**, 064513 (2017).
[95] B. Huang, X. Yang, N. Xu, and M. Gong, Phys. Rev. B **97**, 045142 (2018).
[96] J. M. Byers and M. E. Flatté, Phys. Rev. Lett. **74**, 306 (1995).
[97] M. S. Choi, C. Bruder, and D. Loss, Phys. Rev. B **62**, 13569 (2000).
[98] G. Deutscher, Appl. Phys. Lett. **76**, 487 (2000).
[99] G. B. Lesovik, T. Martina, and G. Blatter, Eur. Phys. J. B **24**, 287 (2001).
[100] P. Recher, E. V. Sukhorukov, and D. Loss, Phys. Rev. B **63**, 165314 (2001).
[101] A. L. Yeyati, F. S. Bergeret, A. Martín-Rodero, and T. M. Klapwijk, Nat. Phys. **3**, 455-459 (2007).
[102] C. Reeg, J. Klinovaja, and D. Loss, Phys. Rev. B **96**, 081301(R) (2017).
[103] C. Reeg, C. Schrade, J. Klinovaja, and D. Loss, Phys. Rev. B **96**, 161407(R) (2017).
[104] M. Thakurathi, P. Simon, I. Mandal, J. Klinovaja, and D. Loss, Phys. Rev. B **97**, 045415 (2018).
[105] L. Hofstetter, S. Csonka, J. Nygård, and C. Schönenberger, Nature **461**, 960–963 (2009).
[106] A. Das, Y. Ronen, M. Heiblum, D. Mahalu, A. V. Kretinin, and Hadas Shtrikman, Nat. Comm. **3**, 1165 (2012).
[107] S. Baba, C. Jünger, S. Matsuo, A. Baumgartner, Y. Sato, H. Kamata, K. Li, S. Jeppesen, L. Samuelson, H. Xu, C. Schönenberger, S. Tarucha, arXiv:1802.08059.
[108] S. Ryu, A. P. Schnyder, A. Furusaki, A. W. W. Ludwig, New J. Phys. **12**, 065010 (2010).
[109] Y. Volpez, D. Loss, and J. Klinovaja, Phys. Rev. B **96**, 085422 (2017).
[110] D. Rainis, L. Trifunovic, J. Klinovaja, and D. Loss, Phys. Rev. B **87**, 024515 (2013).

[111] J. Klinovaja and D. Loss, Phys. Rev. B **90**, 045118 (2014).
[112] C. Schrade, M. Thakurathi, C. Reeg, S. Hoffman, J. Klinovaja, and D. Loss, Phys. Rev. B **96**, 035306 (2017).
[113] J. Klinovaja and D. Loss, Phys. Rev. B **86**, 085408 (2012).
[114] A. A. Burkov and L. Balents, Phys. Rev. Lett. **107**, 127205 (2011).
[115] Y. L. Chen et al., Science 329, 659 (2010).
[116] M. V. Hosseini and M. Askari, Phys. Rev. B 92, 224435 (2015).
[117] H. Chang, J. Zhou, S. Wang, W. Shan, and D. Xiao, Phys. Rev. B 92, 241103(R) (2015).
[118] T. S. Nunner, G. Zaránd, and Felix von Oppen, Phys. Rev. Lett. **100**, 236602 (2008).
[119] P. D. Sacramento, M. A. N. Araújo, V. R. Vieira, V. K. Dugaev, and J. Barnaś, Phys. Rev. B **85**, 014518 (2012).
[120] L. Raymond, A. D. Verga, and A. Demion, Phys. Rev. B **92**, 075101 (2015).
[121] R. A. Deutschmann, W. Wegscheider, M. Rother, M. Bichler, and G. Abstreiter, Phys. Rev. Lett. **86**, 1857 (2001).
[122] J. Nitta, T. Akazaki, H. Takayanagi, and T. Enoki, Phys. Rev. Lett. **78**, 1335 (1997).
[123] F. Dettwiler, J. Fu, S. Mack, P. J. Weigele, J. C. Egues, D. D. Awschalom, and D. M. Zumbühl, Phys. Rev. X **7**, 031010 (2017)
[124] K. S. Novoselov, A. Mishchenko, A. Carvalho, and A. H. Castro Neto, Science **353**, 6298 (2016).
[125] B. Sachs, L. Britnell, T. O. Wehling, A. Eckmann, R. Jalil, B. D. Belle, A. I. Lichtenstein, M. I. Katsnelson, and K. S. Novoselov, App. Phys. Lett. **103**, 251607 (2013).
[126] K. Novoselov, V. Fal'ko, L. Colombo, P. Gellert, M. Schwab, and K. Kim, Nature **490**, 192 (2012).
[127] A. Avsar, J. H. Lee, G. K. W. Koon, and B. Ozyilmaz, 2D Mater. **2**, 044009, (2015).
[128] B. Fülöp, Z. Tajkov, J. Pető, P. Kun, J. Koltai, L. Oroszlány, E. Tóvári, H. Murakawa, Y. Tokura, S. Bordács, L. Tapasztó, and S. Csonka, arXiv:1709.09732.
[129] P. Szumniak, D. Chevallier, D. Loss, and J. Klinovaja, Phys. Rev. B **96**, 041401 (2017).
[130] J. Klinovaja and D. Loss, Eur. Phys. J. B **88**, 62 (2015).

Chapter 5

Second-Order Topological Superconductivity in π-Junction Rashba Layers

Adapted from:
Yanick Volpez, Daniel Loss, and Jelena Klinovaja
"Second-Order Topological Superconductivity in π-Junction Rashba Layers",
Phys. Rev. Lett. **122**, 126402 (2019).

We consider a Josephson junction bilayer consisting of two tunnel-coupled two-dimensional electron gas layers with Rashba spin-orbit interaction, proximitized by a top and bottom s-wave superconductor with phase difference ϕ close to π. We show that, in the presence of a finite weak in-plane Zeeman field, the bilayer can be driven into a second order topological superconducting phase, hosting two Majorana corner states (MCSs). If $\phi = \pi$, in a rectangular geometry, these zero-energy bound states are located at two opposite corners determined by the direction of the Zeeman field. If the phase difference ϕ deviates from π by a critical value, one of the two MCSs gets relocated to an adjacent corner. As the phase difference ϕ increases further, the system becomes trivially gapped. The obtained MCSs are robust against static and magnetic disorder. We propose two setups that could realize such a model: one is based on controlling ϕ by magnetic flux, the other involves an additional layer of randomly-oriented magnetic impurities responsible for the phase shift of π in the proximity-induced superconducting pairing.

5.1 Introduction

Topological insulators and superconductors in d spatial dimensions are gapped fermionic phases with topologically protected gapless states on their $(d-1)$ - dimensional boundaries. Among the best-known examples are Majorana bound states in one-dimensional p-wave superconductors [1–4] as well as two(three)-dimensional topological insulators with an insulating bulk and metallic edges (surfaces) [5–13]. The theoretical prediction of such unconventional phases of condensed quantum matter has motivated an enormous amount of experimental and theoretical work [14–41]. Later, the concept was generalized to second order or more generally, higher order, topological insulators and superconductors [42–60]. In d spatial dimensions, these are gapped phases with topologically protected gapless states on a $(d-n)$ dimensional boundary, where n is the order of the topological phase.

Motivated by these recent developments, we propose a setup that can be controllably brought into the second order topological superconducting (SOTSC) phase. The setup is based on a heterostructure that consists of two two-dimensional electron gas (2DEG) layers with Rashba spin-orbit interaction (SOI) separated by a tunnel barrier. Each of the tunnel-coupled layers is brought into contact with an s-wave superconductor (SC) at the top and the bottom to induce the proximity superconductivity, see Fig. 5.1. Controlling the magnetic flux through the SC loop allows one to control the phase difference ϕ between the two parent SCs, and thereby, the phase difference between the proximity gaps in the two layers. Such a setup lies well within experimental reach [61, 62]. Instead of using a Josephson junction, a second possibility would be to separate one of the Rashba layers from the parent s-wave superconductor by an insulating layer of randomly oriented magnetic impurities [63]. The phase difference of π in the pairing amplitudes arises due to spin-flip tunneling via magnetic impurities [64–67].

For $\phi = \pi$ and if the tunneling term between the layers dominates over the superconducting pairings, the bilayer is in a helical topological superconducting (HTSC) phase, hosting a Kramers pair of helical edge states counterpropagating along the edges. A weak in-plane Zeeman field brings the bilayer into the second-order topological superconducting phase. The helical edge states are gapped and zero-energy Majorana bound states emerge, in rectangular geometry, at two opposite corners, referred to as Majorana corner states (MCSs). By deviating the phase difference slightly from $\phi = \pi$, the MCSs can be relocated to two adjacent corners. The presence of MCSs is robust against potential and magnetic disorder.

5.2 Model

The bilayer setup consists of two 2DEGs with strong Rashba SOI proximity coupled to bulk s-wave SCs. The top (bottom) layer is labeled by an index $\tau = 1$ ($\tau = \bar{1}$). We note that in such bilayers the SOI vectors $\boldsymbol{\alpha}_\tau$ are naturally antiparallel due to the structural asymmetry (see Fig. 5.1) and aligned along the z axis defined to be the normal to the layers [68]. The Hamiltonian for a Rashba layer reads

$$H_\tau = \sum_{\sigma,\sigma'} \int d^2k \; \psi^\dagger_{\tau\sigma,\mathbf{k}} \Big[\varepsilon_k - \mu_\tau + \boldsymbol{\alpha}_\tau \cdot \boldsymbol{\sigma} \times \boldsymbol{k} \Big]_{\sigma\sigma'} \psi_{\tau\sigma',\mathbf{k}} \,, \tag{5.2.1}$$

where $\boldsymbol{k} = (k_x, k_y)$ is the in-plane momentum, $\varepsilon_k = \hbar^2 k^2/2m$ the kinetic energy, m the effective mass, and $\boldsymbol{\sigma}$ the vector of Pauli matrices acting in spin space. The creation operator $\psi^\dagger_{\tau\sigma,\boldsymbol{k}}$ creates an electron with spin projection along the z axis $\sigma = \{1, \bar{1}\} \equiv \{\uparrow, \downarrow\}$ and in-plane momentum $\boldsymbol{k}$ located in layer $\tau = \{1, \bar{1}\}$. The SOI energy $E_{\tau,so} = \hbar^2 k^2_{so,\tau}/2m$, with $k_{so,\tau} = m\alpha_\tau/\hbar^2$ being the SOI momentum, is the energy difference between band bottom and degeneracy point at $k = 0$ where the Rashba bands cross. The chemical potential μ_τ is taken from this degeneracy point, i.e. $\mu_\tau = 0$ at $k = 0$.

The coupling between the two Rashba layers is described by

$$H_\Gamma = \Gamma \sum_\sigma \int d^2k \, \Big(\psi^\dagger_{1\sigma,\boldsymbol{k}} \psi_{\bar{1}\sigma,\boldsymbol{k}} + \text{H.c.} \Big), \tag{5.2.2}$$

where the spin-conserving tunneling amplitude Γ is assumed to be positive. The proximity induced superconductivity is described by

$$H_\Delta = \frac{1}{2} \sum_{\tau,\sigma,\sigma'} \int d^2k \, \Big(\Delta_\tau \psi^\dagger_{\tau\sigma,\boldsymbol{k}} [i\sigma_2]_{\sigma\sigma'} \psi^\dagger_{\tau\sigma',-\boldsymbol{k}} + \text{H.c.} \Big), \tag{5.2.3}$$

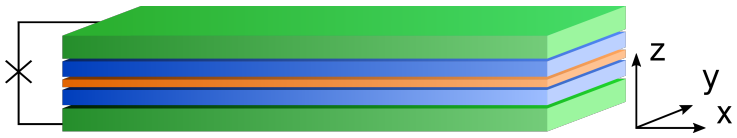

Figure 5.1: Schematics of the bilayer setup consisting of two 2DEG Rashba layers (blue) separated by a tunnel barrier (orange) and coupled to s-wave superconductors (green) that form a Josephson junction. The two Rashba SOI vectors are aligned in opposite directions due to the structural asymmetry. A magnetic flux ensures a phase difference in the proximity-induced superconductivity between two layers. Alternatively, the phase difference of π can be induced by an additional layer of randomly oriented magnetic impurities placed between one of the SC and the Rashba layer.

where we assume the pairing amplitude Δ_1 in the top layer to be real and positive, while the pairing amplitude in the second layer can be complex $\Delta_{\bar{1}} = |\Delta_{\bar{1}}|e^{i\phi}$. There are several mechanisms that can produce a phase difference ϕ. A superconducting loop connecting two SCs enclosing a magnetic flux ϕ (see Fig. 5.1) forms a Josephson junction [61, 62, 69, 70], that allows one to tune the superconducting phase difference ϕ between the two Rashba layers. Alternatively, such a setup could be realized by involving an insulating layer of random magnetic impurities [63] between a SC and one of the Rashba layers, such that the superconducting phase difference between two Rashba layers is equal to π and does not require any fine-tuning necessary in the first setup.

We also account for the presence of an in-plane Zeeman field of strength Δ_Z applied along the unit vector $\boldsymbol{n} = (\cos\theta, \sin\theta, 0)$. The corresponding term in the Hamiltonian is given by

$$H_Z = \Delta_Z \sum_{\tau,\sigma,\sigma'} \int d^2k \; \psi^\dagger_{\tau\sigma,\boldsymbol{k}} [\boldsymbol{n}\cdot\boldsymbol{\sigma}]_{\sigma\sigma'} \psi_{\tau\sigma',\boldsymbol{k}} \,. \tag{5.2.4}$$

The total Hamiltonian reads $H = H_1 + H_{\bar{1}} + H_\Gamma + H_\Delta + H_Z \equiv H_0 + H_Z$. Next, we solve H numerically for two geometries. (i) Semi-infinite geometry: The system is translationally invariant along the x direction (with momentum k_x as good quantum number) and finite along the y direction of length L_y. (ii) Finite geometry: The system is finite in both, the x and y, directions and of size $L_x \times L_y$, where L_x is the length of the system in the x direction. In what follows, we present the key results of the numerical diagonalization of H, while the specific form of the discretized Hamiltonians can be found in Appendix 5.A.

5.3 Topological Phase Diagram of π-Junction

If $\Delta_Z = 0$ and $\phi = \pi$, the system is in the DIII symmetry class [71]. The effective time-reversal (particle-hole) symmetry operator is given by $\Theta = i\sigma_2\mathcal{K}$ ($\mathcal{P} = \eta_1\mathcal{K}$), where η_i are the Pauli matrices acting in particle-hole space and $\mathcal{K}$ is the complex conjugation operator, see Appendix 5.B. The corresponding bulk spectrum of H_0 is given by

$$E^2_\pm(k) = \varepsilon_k^2 + \Delta^2 + \Gamma^2 + (\alpha k)^2 \pm 2\sqrt{\varepsilon_k^2[\Gamma^2 + (\alpha k)^2] + \Delta^2\Gamma^2} \,. \tag{5.3.1}$$

For simplicity we set $\Delta_1 = |\Delta_{\bar{1}}| = \Delta > 0$ and $|\boldsymbol{\alpha}_1| = |\boldsymbol{\alpha}_{\bar{1}}| = \alpha > 0$, however, we note that our results remain valid in the more general case where these quantities are unequal (see Appendix 5.B). The bulk gap closes at $k = 0$ for $\Gamma = \Delta$. For $\Gamma = 0$, the system consists of uncoupled layers, and, thus, is in the trivial phase for $\Gamma < \Delta$, see

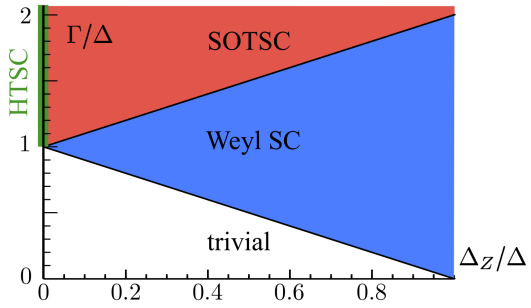

Figure 5.2: Topological phase diagram of the π-junction bilayer as a function of tunnel amplitude Γ and Zeeman energy Δ_Z. Topological phase transitions occur at $\Gamma = |\Delta_Z \pm \Delta|$ (black lines). For $\Delta_Z = 0$ and $\Gamma > \Delta$, the system is in the HTSC phase (green line) hosting a Kramers pair of helical edge states. For $\Delta_Z < \Delta$ and $\Gamma > |\Delta + \Delta_Z|$, the system is in the SOTSC phase (red) hosting at two of the corners each a MCS. For $|\Delta_Z - \Delta| < \Gamma < |\Delta_Z + \Delta|$, the system is in the Weyl SC phase (blue) hosting flat zero-energy edge states. Otherwise, the system is in the trivial phase (white).

Fig. 5.2. In the regime $\Gamma > \Delta$, the system has a Kramers pair of gapless helical edge states on both boundaries ($y = 0$ and $y = L_y$) in the semi-infinite geometry and on each boundary in the finite geometry, see Fig. 5.3. These states are exponentially localized at the boundary and have a linear dispersion around $k_x = 0$. We note that the boundaries between different phases found at $k = 0$ do not depend on the strength of SOI. However, the presence of SOI is crucial for the topological phases since without it the system would be gapless at some finite momentum if $\Gamma > \Delta$.

Zeeman fields break time-reversal symmetry such that the Hamiltonian H is placed now in the D symmetry class [71]. For strong Zeeman field, $\Delta_Z > \Delta$, superconductivity is suppressed such that the system becomes gapless with the gap closing at finite momenta. At smaller fields, the bulk gap closes at $k = 0$ for $\Gamma = |\Delta_Z \pm \Delta|$, indicating a topological phase transition. Obviously, at weak fields, $\Gamma < \Delta - \Delta_Z$, the system stays trivial. If $\Delta - \Delta_Z < \Gamma < \Delta + \Delta_Z$, the system is in a 2D Weyl SC phase [72–81] (see Fig. 5.2), with two Weyl cones emerging in the spectrum in direction orthogonal to the Zeeman field. The nodes of these two Weyl cones are connected in momentum space by a zero-energy line describing localized dispersionless edge states. The zero-energy edge states occur only at edges where the nodes of the Weyl cones are not projected onto the same point (see Appendix 5.C).

Next, we focus on the SOTSC phase, $\Gamma > \Delta + \Delta_Z$. Generally, finite Δ_Z opens a gap in the spectrum of the helical edge states of the HTSC phase. The size of the gap depends on the field direction $\boldsymbol{n}$ [82] (see Fig. 5.4). For simplicity, we consider

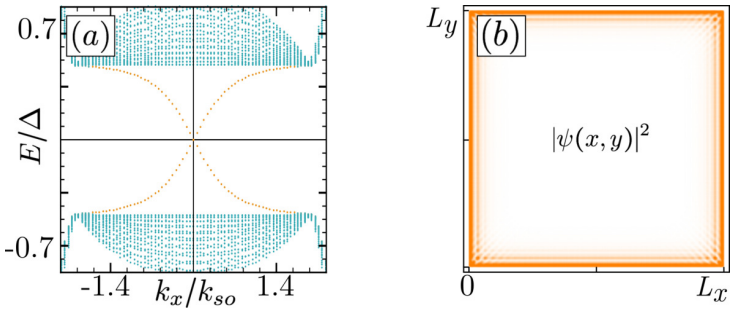

Figure 5.3: (a) Energy spectrum in the HTSC phase ($\Gamma > \Delta$) for semi-infinite geometry, obtained by exact diagonalization. The bulk states (green dots) are gapped, while both edges host a Kramers pair of dispersive helical edge states (orange dots). (b) Color plot of the probability density $|\psi(x,y)|^2$ of a helical edge state in the finite geometry. The states are exponentially localized at the edge (yellow strips). Numerical parameters: $k_{so}L_x = k_{so}L_y \approx 860$, $\mu = 0$, $\Delta/E_{so} \approx 0.2$, $\phi = \pi$, and $\Gamma/E_{so} \approx 0.6$.

samples of rectangular geometry. For fields not parallel to the sample edges, the helical edge states are gapped out. More importantly, two non-degenerate bound states emerge at zero-energy which we can identify as Majorana corner states, each localized at opposite corners, see Fig. 5.4. The localization length of such MCSs along the edges is inversely proportional to the gap [83, 84]. If the system possesses, in addition, mirror symmetry [$\theta = (2p+1)\pi/4$], the localization lengths along x and y axis are the same. As the field deviates from these directions, the localization length along the axis with the smallest gap increases [see Fig. 5.4(a)] up to the point where the two edges are no longer gapped as the field is aligned along one of edges [see Fig. 5.4(b)]. If the field is rotated further, the MCSs re-emerge at the other two opposite corners.

Generally, the existence of the two MCSs does not rely on symmetries of the square lattice, nor on the particular shape of the boundary. If the system, *e.g.*, has a circular shape, the two MCSs are localized at the two opposite points where the Zeeman vector $\boldsymbol{n}$ crosses the edge. We also checked numerically that MCSs are robust against moderate potential and magnetic disorder (see Appendix 5.D). We can also easily create more than two MCSs by modifying the topology of our setup. For instance, we can allow for a region inside the system to be in the trivial phase, giving rise to an inner boundary at the interface with corresponding edge states. Such a region could be fabricated by covering, say, the top Rashba layer with a SC layer with, *e.g.*, a rectangular hole. Without Zeeman fields, helical edge states propagate along the outer and inner edges, while for $\Delta_Z > 0$, these states get gapped and four MCSs emerge, two at the outer and two at the inner corners,

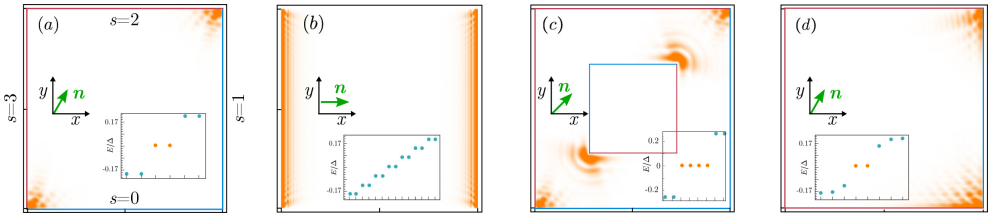

Figure 5.4: Color plots of probability density and spectrum (insets) of low-energy states in SOTSC phase. (a) If the field direction $\boldsymbol{n}$ has projection on both edges as well as $|\delta\phi| < \min\{\delta\phi_{c,\parallel}, \delta\phi_{c,\perp}\}$ (here, $\theta = \pi/3$ and $\delta\phi = 0$), the zero-energy MCSs (yellow dots in inset) are separated from bulk states (blue dots in inset) by the gap and are located at two opposite corners. For $0 < \theta < \pi/2$, the sign of the gap Δ_s on the $s = 0, 1$ ($s = 2, 3$) edge is positive (negative) and shown in blue (red): thus, the lower left (upper right) corner acts as domain wall at which MCSs are localized. (b) If $|\delta\phi| = \delta\phi_{c,\parallel/\perp}$ (here, $\theta = 0$ and $\delta\phi = \phi_{c,\perp} = 0$), the helical edge states propagating along the corresponding edge stays gapless. The other edges are still gapped. (c) A trivial square region in the center (of the size $L_x/2 \times L_x/2$) leads to two additional MCSs localized at the inner corners. (d) If $\min\{\delta\phi_{c,\parallel}, \delta\phi_{c,\perp}\} < |\delta\phi| < \max\{\delta\phi_{c,\parallel}, \delta\phi_{c,\perp}\}$ (here $\theta = \pi/3$ and $\delta\phi \approx \pi/3$), only the sign of the gap on the $s = 1$ edge is positive. As a result, the two MCSs are located now at two neighboring corners. Numerical parameters are the same as in Fig. 5.3, except $k_{so}L_x = k_{so}L_y = 430$ and $\Delta_Z/E_{so} = 0.15$.

see Fig. 5.4(c).

5.4 Analytical Treatment and Stability of MCSs

In order to obtain a deeper understanding for the appearance of the MCSs at the two particular corners, we treat the problem analytically. We assume that the system size is large enough to treat all four edges, away from the corners, independently. For simplicity, we focus on rectangular geometries and label the edges counterclockwise by $s = 0, 1, 2, 3$ with $s = 0$ being the horizontal edge at $y = 0$ (see Fig. 5.4). The effective Hamiltonian describing the helical edge states is given by

$$\mathcal{H}_{eff}^{(s)} = \hbar v k^{(s)} \beta_3 - \Delta_s \beta_2, \tag{5.4.1}$$

where v is the effective Fermi velocity of the edge states, $k^{(s)}$ the momentum along the sth edge, β_i the Pauli matrices acting on the low-energy subspace, and Δ_s is the gap opened on the sth edge if time-reversal symmetry is broken. We also note that the Hamiltonian without Zeeman field, H_0 [see Eqs. (5.2.1)-(5.2.3)], has rotational symmetry around the z-axis, $[H_0, U_\varphi] = 0$, where $U_\varphi = e^{i\varphi\eta_3 J_z/\hbar}$. Here, $J_z = L_z + S_z$ is the z component of the total angular momentum composed of spin

$S_z = \hbar\sigma_3/2$ and orbital angular momentum $L_z = -i\hbar(x\partial_y - y\partial_x)$. At the edges, this symmetry reduces to a fourfold rotational symmetry with $\varphi_s = s\pi/2$. Thus, the states localized at the sth edge are related to those at $s = 0$ by the unitary U_{φ_s}. For example, $\Phi_\pm^{(s)} = U_{\varphi_s}\Phi_\pm^{(0)}$, where $\Phi_\pm^{(s)}$ are the sth edge state wavefunctions at $k^{(s)} = 0$ (see Appendix 5.E). This rotational symmetry ensures that the effective Fermi velocity is the same at all edges.

So far, we focused on the phase difference being tuned to $\phi = \pi$. This is important for observing the helical edge states protected by time-reversal symmetry but not necessary for observing the MCSs. The SOTSC phase and MCSs are robust against small deviations of the phase difference $\phi = \pi + \delta\phi$, which is of great importance for the scenario in which this phase is tuned by magnetic fluxes. For finite $\delta\phi$ ($|\delta\phi| \ll 1$), the bulk spectrum stays almost the same, while the helical edge states become gapped at $k^{(s)} = 0$. The size of the gap for $\delta\phi \neq 0$ can be determined in first order perturbation theory by calculating the expectation value of the corresponding part of H_Δ, $\langle\Phi_+^{(s)}|\delta H_\Delta|\Phi_-^{(s)}\rangle$. The gap, $\Delta_s = -\Delta\sin(\phi)/2 \approx \Delta\delta\phi/2$, is the same on all edges due to rotation symmetry (see Appendix 5.F).

As discussed above, a Zeeman field also opens a gap in the spectrum of edge states at $k^{(s)} = 0$. Since the edge states at $s = 0$ have a well-defined spin projection along y, only the x-component of the field can lead to a gap given by $-i\langle\Phi_+^{(0)}|\mathcal{H}_Z|\Phi_-^{(0)}\rangle = \Delta_Z\cos\theta$. The Zeeman term $\mathcal{H}_Z$ defined in Eq. (5.2.4) is not invariant under rotations, $U_{\varphi_s}^\dagger\mathcal{H}_Z U_{\varphi_s} = \Delta_Z[\cos(\theta-\varphi_s)\eta_3\sigma_1 + \sin(\theta-\varphi_s)\sigma_2]/2$. Thus, the gap in the edge state spectrum opened by $\mathcal{H}_Z$ is different at different edges and is given by $\Delta_Z\cos(\theta-\varphi_s)$ (see Appendix 5.F).

Combining the two complementary mechanisms gapping the helical edge states, we find that the gap on the sth edge is given by $\Delta_s = \Delta\delta\phi/2 + \Delta_Z\cos(\theta-\varphi_s)$. The edges are gapped except if $\delta\phi = \pm\delta\phi_{c,\parallel/\perp}$, where the gap closes at the horizontal ($\delta\phi_{c,\parallel} = 2\Delta_Z|\cos\theta|/\Delta$) or vertical ($\delta\phi_{c,\perp} = 2\Delta_Z|\sin\theta|/\Delta$) edges. The effective Hamiltonian $\mathcal{H}_{eff}^{(s)}$ brings us back to the first topological models of Jackiw-Rebbi type [85, 86]. The mass term Δ_s, opening the gap, can change its sign at a corner where two edges meet. As a result, there is a zero-energy bound state located at this effective domain wall with the localization length $\xi_s \approx \hbar v/|\Delta_s|$, which we identify as a MCS. Importantly, the details of the parameter dependence at the domain wall is not important and only the asymptotics away from it matters. This allows us to rely on the effective $\mathcal{H}_{eff}^{(s)}$ derived away from the corners.

There are three regimes to consider. If $|\delta\phi| > \max\{\delta\phi_{c,\parallel}, \delta\phi_{c,\perp}\}$, the mass term Δ_s is either positive or negative on all edges, since the uniform gap opened by $\delta\phi$ dominates. In this case, there are no domain walls and thus no MCSs. If

$|\delta\phi| < \min\{\delta\phi_{c,\parallel}, \delta\phi_{c,\perp}\}$, the gap due to the Zeeman field dominates and there are two domain walls that lie on opposite corners along the diagonal [see Fig. 5.4(a)]. In the intermediate regime, $\min\{\delta\phi_{c,\parallel}, \delta\phi_{c,\perp}\} < |\delta\phi| < \max\{\delta\phi_{c,\parallel}, \delta\phi_{c,\perp}\}$, the domain walls, and as result the MCSs, are located on neighboring corners [see Fig. 5.4(d)]. Thus, the MCSs exist for a wide range of $\delta\phi$ and their location is governed by both the Zeeman field and $\delta\phi$. While the analytical treatment was done perturbatively, the conditions on the existence of MCSs as well as their location can be confirmed numerically well beyond the perturbative regime, see Fig. 5.4.

5.5 Conclusions

We studied a bilayer Josephson junction consisting of two tunnel coupled 2DEGs with opposite Rashba SOI and proximity-induced superconducting pairing amplitudes that have a phase difference $\phi \approx \pi$. Alternatively, since the spectrum of the uncoupled layers around $k = 0$ is essential for the topological properties of the system, instead of two Rashba layers with opposite SOI separated by a tunneling barrier, one could also use a thin film of a 3D topological insulator [87]. There, the surface states on opposite surfaces have opposite helicity and therefore have the same spectrum around $k = 0$ as in the Rashba bilayer setup. If tunneling between layers dominates over the superconducting pairings with the phase difference close to π and a weak in-plane Zeeman field is applied, the system is in a SOTSC phase hosting two MCSs that are robust against both potential and magnetic disorder.

Acknowledgments. This work was supported by the Swiss National Science Foundation and NCCR QSIT. This project received funding from the European Union's Horizon 2020 research and innovation program (ERC Starting Grant, grant agreement No 757725). We acknowledge helpful discussions with Christopher Reeg and Katharina Laubscher.

5.A Discretized Lattice Models

In the main text we present our numerical results for the semi-infinite and the finite geometries in which the Rashba bilayer system is assumed to have a rectangular shape. In this section we explicitly discretize the total Hamiltonian H defined by Eqs. (5.2.1)-(5.2.4) of the main text.

Semi-Infinite Geometry

In the semi-infinite geometry, we assume, without loss of generality, that the system is translationally invariant along the x and finite along the y direction with the length $L_y = (N_y - 1)a$, where N_y is the number of lattice sites in y-direction and a the lattice constant. The total Hamiltonian for the semi-infinite geometry is given by $\bar{H}' = \sum_{k_x}[\bar{H}'_1(k_x) + \bar{H}'_{\bar{1}}(k_x) + \bar{H}'_\Gamma(k_x) + \bar{H}'_D(k_x) + \bar{H}'_Z(k_x)]$ with

$$\begin{aligned}
\bar{H}'_\tau(k_x) &= \sum_m \Big\{ \sum_\sigma \Big(-t c^\dagger_{k_x\tau(m+1)\sigma} c_{k_x\tau m\sigma} + [-t\cos(k_x a) + \mu_\tau/2 + 2t] c^\dagger_{k_x\tau m\sigma} c_{k_x\tau m\sigma} \Big) \\
&\quad + \tau\tilde{\alpha}\Big[i(c^\dagger_{k_x\tau(m+1)\uparrow} c_{k_x\tau m\downarrow} - c^\dagger_{k_x\tau(m-1)\uparrow} c_{k_x\tau m\downarrow}) + 2i\sin(k_x a) c^\dagger_{k_x\tau m\uparrow} c_{k_x\tau m\downarrow} \Big] + \text{H.c.} \Big\}, \\
\bar{H}'_\Gamma(k_x) &= \Gamma \sum_\sigma \sum_m \Big(c^\dagger_{k_x 1\sigma m} c_{k_x \bar{1}\sigma m} + \text{H.c.} \Big), \\
\bar{H}'_D(k_x) &= \frac{1}{2} \sum_{\tau,m} \sum_{\sigma,\sigma'} \Big(\Delta_\tau c^\dagger_{k_x\tau m\sigma} [i\sigma_2]_{\sigma\sigma'} c^\dagger_{-k_x\tau m\sigma'} + \text{H.c.} \Big), \qquad (5.A.1) \\
\bar{H}'_Z(k_x) &= \Delta_Z \sum_{\tau,m} \sum_{\sigma,\sigma'} c^\dagger_{k_x\tau m\sigma} [\boldsymbol{n}\cdot\boldsymbol{\sigma}]_{\sigma\sigma'} c_{k_x\tau m\sigma'}. \qquad (5.A.2)
\end{aligned}$$

The operator $c^\dagger_{k_x\tau\sigma m}$ creates an electron with momentum k_x and spin projection σ (along z axis) in the layer τ at the lattice site m. Here, t is the amplitude for a hopping process between two neighboring lattice sites used to set the effective mass as $t = \hbar^2/(2ma^2)$. The spin-flip hopping amplitude $\tilde{\alpha}$ is related to the SOI parameter by $\tilde{\alpha} = \alpha/2a$. The spin-orbit energy E_{so} is given by $E_{so} = \tilde{\alpha}^2/t$ [88, 89].

Finite Rectangular Geometry

In the finite geometry we assume the system to be finite in both x and y directions and of size $L_x \times L_y = (N_x - 1)(N_y - 1)a^2$. The indices (n, m) label sites in the two-dimensional square lattice with $n \in \{1, \ldots, N_x\}$ and $m \in \{1, \ldots, N_y\}$. The total

Hamiltonian $\bar{H} = \bar{H}_1 + \bar{H}_{\bar{1}} + \bar{H}_\Gamma + \bar{H}_D + \bar{H}_Z$ in the finite geometry is then given by

$$\begin{aligned}
\bar{H}_\tau &= \sum_{n,m}\Big\{\sum_\sigma\Big(-t_x c^\dagger_{\tau\sigma(n+1)m}c_{\tau\sigma nm} - t_y c^\dagger_{\tau\sigma n(m+1)}c_{\tau\sigma nm} + \frac{\mu_\tau + 4t}{2}c^\dagger_{\tau\sigma nm}c_{\tau\sigma nm} + \text{H.c.}\Big) \\
&\quad + \tau\tilde{\alpha}\Big[i(c^\dagger_{\tau\uparrow n(m+1)}c_{\tau\downarrow nm} - c^\dagger_{\tau\uparrow n(m-1)}c_{\tau\downarrow nm}) \\
&\qquad - (c^\dagger_{\tau\uparrow(n+1)m}c_{\tau\downarrow nm} - c^\dagger_{\tau\uparrow(n-1)m}c_{\tau\downarrow nm}) + \text{H.c.}\Big]\Big\}, \\
\bar{H}_\Gamma &= \Gamma\sum_{\substack{\sigma\\ n,m}}\Big(c^\dagger_{1\sigma nm}c_{\bar{1}\sigma nm} + \text{H.c.}\Big), \\
\bar{H}_\Delta &= \frac{1}{2}\sum_{\substack{\tau\\ n,m}}\sum_{\sigma,\sigma'}\Big(\Delta_\tau c^\dagger_{\tau\sigma nm}[i\sigma_2]_{\sigma\sigma'}c^\dagger_{\tau\sigma' nm} + \text{H.c.}\Big), \qquad (5.A.3) \\
\bar{H}_Z &= \Delta_Z\sum_{\substack{\tau\\ n,m}}\sum_{\sigma,\sigma'}c^\dagger_{\tau\sigma nm}[\boldsymbol{n}\cdot\boldsymbol{\sigma}]_{\sigma\sigma'}c_{\tau\sigma' nm}\,. \qquad (5.A.4)
\end{aligned}$$

The operator $c^\dagger_{\tau\sigma nm}$ creates an electron with spin projection σ in the layer τ at the lattice site (n,m). Note that $\bar{H}'$ in the semi-infinite geometry can be obtained from $\bar{H}$ by applying a Fourier transformation in the x direction.

5.B Phase Diagram for $\Delta_1 \neq \Delta_{\bar{1}}$ and $\alpha_1 \neq \alpha_{\bar{1}}$

In the main text, for analytical simplicity, we have assumed that $\Delta_1 = \Delta_{\bar{1}}$ and $\alpha_1 = \alpha_{\bar{1}}$. However, we have emphasized that the topological phase diagram stays essentially the same even if $\Delta_1 \neq \Delta_{\bar{1}}$ and $\alpha_1 \neq \alpha_{\bar{1}}$. Here, we confirm this statement both analytically and numerically.

First, we show that our setup obeys particle-hole symmetry. For a general system obeying particle-hole symmetry with a corresponding Hamiltonian H we must find an operator C such that [71]

$$H(\boldsymbol{k}) = -CH^*(-\boldsymbol{k})C^{-1}. \qquad (5.B.1)$$

The total Hamiltonian describing our system [see Eqs. (5.2.1)-(5.2.4)], compactly expressed in momentum space in terms of Pauli matrices, reads

$$\begin{aligned}
H(k_x,k_y) &= \eta_3\frac{\hbar^2k^2}{2m} + \tau_3\alpha(k_y\sigma_1 - k_x\eta_3\sigma_2) + \Gamma\tau_1\eta_3 + \Delta_1(1+\tau_3)\eta_2\sigma_2/2 \\
&\quad + \Delta_{\bar{1}}\cos(\phi)\frac{1-\tau_3}{2}\eta_2\sigma_2 - \Delta_{\bar{1}}\sin(\phi)\frac{1-\tau_3}{2}\eta_1\sigma_2, \qquad (5.B.2)
\end{aligned}$$

where τ_i, η_i, and σ_i are Pauli matrices acting in layer, particle-hole, and spin space, respectively. One can easily check that the above definition of particle-hole symmetry, Eq. (5.B.1), is fulfilled independent of the specific values of Δ_1, $\Delta_{\bar{1}}$, and

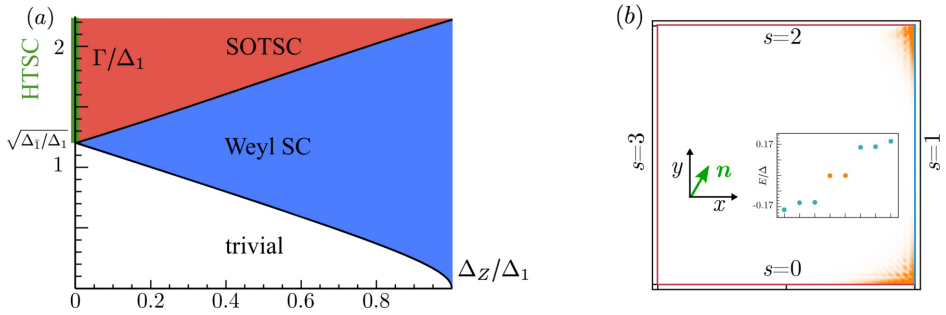

Figure 5.5: (a) Topological phase diagram of the π-junction bilayer as a function of the tunnel amplitude Γ and the Zeeman energy Δ_Z in the regime where the proximity-induced pairing amplitudes are unequal, $\Delta_1 \neq \Delta_{\bar{1}}$ (here $\Delta_{\bar{1}} = 1.5\Delta_1$). The boundaries between different topological phase transitions are given by $\Gamma_\pm^2 = \Delta_1\Delta_{\bar{1}} + \Delta_Z^2 \pm \Delta_Z(\Delta_1 + \Delta_{\bar{1}})$ (black lines). For $\Delta_Z = 0$ and $\Gamma > \sqrt{\Delta_1\Delta_{\bar{1}}}$, the system is in the HTSC phase (green line) hosting a Kramers pair of helical edge states. For $\Delta_Z < \min\{\Delta_1, \Delta_{\bar{1}}\}$ and $\Gamma > \Gamma_+$, the system is in the SOTSC phase (red) hosting a MCS each at two of the four corners. For $\Gamma_- < \Gamma < \Gamma_+$, the system is in the Weyl SC phase (blue) hosting unidirectional edge states. Otherwise, the system is in the trivial phase (white). (b) Color plot of probability density and spectrum (inset) of low-energy states in the SOTSC phase. Two MCSs are hosted at two neighboring corners. The numerical parameters are chosen to be the same as in Fig. 5.4(d) of the main text except that here $E_{so,\bar{1}} = 2E_{so,1}$ and $\Delta_{\bar{1}} = 2\Delta_1$.

ϕ, with C being explicitly given by $C = \eta_1$. At the same time, using the condition for time-reversal symmetry [71],

$$H(\boldsymbol{k}) = TH^*(-\boldsymbol{k})T^{-1}, \tag{5.B.3}$$

one can see that this equation is only fulfilled if $\sin\phi = 0$ with $T = \sigma_1$. This means that deviations from $\phi = n\pi$ (n integer) break time-reversal symmetry. However, this does not cause any issues, since in our system time-reversal symmetry has to be broken anyway in order to achieve the second-order topological phase. Indeed, only time-reversal symmetry breaking terms can gap the edge states in the helical topological superconducting phase.

To determine the topological phase diagram of the π-junction Rashba bilayer setup, we again focus on the bulk gap closing at $k = 0$ which now occurs along the lines

$$\Gamma_\pm^2 = \Delta_1\Delta_{\bar{1}} + \Delta_Z^2 \pm \Delta_Z(\Delta_1 + \Delta_{\bar{1}}). \tag{5.B.4}$$

The topological phases remain essentially unchanged as we have also checked numerically [see Fig. 5.5(a)]. At $\Delta_Z = 0$, the gapless helical edge states emerge at $\Gamma = \sqrt{\Delta_1\Delta_{\bar{1}}}$. In the absence of tunneling, $\Gamma = 0$, the trivial gapped phase extends up to $\Delta_Z = \min\{\Delta_1, \Delta_{\bar{1}}\}$. Numerically, we again confirm the presence of MCSs in

the SOTSC part of the phase diagram, $\Gamma > \Gamma_+$ [see Fig. 5.5(b)]. From Eq. (5.B.4) above we also recover the special case $\Delta_1 = \Delta_{\bar{1}}$ and $\alpha_1 = \alpha_{\bar{1}}$ considered analytically in the main text. In the general case $\Delta_1 \neq \Delta_{\bar{1}}$ and $\alpha_1 \neq \alpha_{\bar{1}}$, the properties of the edge states in the region referred to as Weyl SC phase and defined by $\Gamma_- < \Gamma < \Gamma_+$ are modified. Due to the loss of symmetry, the Weyl nodes are no longer pinned to zero energy but shifted against each other to small but finite energy. As a result, the formerly flat zero-energy edge states connecting the two Weyl nodes have now a finite slope and become so-called unidirectional edge states [77, 78, 82].

5.C 2D Weyl Superconductor

As discussed in the main text, in the regime $|\Delta_Z - \Delta| < \Gamma < |\Delta_Z + \Delta|$, the system is a 2D Weyl superconductor [72–80]. The bulk spectrum is closed at two nodes around which the bulk spectrum is linear, *i.e.*, the low-energy spectrum can be described by 2D Weyl cones. The position of the Weyl cones in momentum space is such that the line connecting the two cones is orthogonal to the direction of the Zeeman field. As already mentioned in the main text, in a Weyl superconductor (as well as in a Weyl semimetal) edge states only occur on edges at which the nodes of the two Weyl cones (being projected onto the edge) are not projected onto the same point. This means that the occurrence of edge states at the given edge in the 2D Weyl superconducting phase depends on the orientation $\boldsymbol{n}$ of the Zeeman field. In momentum space, the edge states appear on a line connecting the nodes of the Weyl cones, and since they are at zero energy, the corresponding edge states are flat (see Fig. 5.6).

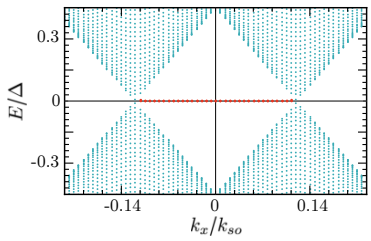

Figure 5.6: The energy spectrum in the 2D Weyl SC phase in the semi-infinite geometry. The Zeeman field is applied along the y direction such that the Weyl nodes are located at the k_x axis in momentum space. The bulk spectrum (blue dots) closes the gap at zero energy at two nodes, which are connected by dispersionless edge states (red). Numerical parameters are $k_{so}L_x \approx 4290$, $\mu = 0$, $\Delta/E_{so} \approx 0.2$, $\phi = \pi$, $\Gamma/E_{so} \approx 0.2$, and $\Delta_Z/E_{so} \approx 0.1$.

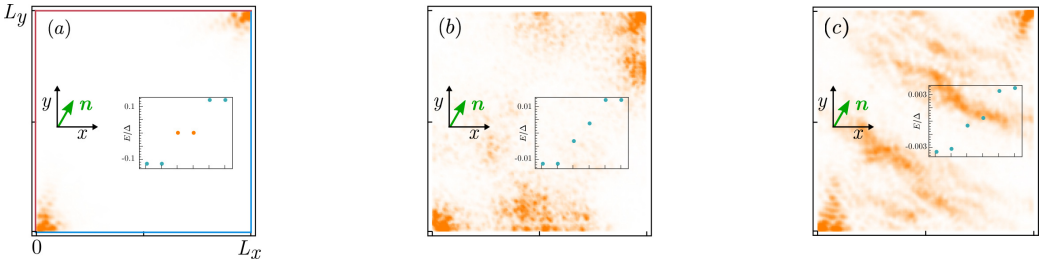

Figure 5.7: (a) The SOTSC phase is stable against fluctuations in chemical potential (potential disorder) and in Zeeman field (magnetic disorder). Here, we choose $\overline{\sigma}_\mu/E_{so} \approx 0.4$ and $\overline{\sigma}_Z/E_{so} \approx 0.1$. (b) If the static potential disorder strength is as large as $\overline{\sigma}_\mu/E_{so} \approx 1.6$, the bulk gap closes and, consequently, the MCSs disappear. (c) The same happens if the magnetic disorder strength is as large as $\overline{\sigma}_Z/E_{so} \approx 0.4$. Numerical parameters are the same as in Fig. 5.4(a): $k_{so}L_x = k_{so}L_y = 430$, $\mu = 0$, $\Delta/E_{so} = 0.2$, $\Delta_Z/E_{so} = 0.15$, $\Gamma/E_{so} = 0.6$, $\theta = \pi/3$, and $\delta\phi = 0$ (corresponding to $N_x = N_y = 150$, $\mu = 0$, $\Delta/t = 0.06$, $\Delta_Z/t = 0.05$, $\Gamma/t = 0.17$, $\theta = \pi/3$, and $\delta\phi = 0$ in the tight-binding model).

5.D Stability of Majorana Corner States Against Disorder

In this section, we show numerically that the SOTSC phase is stable against fluctuations of the local chemical potential (potential disorder) and of Zeeman field (magnetic disorder), see Fig. 5.7.

Potential Disorder

In the considerations above we assumed the chemical potential to be fixed at the SOI energy, *i.e.*, $\mu = 0$. In the presence of scalar impurities the local potential can fluctuate around this value, which can be taken into account by introducing local fluctuations $\delta\mu_{ij}$ at lattice site (i, j) that follow a normal distribution with zero mean value, *i.e.*, $\langle\delta\mu_{ij}\rangle = 0$. The strength of the potential fluctuations is characterized by the standard deviation $\overline{\sigma}_\mu = \sqrt{\langle\delta\mu_{ij}^2\rangle}$.

Magnetic Disorder

Magnetic impurities create local fluctuations in the effective Zeeman field. As for potential disorder, this can be taken into account by introducing the local deviation from the Zeeman field $\boldsymbol{h}_{ij} = (h_{x,ij}, h_{y,ij}, h_{z,ij})$, where each component separately follows a normal distribution with the corresponding mean values, *i.e.* $\langle h_{x,ij}\rangle = \Delta_Z \cos\theta$, $\langle h_{x,ij}\rangle = \Delta_Z \sin\theta$, $\langle h_{z,ij}\rangle = 0$, and the standard deviation $\overline{\sigma}_Z = \sqrt{\langle \boldsymbol{h}_{ij}^2\rangle - \langle \boldsymbol{h}_{ij}\rangle^2}$. We find that the SOTSC phase is robust against strong potential disorder characterized by $\overline{\sigma}_\mu$ substantially exceeding the bulk gap. However, if

disorder is too strong, the bulk gap closes and the system becomes effectively gapless. As a result, the MCSs disappear. In addition, we note that the coupling between the parent s-wave superconductors and the Rashba layers [90–93] should be weak to avoid metallization effects [94–97].

5.E Edge State Wavefunctions in HTSC Phase

In this section we provide more details on the calculation of the wavefunction of the helical edge states in the HTSC phase. The Hamiltonian density in the absence of a Zeeman field ($\Delta_Z = 0$) [see Eqs. (5.2.1)-(5.2.3)] reads

$$\mathcal{H}_0(k_x, k_y) = \left[\eta_3 \frac{\hbar^2 k^2}{2m} + \tau_3\alpha(k_y\sigma_1 - k_x\eta_3\sigma_2) + \Gamma\tau_1\eta_3 + \Delta\tau_3\eta_2\sigma_2\right]/2, \tag{5.E.1}$$

where τ_i, η_i, σ_i are the Pauli matrices acting in layer, particle-hole, and spin space, respectively. Note that we set here $\phi = \pi$ for simplicity. This Hamiltonian density was also used to obtain the spectrum in Eq. (5.3.1) in the main text.

As discussed in the main text, we calculate the wavefunctions of the helical edge states that are exponentially localized at the $s = 0$ edge. These modes are localized in the y direction (located close to $y = 0$) and propagate in the x direction. In order to find the wavefunction, we assume the edge to be infinitely extended and focus on the states with $k_x = 0$. Due to particle-hole and time-reversal symmetry it is clear that these states are at zero energy and twofold degenerate (Kramers pair). For simplicity, we work in the strong SOI limit where we can linearize the Hamiltonian density $\mathcal{H}_0(0, k_y)$ around two Fermi points ($k_{Fi} = 0$, $k_{Fe} = 2k_{so}$) [98],

$$\mathcal{H}_0(0, k_y) = \left[\eta_3 \frac{\hbar^2 k_y^2}{2m} + \tau_3\sigma_1\alpha k_y + \Gamma\tau_1\eta_3 + \Delta\tau_3\eta_2\sigma_2\right]/2\,. \tag{5.E.2}$$

In what follows we denote the wavefunctions (field operators) by $\tilde{\Phi}_\sigma$ ($\tilde{\psi}_\sigma$) when $\sigma = \uparrow, \downarrow$ refers to the spin projection onto the x axis. The field operators can then be approximated as

$$\begin{aligned}
&\tilde{\psi}_{1\uparrow} = \tilde{L}_{1\uparrow}e^{-2ik_{so}y} + \tilde{R}_{1\uparrow},\ \tilde{\psi}_{1\downarrow} = \tilde{L}_{1\downarrow} + \tilde{R}_{1\downarrow}e^{2ik_{so}y} \\
&\tilde{\psi}_{\bar{1}\uparrow} = \tilde{L}_{\bar{1}\uparrow} + \tilde{R}_{\bar{1}\uparrow}e^{2ik_{so}},\ \tilde{\psi}_{\bar{1}\downarrow} = \tilde{L}_{\bar{1}\downarrow}e^{-2ik_{so}y} + \tilde{R}_{\bar{1}\downarrow},
\end{aligned} \tag{5.E.3}$$

where $\tilde{L}_{\tau\sigma}(y)$ [$\tilde{R}_{\tau\sigma}(y)$] are slowly varying fields on the scale of k_{so}^{-1}. The linearized Hamiltonian density is then given by

$$\tilde{\mathcal{H}}_{0,lin} = [\hbar v_F \hat{k}\rho_3 + \Gamma(\tau_1\eta_3\rho_1 - \tau_2\eta_3\sigma_3\rho_2)/2 + \Delta\tau_3\eta_2\sigma_2\rho_1]/2\,, \tag{5.E.4}$$

where $\hat{k} = -i\hbar\partial_y$ is the momentum operator and $v_F = \alpha/\hbar$ the Fermi velocity, and ρ_i act in left/right mover space. By imposing vanishing boundary conditions,

$\tilde{\Phi}_\pm(y=0)=0$, we find two independent zero-energy solutions only if $\Gamma>\Delta$. The corresponding wavefunctions are written in the basis,

$$\tilde{\Psi}=(\tilde{\psi}_{1\uparrow,k_x=0},\tilde{\psi}_{1\downarrow,k_x=0},\tilde{\psi}^\dagger_{1,\uparrow,k_x=0},\tilde{\psi}^\dagger_{1\downarrow,k_x=0},\tilde{\psi}_{\bar{1}\uparrow,k_x=0},\tilde{\psi}_{\bar{1}\downarrow,k_x=0},\tilde{\psi}^\dagger_{\bar{1}\uparrow,k_x=0},\tilde{\psi}^\dagger_{\bar{1}\downarrow,k_x=0}), \tag{5.E.5}$$

as

$$\begin{aligned}\tilde{\Phi}_+(y)&=\frac{1}{\sqrt{N}}\Big[f_1(y),g_1(y),f_1^*(y),g_1^*(y),f_{\bar{1}}(y),g_{\bar{1}}(y),f_{\bar{1}}^*(y),g_{\bar{1}}^*(y)\Big]^T,\\ \tilde{\Phi}_-(y)&=\frac{1}{\sqrt{N}}\Big[g_1^*(y),-f_1^*(y),g_1(y),-f_1(y),g_{\bar{1}}^*(y),-f_{\bar{1}}^*(y),g_{\bar{1}}(y),-f_{\bar{1}}(y)\Big]^T,\end{aligned} \tag{5.E.6}$$

with $f_1(y)=-ig_1^*(y)=e^{2ik_{so}y}e^{-y/\xi}-e^{-y/\xi_-}$ and $f_{\bar{1}}(y)=-ig_{\bar{1}}^*(y)=-i(e^{-2ik_{so}y}e^{-y/\xi}-e^{-y/\xi_-})$, where the localization lengths are defined as $\xi=\hbar v_F/\Delta$ and $\xi_-=\hbar v_F/(\Gamma-\Delta)$. These two solutions are Kramers partners and related by time-reversal symmetry described by the operator $\Theta=-i\sigma_2\mathcal{K}$ with $\Theta\tilde{\Phi}_\pm=\pm\tilde{\Phi}_\mp$. Moreover, both $\tilde{\Phi}_+(y)$ and $\tilde{\Phi}_-(y)$ are extended Majorana wavefunctions (not to be confused with the MCSs that are localized at the corners) that are eigenstates of the particle-hole operator $\mathcal{P}=\eta_1\mathcal{K}$, *i.e.*, $\mathcal{P}\tilde{\Phi}_\pm=\tilde{\Phi}_\pm$. As can be seen above, the spin-up and spin-down components of the Majorana wavefunctions in Eq. (5.E.6) are not independent but related by $g_\tau(y)=-if_\tau^*(y)$ [99, 100]. This is ensured by the symmetry operator $\mathcal{O}=\eta_2\sigma_1$, which commutes with the particle-hole symmetry operator $[\mathcal{P},\mathcal{O}]=0$, and thus, $\mathcal{O}\tilde{\Phi}_\pm=\tilde{\Phi}_\pm$. The operator $\mathcal{O}$ anti-commutes with the Hamiltonian density in Eq. (5.E.2), $\{\mathcal{H}_0,\mathcal{O}\}=0$. Moreover, also the functions $f_1(y)$ and $f_{\bar{1}}(y)$ are not independent from each other, but related by $f_1(y)=-if_{\bar{1}}^*(y)$. This is ensured by the symmetry operator $\mathcal{O}'=\tau_1\eta_2$, which commutes with the previous two symmetries, $[\mathcal{P},\mathcal{O}']=[\mathcal{O},\mathcal{O}']=0$, and thus $\mathcal{O}'\tilde{\Phi}_\pm=\pm\tilde{\Phi}_\pm$. It is useful to take advantage of these hidden symmetries when calculating the various matrix elements in deriving the effective low-energy Hamiltonian in the following.

First we note that the spin-operator $\tilde{\mathbf{S}}$ in Nambu space is parametrized by the following Pauli matrices $\tilde{\mathbf{S}}\sim(\eta_3\sigma_3,\sigma_2,\eta_3\sigma_1)$ (we recall that we take the x axis as the spin quantization axis). In addition, this operator anti-commutes with the particle-hole operator, $\{\tilde{\boldsymbol{S}},\mathcal{P}\}=0$. Then, the symmetry of the Majorana wavefunctions leads to

$$\langle\tilde{\Phi}_a|\tilde{\boldsymbol{S}}|\tilde{\Phi}_a\rangle=\langle\tilde{\Phi}_a|\mathcal{P}\tilde{\boldsymbol{S}}\mathcal{P}|\tilde{\Phi}_a\rangle=-\langle\tilde{\Phi}_a|\tilde{\boldsymbol{S}}|\tilde{\Phi}_a\rangle, \tag{5.E.7}$$

for $a\in\{+,-\}$, and therefore $\langle\tilde{\Phi}_a|\tilde{\boldsymbol{S}}|\tilde{\Phi}_a\rangle=0$. The expectation values of spin projections to any axis is zero for Majorana states. The time-reversal operator Θ and

the operator $\mathcal{O}$, which ensures the structure of the Majorana wavefunctions $\tilde{\Phi}_\pm$, fix the values of the off-diagonal terms,

$$\begin{aligned}\langle\tilde{\Phi}_+|\eta_3\sigma_3|\tilde{\Phi}_-\rangle &= \langle\tilde{\Phi}_+|\mathcal{P}\eta_3\sigma_3\Theta|\tilde{\Phi}_+\rangle = \langle\tilde{\Phi}_+|\eta_1\mathcal{K}\eta_3\sigma_3(-i\sigma_2)\mathcal{K}|\tilde{\Phi}_+\rangle \\ &= \langle\tilde{\Phi}_+|\eta_1\eta_3\sigma_3(-i\sigma_2)|\tilde{\Phi}_+\rangle = i\,\langle\tilde{\Phi}_+|\eta_2\sigma_1|\tilde{\Phi}_+\rangle = i\,\langle\tilde{\Phi}_+|\mathcal{O}|\tilde{\Phi}_+\rangle \\ &= i\,\langle\tilde{\Phi}_+|\tilde{\Phi}_+\rangle = i,\end{aligned}$$

$$\langle\tilde{\Phi}_+|\sigma_2|\tilde{\Phi}_-\rangle = \langle\tilde{\Phi}_+|\mathcal{O}\sigma_2\mathcal{O}|\tilde{\Phi}_-\rangle = -\langle\tilde{\Phi}_+|\sigma_2|\tilde{\Phi}_-\rangle = 0 \tag{5.E.8}$$

$$\langle\tilde{\Phi}_+|\eta_3\sigma_1|\tilde{\Phi}_-\rangle = \langle\tilde{\Phi}_+|\mathcal{O}\eta_3\sigma_1\mathcal{O}|\tilde{\Phi}_-\rangle = -\langle\tilde{\Phi}_+|\eta_3\sigma_1|\tilde{\Phi}_-\rangle = 0, \tag{5.E.9}$$

$$\tag{5.E.10}$$

where we used the fact that $\{\mathcal{O},\eta_2\} = \{\mathcal{O},\eta_3\sigma_1\} = 0$. In addition, one finds

$$\begin{aligned}&\langle\tilde{\Phi}_+|(1-\tau_3)\eta_1\sigma_2|\tilde{\Phi}_+\rangle = \langle\tilde{\Phi}_+|\eta_1\sigma_2|\tilde{\Phi}_+\rangle - \langle\tilde{\Phi}_+|\tau_3\eta_1\sigma_2|\tilde{\Phi}_+\rangle = 0, \text{ since} \\ &\langle\tilde{\Phi}_+|\eta_1\sigma_2|\tilde{\Phi}_+\rangle = \langle\tilde{\Phi}_+|\mathcal{O}\eta_1\sigma_2|\tilde{\Phi}_+\rangle = \langle\tilde{\Phi}_+|\eta_3\sigma_3|\tilde{\Phi}_+\rangle = 0, \text{ and} \\ &\langle\tilde{\Phi}_+|\tau_3\eta_1\sigma_2|\tilde{\Phi}_+\rangle = \langle\tilde{\Phi}_+|\mathcal{P}\tau_3\eta_1\sigma_2|\tilde{\Phi}_+\rangle = -\langle\tilde{\Phi}_+|\tau_3\eta_1\sigma_2|\tilde{\Phi}_+\rangle = 0,\end{aligned} \tag{5.E.11}$$

where we used that $\{\mathcal{P},\tau_3\eta_1\sigma_2\} = 0$. By analogy, one also finds

$$\langle\tilde{\Phi}_-|(1-\tau_3)\eta_1\sigma_2|\tilde{\Phi}_-\rangle = 0. \tag{5.E.12}$$

However, the off-diagonal term is given by

$$\begin{aligned}&\langle\tilde{\Phi}_+|(1-\tau_3)\eta_1\sigma_2|\tilde{\Phi}_-\rangle = i, \text{ since} \\ &\langle\tilde{\Phi}_+|\eta_1\sigma_2|\tilde{\Phi}_-\rangle = \langle\tilde{\Phi}_+|\eta_3\sigma_3|\tilde{\Phi}_-\rangle = i \text{ and} \\ &\langle\tilde{\Phi}_+|\tau_3\eta_1\sigma_2|\tilde{\Phi}_-\rangle = \langle\tilde{\Phi}_+|\mathcal{P}\tau_3\eta_1\sigma_2|\tilde{\Phi}_-\rangle = -\langle\tilde{\Phi}_+|\tau_3\eta_1\sigma_2|\tilde{\Phi}_-\rangle = 0,\end{aligned} \tag{5.E.13}$$

where in the second line we used Eq. (5.E.8) and Eq. (5.E.11). The last matrix element we are considering here is given by $\langle\tilde{\Phi}_+|\tau_3\eta_3\sigma_2|\tilde{\Phi}_-\rangle$. Using time-reversal and particle-hole symmetry operators, one can rewrite it as

$$\langle\tilde{\Phi}_+|\tau_3\eta_3\sigma_2|\tilde{\Phi}_-\rangle = \langle\tilde{\Phi}_+|\tau_3\eta_3\sigma_2(-i\sigma_2\mathcal{K})\eta_1\mathcal{K}|\tilde{\Phi}_+\rangle = -i\,\langle\tilde{\Phi}_+|\tau_3\eta_3\eta_1|\tilde{\Phi}_+\rangle = -\langle\tilde{\Phi}_+|\tau_3\eta_2|\tilde{\Phi}_+\rangle\,. \tag{5.E.14}$$

This last expression can be shown to be zero by invoking the symmetry operator $\mathcal{O}'$,

$$\langle\tilde{\Phi}_+|\tau_3\eta_2|\tilde{\Phi}_+\rangle = \langle\tilde{\Phi}_+|\mathcal{O}'\tau_3\eta_2|\tilde{\Phi}_+\rangle = \langle\tilde{\Phi}_+|\tau_1\eta_2\tau_3\eta_2|\tilde{\Phi}_+\rangle = -\langle\tilde{\Phi}_+|\tau_3\eta_2|\tilde{\Phi}_+\rangle = 0. \tag{5.E.15}$$

Importantly, the values of all these expectation values do not depend on the explicit form of $f_\tau(y)$.

The wavefunctions in the original spin basis, where the z direction is the spin quantization axis, are given by $\Phi^{(0)}_\pm(y) = e^{-i\pi\sigma_2/4}\tilde{\Phi}_\pm(y)$, which will be used in further calculations below. In order to avoid confusion we stress that the spin operator then takes the more familiar form $\boldsymbol{S} = \hbar(\eta_3\sigma_1,\sigma_2,\eta_3\sigma_3)/2$.

5.F Derivation of Effective Low-Energy Hamiltonian

Using the explicit form of the wavefunctions obtained in the previous section, we derive the low-energy effective Hamiltonian on all four edges. As outlined in the main text, the Hamiltonian of the Rashba layers [see Eq. (5.2.1)] is invariant under rotations $U_\varphi = e^{i\varphi\eta_3 J_z/\hbar}$, generated by the total angular momentum operator $J_z = L_z + S_z$. This allows us, knowing the wavefunctions at $s = 0$ edge, to find the wavefunctions at the other three edges by applying U_φ to $\Phi^{(0)}_\pm(y)$: $\Phi^{(s)}_\pm(y) = U_{\varphi_s}\Phi^{(0)}_\pm(y)$ with $\varphi_s \in \{0, \pi/2, \pi, 3\pi/2\}$.

We first derive the low-energy effective Hamiltonian for the helical edge states on the $s = 0$ edge from the wavefunctions obtained in the previous section. To achieve this, we add various perturbation to $\mathcal{H}_0(0, k_y)$ defined in Eq. (5.E.2). We restrict ourselves to first-order perturbation theory applied in the low-energy subspace spanned by $\Phi^{(0)}_\pm$, in which we focus only on linear terms in Δ_Z, Δ, and k_x

Kinetic part. The dispersion of the helical edge states close to zero-energy is linear, see Fig. 5.3 of the main text. This can be also shown explicitly by treating the linear term in k_x in $\mathcal{H}_0(k_x, k_y)$ [see Eq. (5.E.1)], $\mathcal{H}_{k_x} = -\alpha\tau_3\eta_3\sigma_2 k_x/2$ as a perturbation. For this term, the off-diagonal elements vanish by symmetry as was shown in Eq. (5.E.14)-(5.E.15). However, for the diagonal elements these arguments do not apply: $\langle\Phi^{(0)}_\pm|\mathcal{H}_{k_x}|\Phi^{(0)}_\pm\rangle$ depends on the explicit form of the function $f_1(y)$. As a result, we obtain the effective low-energy Hamiltonian for helical edge states to be written as

$$\mathcal{H}^{(0)}_{kin} = \hbar v k_x \beta_3, \tag{5.F.1}$$

where the Pauli matrix β_i acts in the low-energy subspace and the effective velocity v of the linearly dispersing edge states is given by

$$v = v_F \frac{\Delta}{\Gamma} < v_F. \tag{5.F.2}$$

We note that the Fermi velocity of the edge modes is the same at all four edges due to the rotation invariance of the system without applied magnetic fields.

Superconducting gap at edge states for $\phi \neq \pi$. In the main text, we also discussed the case where the phase difference between the two layers is not exactly $\phi = \pi$, but slightly deviating from it, *i.e.*, $\phi = \pi + \delta\phi$, where $\delta\phi \ll 1$ can be positive or negative. This leads to an extra factor in the superconducting pairing term in the $\tau = \bar{1}$ layer: $\Delta_{\bar{1}} = \Delta e^{i\phi} = \Delta e^{i(\pi+\delta\phi)} \approx -\Delta(1 + i\delta\phi)$. The deviations from the π-junction is given by $\mathcal{H}_{\delta\phi} = -\delta\phi\Delta(1-\tau_3)\eta_1\sigma_2/4$. In Eqs. (5.E.11) and (5.E.13), we showed that, due to the system symmetry, only the off-diagonal matrix elements

$\langle\Phi_{\pm}^{(0)}|\mathcal{H}_{\delta\phi}|\Phi_{\mp}^{(0)}\rangle$ are non-zero. This leads to

$$\mathcal{H}_{sc}^{(0)} = -\Delta\delta\phi\beta_2/2. \tag{5.F.3}$$

Again, due to the rotation invariance of the superconducting part of the Hamiltonian, this term opens a gap of the same size at all edges.

Zeeman term. For a weak Zeeman field $\Delta_Z \ll \Gamma - \Delta$, the corresponding term opening the gap in the edge state spectrum is given by $\mathcal{H}_Z = \Delta_Z[\cos(\theta)\eta_3\sigma_1 + \sin(\theta)\sigma_2]/2$. Using Eqs. (5.E.7) and (5.E.8), one notices that in the low-energy subspace only the term proportional to $\eta_3\sigma_1$ is important, and only its off-diagonal matrix elements are non-zero. This leads us to the effective Zeeman term acting in the low-energy subspace,

$$\mathcal{H}_Z^{(0)} = -\Delta_Z\cos(\theta)\beta_2. \tag{5.F.4}$$

The form of the effective Zeeman term in the Hamiltonian for the remaining edges can be simply obtained by calculating the matrix elements $\langle\Phi_a^{(s)}|\mathcal{H}_Z|\Phi_b^{(s)}\rangle$, where we make use of the symmetry operator U_{φ_s},

$$\left\langle\Phi_a^{(s)}|\mathcal{H}_Z|\Phi_b^{(s)}\right\rangle = \left\langle\Phi_a^{(0)}|U_{\varphi_s}^\dagger\mathcal{H}_Z U_{\varphi_s}|\Phi_b^{(0)}\right\rangle = -\Delta_Z\cos(\theta-\varphi_s)\beta_2, \tag{5.F.5}$$

$$U_{\varphi_s}^\dagger\mathcal{H}_Z U_{\varphi_s} = \Delta_Z[\cos(\theta-\varphi_s)\ \eta_3\sigma_1 + \sin(\theta-\varphi_s)\sigma_2]/2. \tag{5.F.6}$$

Thus, the gap opened by the Zeeman field is different at different edges and is given by the size $\Delta_Z\cos(\theta-\varphi_s)$. Collecting all terms together, we arrive at Eq. (5.4.1) of the main text:

$$\mathcal{H}_{eff}^{(s)} = \hbar v k^{(s)}\beta_3 - \Delta_s\beta_2, \tag{5.F.7}$$

$$\Delta_s = \Delta\delta\phi/2 + \Delta_Z\cos(\theta-\varphi_s). \tag{5.F.8}$$

By examining the sign of the gap Δ_s, one can identify potential domain walls and determine the location of zero-energy MCSs.

Concretely, in the effective Hamiltonian describing helical edge states [see Eq. (5.4.1)], the gap between the clockwise-moving mode $|\Phi_-^{(s)}\rangle$ and anticlockwise-moving mode $|\Phi_+^{(s)}\rangle$ is opened at $k^{(s)} = 0$. In this case, the Hamiltonian simplifies to

$$\mathcal{H}_{eff}^{(s)} = -\Delta_s\beta_2. \tag{5.F.9}$$

The eigenvalues are given by $E_\pm = \pm\Delta_s$ and the corresponding eigenstates by $|\pm\rangle = (|\Phi_-^{(s)}\rangle \pm i\,|\Phi_+^{(s)}\rangle)/\sqrt{2}$. If the gap is positive, $\Delta_s > 0$, then $E_+ > E_-$, and, thus, the eigenstate $|-\rangle$ is the groundstate. If the gap is negative, $\Delta_s < 0$, then $E_- > E_+$, and the eigenstate $|+\rangle$ is the groundstate. This change from $|-\rangle$ to $|+\rangle$ being the groundstate can be considered as the analog of a band inversion in topological insulators.

Bibliography

[1] A. Y. Kitaev, Phys.-Usp. **44**, 131 (2001).

[2] R. M. Lutchyn, J. D. Sau, and S. D. Sarma, Phys. Rev. Lett. **105**, 177002 (2010).

[3] Y. Oreg, R. Refael, and F. von Oppen, Phys. Rev. Lett. **105**, 177002 (2010).

[4] J. Alicea, Phys. Rev. B **81**, 125318 (2010).

[5] C. L. Kane and E. J. Mele, Phys. Rev. Lett. **95**, 226801 (2005).

[6] C. L. Kane and E. J. Mele, Phys. Rev. Lett. **95**, 146802 (2005).

[7] C. Wu, B. A. Bernevig, and S. Zhang, Phys. Rev. Lett. **96**, 106401 (2006).

[8] B. A. Bernevig, T. L. Hughes, and S. Zhang, Science **314**, 5806 (2006).

[9] L. Fu, C. L. Kane, and E. J. Mele, Phys. Rev. Lett. **98**, 106803 (2007).

[10] J. E. Moore and L. Balents, Phys. Rev. B **75**, 121306(R) (2007).

[11] M. König, S. Wiedmann, C. Brüne, A. Roth, H. Buhmann, L. W. Molenkamp, X. Qi, and S. Zhang, Science **318**, 5851 (2007).

[12] D. Hsieh, D. Qian, L. Wray, Y. Xia, Y. S. Hor, R. J. Cava, and M. Z. Hasan, Nature **452**, 970 (2008).

[13] D. Hsieh, Y. Xia, L. Wray, D. Qian, A. Pal, J. H. Dil, J. Osterwalder, F. Meier, G. Bihlmayer, C. L. Kane, Y. S. Hor, R. J. Cava, and M. Z. Hasan, Science **323**, 919 (2009).

[14] M. Z. Hasan and C. L. Kane, Rev. Mod. Phys. **82**, 3045 (2010).

[15] X.-L. Qi and S.-C. Zhang, Rev. Mod. Phys. **83**, 1057 (2011).

[16] Y. Ando and L. Fu, Annu. Rev. Condens. Matter Phys. **6**, 361 (2015).

[17] A. Stern, Annu. Rev. Condens. Matter Phys. **7**, 349 (2016).

[18] M. Sato and Y. Ando, Rep. Prog. Phys. **80**, 076501 (2017).

[19] A. C. Potter and P. A. Lee, Phys. Rev. B **83**, 094525 (2011).

[20] M. Z. Hasan and J. E. Moore, Annu. Rev. Condens. Matter **2**, 55 (2011).

[21] D. Chevallier, D. Sticlet, P. Simon, and C. Bena, Phys. Rev. B **85**, 235307 (2012).

[22] J. Klinovaja, S. Gangadharaiah, and D. Loss, Phys. Rev. Lett. **108**, 196804 (2012).

[23] D. Sticlet, C. Bena, and P. Simon, Phys. Rev. Lett. **108**, 096802 (2012).

[24] J. Klinovaja, P. Stano, and D. Loss, Phys. Rev. Lett. **109**, 236801 (2012).

[25] B. I. Halperin, Y. Oreg, A. Stern, G. Refael, J. Alicea, and F. von Oppen, Phys. Rev. B **85**, 144501 (2012).

[26] S. Nadj-Perge, I. K. Drozdov, B. A. Bernevig, and A. Yazdani, Phys. Rev. B **88**, 020407 (R) (2013).

[27] J. Klinovaja, P. Stano, A. Yazdani, and D. Loss, Phys. Rev. Lett. **111**, 186805 (2013).

[28] B. Braunecker and P. Simon, Phys. Rev. Lett. **111**, 147202 (2013).
[29] M. Vazifeh and M. Franz, Phys. Rev. Lett. **111**, 206802 (2013).
[30] L. Weithofer, P. Recher, and T. L. Schmidt, Phys. Rev. B **90**, 205416 (2014).
[31] J. Manousakis, A. Altland, D. Bagrets, R. Egger, and Y. Ando, Phys. Rev. B **95**, 165424 (2017).
[32] A. Das, Y. Ronen, Y. Most, Y. Oreg, M. Heiblum, and H, Shrikman, Nature **8**, 887–895 (2012).
[33] V. Mourik, K. Zuo, S. M. Frolov, S. R. Plissard, E. P. A. M. Bakkers, and L. P. Kouwenhoven, Science **336**, 6084 (2012).
[34] M. T. Deng, C. L. Yu, G. Y. Huang, M. Larsson, P. Caroff, and H. Q. Xu, Nano Lett. **12**, 6414 (2012).
[35] A. D. K. Finck, D. J. Van Harlingen, P. K. Mohseni, K. Jung, and X. Li, Phys. Rev. Lett. **110**, 126406 (2013).
[36] H. O. H. Churchill, V. Fatemi, K. Grove-Rasmussen, M. T. Deng, P. Caroff, H. Q. Xu, and C. M. Marcus, Phys. Rev. B **87**, 241401(R) (2013).
[37] S. M. Albrecht, A. P. Higginbotham, M. Madsen, F. Kuemmeth, T. S. Jespersen, J. Nygard, P. Krogstrup, and C. M. Marcus, Nature **531**, 206 (2016).
[38] H. Zhan *et al.*, Nature **556**, 74 (2018).
[39] S. Nadj-Perge, I. K. Drozdov, J. Li, H. Chen, S. Jeon, J. Seo, A. H. MacDonald, B. A. Bernevig, and A. Yazdani, Science **346**, 602 (2014).
[40] M. Ruby, F. Pientka, Y. Peng, F. von Oppen, B. W. Heinrich, and K. J. Franke, Phys. Rev. Lett. **115**, 197204 (2015).
[41] R. Pawlak, M. Kisiel, J. Klinovaja, T. Meier, S. Kawai, T. Glatzel, D. Loss, and E. Meyer, Npj Quantum Inform. **2**, 16035 (2016).
[42] W. A. Benalcazar, J. C. Teo, and T. L. Hughes, Phys. Rev. B **89**, 224503 (2014).
[43] W. A. Benalcazar, B. A. Bernevig, and T. L. Hughes, Science **357**, 61 (2017).
[44] W. A. Benalcazar, B. A. Bernevig, and T. L. Hughes, Phys. Rev. B **96**, 245115 (2017).
[45] Z. Song, Z. Fang, and C. Fang, Phys. Rev. Lett. **119**, 246402 (2017).
[46] Y. Peng, Y. Bao, and F. von Oppen, Phys. Rev. B **95**, 235143 (2017).
[47] S. Imhof, C. Berger, F. Bayer, H. Brehm, L. Molenkamp, T. Kiessling, F. Schindler, C. H. Lee, M. Greiter, T. Neupert, and R. Thomale, arix:1708.03647.
[48] M. Geier, L. Trifunovic, M. Hoskam, and P. W. Brouwer, Phys. Rev. B **97**, 205135 (2018).
[49] F. Schindler, A. M. Cook, M. G. Verginory, Z. Wang, S. S. P. Parking, B. A. Bernevig, and T. Neupert, Science Adv. **4**, 6 (2018).
[50] C.-H. Hsu, P. Stano, J. Klinovaja, and D. Loss, Phys. Rev. Lett. 121, 196801 (2018).
[51] M. Ezawa, Phys. Rev. B 97, 155305 (2018).
[52] M. Ezawa, arxiv:1807.10932.
[53] M. Ezawa, Phys. Rev. Lett. **121**, 116801 (2018).
[54] X. Zhu, Phys. Rev. B **97**, 205134 (2018).
[55] Q. Wang, C.-C. Liu, Y.-M. Lu, and F. Zhang, Phys. Rev. Lett. **121**, 186801 (2018).
[56] Z. Yan, F. Song, and Z. Wang, Phys. Rev. Lett. **121**, 096803 (2018).
[57] T. Liu, J. J. He, and F. Nori, Phys. Rev. B **18**, 245413 (2018).
[58] X. Zhang, H.-X. Wang, Z.-K. Lin, Z. Tian, B. Xie, M.-H. Lu, Y.-F. Chen, and J.-H. Jian, arxiv:1806.10028.
[59] Q. Wang, D. Wand, and Q.-H. Wang, arxiv:1808.01085.
[60] Y. Wang, M. Lin, and T. L. Hughes, Phys. Rev. B **98**, 165144 (2018).

[61] H. Ren, F. Pientka, S. Hart, A. Pierce, M. Kosowsky, L. Lunczer, R. Schlereth, B. Scharf, E. M. Hankiewicz, L. W. Molenkamp, B. I. Halperin, and A. Yacoby, arXiv:1809.03076.

[62] A. Fornieri, A. M. Whiticar, F. Setiawan, E. P. Martin, A. C. C. Drachmann, A. Keselman, S. Gronin, C. Thomas, T. Wang, R. Kallaher, G. C. Gardner, E. Berg, M.J. Manfra, A. Stern, C. M. Marcus, and F. Nichele, arXiv:1809.03037.

[63] C. Schrade, A. A. Zyuzin, J. Klinovaja, and D. Loss, Phys. Rev. Lett. **115**, 237001 (2015).

[64] A. I. Buzdin, L. N. Bulaevskii, and S.V. Panyukov, Pis'ma Zh. Eksp. Teor. Fiz. **35**, 147 (1982) [JETP Lett. **35**, 178 (1982)].

[65] V.V. Ryazanov, V.A. Oboznov, A. Yu. Rusanov, A.V. Veretennikov, A.A. Golubov, and J. Aarts, Phys. Rev. Lett. **86**, 2427 (2001).

[66] B. I. Spivak and S. A. Kivelson, Phys. Rev. B **43**, 3740 (1991).

[67] J. A. van Dam, Y.V. Nazarov, E. P.A.M. Bakkers, and L. P. Kouwenhoven, Nature (London) **442**, 667 (2006).

[68] We note that our result stays valid also if the two SOI vectors are slightly misaligned. The topological transition is determined by the gap closing at $k = 0$, where the SOI terms do not play a role, under the condition that the bulk spectrum stays gapped at all other values of k.

[69] A. Keselman, L. Fu, and E. Berg, Phys. Rev. Lett. **111**, 116402 (2013).

[70] F. Pientka, A. Keselman, E. Berg, A. Yacoby, A. Stern, and B. I. Halperin, Phys. Rev. X **7**, 021032 (2017).

[71] S. Ryu, A. P. Schnyder, A. Furusaki, and A. W. W. Ludwig, New J. Phys. **12**, 065010 (2010).

[72] Y. Tanaka, Y. Mizuno, T. Yokoyama, K. Yada, and M. Sato, Phys. Rev. Lett. **105**, 097002 (2010).

[73] M. Sato and S. Fujimoto, Phys. Rev. Lett. **105**, 217001 (2010).

[74] M. Sato, Y. Tanaka, K. Yada, and T. Yokoyama, Phys. Rev. B **83**, 224511 (2011).

[75] A. P. Schnyder and S. Ryu, Phys. Rev. B **84**, 060504(R) (2011).

[76] T. Meng and L. Balents, Phys. Rev. B **86**, 054504 (2012).

[77] C. L. M. Wong, J. Liu, K. T. Law, and P. A. Lee, Phys. Rev. B **88**, 060504(R) (2013).

[78] A. Daido and Y. Yanase, Phys. Rev. B **95**, 134507 (2017).

[79] S. Deng, G. Ortiz, A. Poudel, and L. Viola, Phys. Rev. B **89**, 140507(R) (2014).

[80] A. P. Schnyder and P. M. R. Brydon, J. Phys.: Condens. Matter **27**, 243201 (2015).

[81] L. Hao and C. S. Ting, Phys. Rev. B **95**, 064513 (2017).

[82] Y. Volpez, D. Loss, and J. Klinovaja, Phys. Rev. B **97**, 195421 (2018).

[83] J. Klinovaja, A. Yacoby, and D. Loss, Phys. Rev. B **90**, 155447 (2014).

[84] J. Klinovaja and D. Loss, Phys. Rev. B **92**, 121410(R) (2015).

[85] R. Jackiw and C. Rebbi, Phys. Rev. D 13, 3398 (1976).

[86] R. Jackiw and J. Schrieffer, Nucl. Phys. B 190, 253 (1981).

[87] F. Parhizgar and A. Black-Schaffer, Sci. Rep. **7**, 9817 (2017).

[88] D. Rainis, L. Trifunovic, J. Klinovaja, and D. Loss, Phys. Rev. B **87**, 024515 (2013).

[89] J. Klinovaja and D. Loss, Eur. Phys. J. B **88**, 62 (2015).

[90] W. Chang, S. M. Albrecht, T. S. Jespersen, F. Kuemmeth, P. Krogstrup, J. Nygård, and C. M. Marcus, Nat. Nano. **10**, 232 (2015).

[91] S. Gazibegovic, D. Car, H. Zhang, S. C. Balk, J. A. Logan, M. W. A. de Moor, M. C. Cassidy, R. Schmits, D. Xu, G. Wang, P. Krogstrup, R. L. M. Op het Veld, K. Zuo, Y. Vos, J. Shen, D. Bouman, B. Shojaei, D. Pen- nachio, J. S. Lee, P. J. van Veldhoven, S. Koelling, M.

A. Verheijen, L. P. Kouwenhoven, C. J. Palmstrøm, and E. P. A. M. Bakkers, Nature **548**, 434 (2017).

[92] M. Kjaergaard, F. Nichele, H. J. Suominen, M. P. Nowak, M. Wimmer, A. R. Akhmerov, J. A. Folk, K. Flensberg, J. Shabani, C. J. Palmstrøm, and C. M. Marcus, Nat. Commun. **7**, 12841 (2016).

[93] J. Shabani, M. Kjaergaard, H. J. Suominen, Y. Kim, F. Nichele, K. Pakrouski, T. Stankevic, R. M. Lutchyn, P. Krogstrup, R. Feidenhans'l, S. Kraemer, C. Nayak, M. Troyer, C. M. Marcus, and C. J. Palmstrøm, Phys. Rev. B **93**, 155402 (2016).

[94] C. Reeg, D. Loss, and J. Klinovaja, Phys. Rev. B **96**, 125426 (2017).

[95] C. Reeg, D. Loss, and J. Klinovaja, Phys. Rev. B **97**, 165425 (2018).

[96] C. Reeg, D. Loss, and J. Klinovaja, Beilstein J. Nanotechnol. **9**, 1263 (2018).

[97] A. E. Antipov, A. Bargerbos, G. W. Winkler, B. Bauer, E. Rossi, and R. M. Lutchyn, Phys. Rev. X **8**, 031041 (2018).

[98] J. Klinovaja and D. Loss, Phys. Rev. B **86**, 085408 (2012).

[99] J. Klinovaja and D. Loss, Phys. Rev. B **90**, 045118 (2014).

[100] J. Klinovaja, A. Yacoby, and D. Loss, Phys. Rev. B **90**, 155447 (2014).

Chapter 6

Time-Reversal Invariant Topological Superconductivity in Planar Josephson Bijunction

Adapted from:
Yanick Volpez, Daniel Loss, and Jelena Klinovaja
"Time-Reversal Invariant Topological Superconductivity in Planar Josephson Bijunction",
Phys. Rev. Research **2**, 023415 (2020).

We consider a Josephson bijunction consisting of a thin SIS π-Josephson junction sandwiched between two-dimensional semiconducting layers with strong Rashba spin-orbit interaction. Each of these layers forms an SNS junction due to proximity-induced superconductivity. The SIS junction is assumed to be thin enough such that the two Rashba layers are tunnel-coupled. We show that, by tuning external gates, this system can be controllably brought into a time-reversal invariant topological superconducting phase with a Kramers pair of Majorana bound states being localized at the end of the normal region for a large parameter phase space. In particular, in the strong spin-orbit interaction limit, the topological phase can be accessed already in the regime of small tunneling amplitudes.

6.1 Introduction

The prediction of Majorana bound states (MBSs) in p-wave superconductors [1] and the proposed implementation in semiconductor-superconductor heterostructures [2–4] has sparked wide interest in exploring new platforms hosting topological superconductivity. Prominent experimental realizations involve nanowires proximitized by an s-wave superconductor [5–10], or chains of magnetic adatoms on s-wave superconductors [11–19]. More recently, MBSs in Josephson junctions [20] gained considerable interest [21–31], since this setup offers additional control knobs for experiments, in particular, the superconducting phase difference. In this case, the topological phase can be reached for a wide parameter range and the scalability to topological networks seems promising [20].

In contrast, time-reversal invariant (TRI) topological superconductors hosting Kramers pairs of MBSs [32–55] are still lacking experimental evidence. Such schemes are attractive since they avoid magnetic fields and their detrimental effect on superconductivity. Many such proposals rely on unconventional superconductors or can only be achieved with strong electron-electron interactions [56, 57]. A major drawback of them is that they do not allow for an easy *in-situ* control over the topological phase.

It is the goal of the present work to close this gap. For this we propose a Josephson bijunction which can be brought into the TRI topological superconducting phase via the control of experimentally accessible parameters, thereby hosting multiple Kramers pairs of MBSs, see Fig. 6.1. The setup consists of a superconductor-insulator-superconductor (SIS) Josephson junction sandwiched between semiconducting layers with Rashba spin-orbit interaction (SOI) [see Fig. 6.1(a)]. The superconductors are assumed to be s-wave and to have a phase difference ϕ controlled by applying a magnetic flux or generated by introducing an additional layer of randomly oriented magnetic impurities [58–62]. Due to the proximity effect this leads to the formation of two tunnel-coupled superconductor-normal-superconductor (SNS) Josephson junctions of width W and phase difference ϕ [see Fig. 6.1(a)]. This setup leads to an intricate interplay between the formation of Andreev bound state bands (ABSBs) in both SNS junctions on one hand and the hybridization of the two Rashba layers on the other hand, with striking consequences. In particular, we find a periodic closing and reopening of the topological gap in the spectrum of the ABSBs as a function of $k_{so}W$, where k_{so} is the SOI momentum which can be tuned electrically via gates [63–65]. Interestingly, in the strong SOI limit, the TRI topological phase can be reached for a relatively small tunneling amplitude.

We believe that with the recent advances in the fabrication and study of bilayer systems [66–69] and van der Waals heterostructures [70–74], the setup proposed here lies within experimental reach and could be a promising route in realizing Kramers pairs of MBSs without the need of magnetic fields.

6.2 Model

The Josephson bijunction consists of two semiconducting layers labeled by $\tau = \pm 1$. Due to the structural asymmetry the Rashba SOI vectors $\boldsymbol{\alpha}_\tau$ are naturally antiparallel and aligned along the z axis, which is normal to the layers. The layers are modeled by

$$H_\tau = \sum_{\sigma,\sigma'} \int d\boldsymbol{r}\ \psi^\dagger_{\tau\sigma}(\boldsymbol{r}) \mathcal{H}_{\tau\sigma\sigma'}(\boldsymbol{r}) \psi_{\tau\sigma'}(\boldsymbol{r}), \tag{6.2.1}$$

where $\mathcal{H}_{\tau\sigma\sigma'}(\boldsymbol{r}) = [-\hbar^2\nabla^2/(2m) - \mu_\tau + \boldsymbol{\alpha}_\tau \cdot \boldsymbol{\sigma} \times \hat{\mathbf{k}}]_{\sigma\sigma'}$, m is the effective mass, μ_τ the chemical potential, $\hat{\mathbf{k}} = -i\hbar(\partial_x, \partial_y)$ the in-plane momentum operator, and σ_i are the Pauli matrices acting in spin space. The operator $\psi^\dagger_{\tau\sigma}(\boldsymbol{r})$ creates an electron with spin projection σ along the z axis in the τ-layer at the position $\boldsymbol{r} = (x, y)$. The SOI energy $E_{\tau,so} = \hbar^2 k^2_{so,\tau}/2m$, with the SOI momentum $k_{so,\tau} = m\alpha_\tau/\hbar^2$, is the energy difference between the bottom of the Rashba bands and the degeneracy point at $k = 0$, from which μ_τ is measured.

The regions that are in contact with the bulk superconductors become superconducting as well [20, 25, 26, 28] and the proximitized Rashba layers themselves form an SNS junction with a normal region of width W [75]. The superconducting

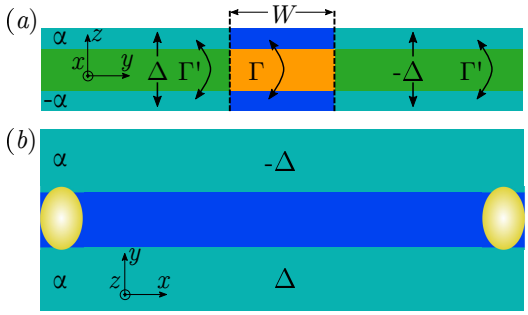

Figure 6.1: (a) Josephson bijunction setup consisting of a top (blue and mint) and bottom (blue and mint) Rashba layer with opposite SOI in contact with an SIS junction (green-orange-green). The superconductors (green) have a phase difference π and are separated by an insulator (orange) of width W. The proximity to the SIS junction creates two SNS junctions of width W in the Rashba layers. (b) Top view of the setup. In the topological phase a Kramers pair of MBSs (yellow dots) emerges at each end of the junction.

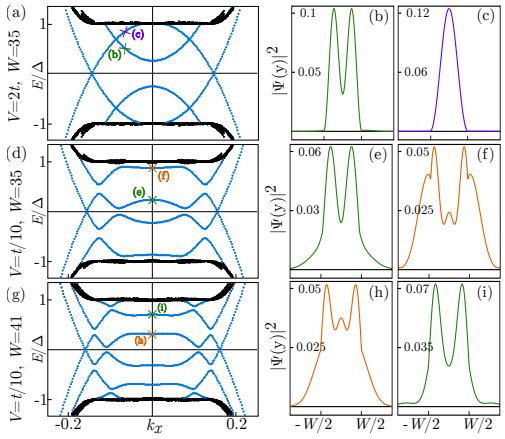

Figure 6.2: Spectrum as function of momentum k_x for (a) $V = 2t$ and $W = 35$, (d) $V = t/10$ and $W = 35$, and (g) $V = t/10$ and $W = 41$. (a) For a high potential barrier V, the transverse subbands [$n = 1$ (purple cross) and $n = 2$ (green cross)] are decoupled from the superconducting regions and lie within the superconducting gap (black). (b)-(c) The corresponding probability densities $|\psi(y)|^2$ at $k_x = -0.08$ of the first two transverse subbands. (d) Upon lowering V, the interfaces become transparent leading to ABSBs. The electron and hole bands are mixed now and as a consequence each ABSB has contributions from different transverse subbands with the dominant orbital content depending on k_x. The lowest ABSB also has a very small gap around $|k_x| \approx 0.2$, which is further discussed in the text. (e)-(f) At $k_x = 0$, the lowest (second) ABSB comes from the $n = 2$ ($n = 3$) subband of the normal region. (g) Between $W = 35$ and $W = 41$, the inverted case emerges where the lowest (second) ABSB comes from the $n = 3$ ($n = 2$) subband [(h) and (i)]. This is the origin of the topological phase transition of higher subbands (see text below and Appendix 6.B). Numerical parameters are $a = 1$, $N_y = 500$, $N_W = W - 1$, $\alpha_1/t = -\alpha_{\bar{1}}/t = 0.07$, $\Delta/t = 0.012$, $\Gamma = 1.5\Delta$, and $\Gamma' = 0$.

regions are described by [76]

$$H_\Delta = \sum_{\tau,\sigma,\sigma'} \int d\boldsymbol{r} \left[\Delta_\tau(y)\psi^\dagger_{\tau\sigma}(\boldsymbol{r})[i\sigma_2]_{\sigma\sigma'}\psi^\dagger_{\tau\sigma'}(\boldsymbol{r}) + \text{H.c.}\right], \tag{6.2.2}$$

where $\Delta_\tau(y) = \Delta e^{i\text{sgn}(y)\phi/2}\theta(|y| - W/2)/2$, $\Delta > 0$ is the strength of the induced superconducting pairing and ϕ is the phase difference between the superconducting regions inherited from the parent superconductors. We also allow for electron tunneling between the two layers,

$$H_\Gamma = \sum_\sigma \int d\boldsymbol{r} \left[\bar{\Gamma}(y)\psi^\dagger_{1\sigma}(\boldsymbol{r})\psi_{\bar{1}\sigma}(\boldsymbol{r}) + \text{H.c.}\right], \tag{6.2.3}$$

where we assume the tunneling amplitude to be uniform in the x direction such that $\bar{\Gamma}(y) = \Gamma\theta(W/2 - |y|) + \Gamma'\theta(|y| - W/2)$, and without loss of generality $\Gamma > 0$

($\Gamma' \geq 0$) for the coupling between the two layers [83]. The total Hamiltonian modeling the setup is then given by $H = H_1 + H_{\bar{1}} + H_\Delta + H_\Gamma$.

First, we study the system numerically for two geometries (see Appendix 6.A for details): (*i*) *semi-infinite geometry* - the system is translationally invariant along the direction of the junction, *i.e.*, along the x direction, which allows us to parametrize the eigenstates by the good quantum number k_x; (*ii*) *finite geometry* - the system is finite in both the x- and y direction. Second, to gain a better physical understanding, we then treat the problem also analytically.

6.2.1 Spectrum of Andreev Bound State Bands

In order to better understand the evolution of the ABSBs, it is instructive to consider the effect of a potential barrier of height V at the interfaces between the superconducting and the normal regions ($y = \pm W/2$) [84]. If V is very large, the interfaces are intransparent such that there are two independent superconducting regions and an isolated normal region, which consists of two tunnel-coupled quantum wires. Since the physics of the normal region in the confined direction (y direction) is equivalent to a particle in a box, the spectrum consists of quantized transverse subbands labeled by an index n, where the spacing between them depends on the width W and roughly behaves as $1/W^2$. Out of these subbands only the ones crossing the chemical potential or lying within the superconducting gap are important for us. By increasing W the subband spacing is reduced and as a result more of these will be shifted into the superconducting gap [see Fig. 6.2(a)]. The probability density of the nth subband, $|\psi^{(n)}(y)|^2$, has n peaks, which allows us to determine n numerically from the shape of the wavefunction.

Upon lowering V, the electron and hole bands get coupled with corresponding anti-crossings and, as a result, ABSBs form [see Fig. 6.2(b)]. This picture qualitatively explains why the number of ABSBs increases with W, and that generically the ABSBs have contributions coming from different transverse subbands of the normal region (see Fig. 6.2). For $\Gamma \neq 0$, the ABSB spreads in both layers. More concretely, when a new subband is entering the superconducting gap, the ABSB highest in energy will obtain mainly contributions from this additional subband around $k_x = 0$, while at larger momenta $|k_x|$ it has mainly contributions from a subband with smaller n. As W is further increased the same behavior can be observed for all ABSBs (see Fig. 6.2). For the remainder we will put $V = 0$ and work with ABSBs.

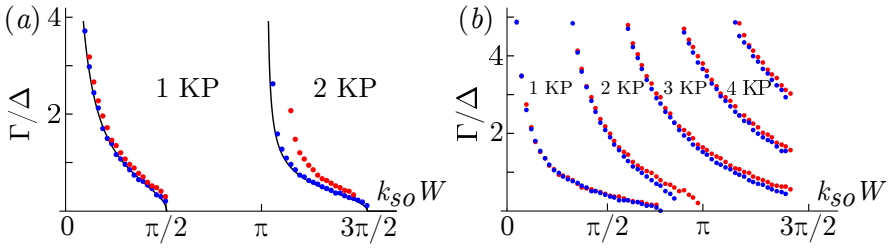

Figure 6.3: Phase diagram as function of $k_{so}W$ and tunneling amplitude Γ for (a) strong SOI ($\Delta = E_{so}/20$) and (b) weak SOI ($\Delta \approx E_{so}$). After each gap closing at $k_x = 0$, a new Kramers pair of MBSs emerges. For strong SOI, we find very good agreement between numerical and analytical [black line, see Eq. (6.3.1)] results. The numerical results (blue dots) are obtained in the semi-infinite geometry and parameters are $N_y = 10000$, $\alpha_1/t = -\alpha_{\bar{1}}/t = 0.07$. In the generic case $|\alpha_1| \neq |\alpha_{\bar{1}}|$, the gap closing line still shows a similar behavior (red dots). Here, we choose $\alpha_1/t = 0.07$ and $\alpha_{\bar{1}}/t = -0.06$.

6.3 Kramers Pairs of MBSs

If the phase difference between the superconductors is $\phi = \pi$, the system is time-reversal invariant and is in the DIII symmetry class and has a $\mathbb{Z}_2$ number classification [85]. The time-reversal (particle-hole) symmetry operator is given by $\Theta = i\sigma_2\mathcal{K}$ ($\mathcal{P} = \eta_1\mathcal{K}$), where η_i are the Pauli matrices acting in particle-hole space, and $\mathcal{K}$ is the complex conjugation operator.

To investigate topological phase transitions, we look for gap closings of the ABSBs at $k_x = 0$, which only happens at particular combinations of $k_{so}W$ and Γ/Δ. An analytical expression for the gap closing condition can be derived in the semi-infinite geometry in the strong SOI limit, *i.e.*, $\Gamma, \Delta \ll E_{so}$, for $\alpha_1 = -\alpha_{\bar{1}}$ and $\Gamma' = 0$ (see Appendix 6.C for details). In this limit, we find a remarkably simple expression for the gap closing condition

$$\left(\frac{\Gamma}{\Delta}\right)^2 - \frac{\cot(k_{so}W)}{k_{so}W} = 0. \tag{6.3.1}$$

We stress that it is essential for obtaining this result to go beyond standard linearization and retain band curvature effects. Thus, for a fixed ratio Γ/Δ there exist multiple solutions, whenever the cotangent is positive [see Fig. 6.3(a)]. In the interval where the cotangent is negative, *e.g.*, for $k_{so}W \in (\pi/2, \pi)$, no gap closing occurs and the ABSBs are always gapped [see Fig. 6.3(a)]. Interestingly, in this region of the phase diagram the topological phase can in principal be achieved with an infinitesimal tunneling amplitude Γ. Relaxing the condition of exactly opposite SOI in the two layers, one finds that the functional form of the gap closing lines remain essentially unchanged (see Fig. 6.3). However, for weak SOI, $\Delta \sim E_{so}$,

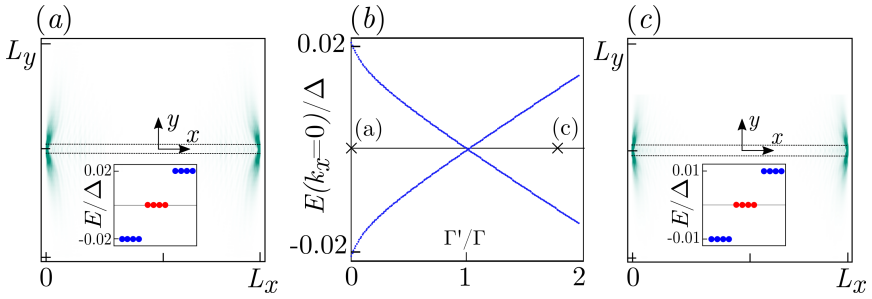

Figure 6.4: Color plot of probability density $|\psi(x,y)|^2$ for two MBSs localized at opposite ends of the junctions for (a) $\Gamma' = 0$ and (c) $\Gamma'/\Gamma = 1.8$. In total, there are four zero-energy MBSs (red dots in spectrum in inset), with two Kramers pairs of MBSs at each end of the junction. The dashed lines symbolize the extension of the normal region. (b) Spectrum at $k_x = 0$ in semi-infinite geometry as function of Γ'/Γ. The gap in the ABSB closes around $\Gamma' \approx \Gamma$ and reopens. The crosses mark the values of Γ'/Γ chosen for panels (a) and (c). A Kramers pair of MBSs exists for both values and the topological phase can thus be reached for both regimes $\Gamma > \Gamma'$ and $\Gamma < \Gamma'$. Parameters are $N_x = 800$, $N_y = 400$, $N_W = 6$, $\alpha_1/t = -\alpha_{\bar{1}}/t = 0.35$, $\Delta = E_{so}/10$, and $\Gamma = 0.6\Delta$.

the functional form deviates from the cotangent behavior, and, more importantly, there are no longer regions where no gap closing takes place [see Fig. 6.3(b)]. Note that the position of the gap closing lines depends on the product $k_{so}W$, which is a useful advantage of the present setup. Suppose that the parameters W and Γ/Δ, which are fixed for a given device, are such that the system is in the trivial phase (the very left region in Fig. 6.3). Then it is always possible to tune the system into the neighboring topological phase by changing the SOI α, *e.g.*, by applying electric fields via external gates. For concreteness we consider numerical parameters relevant for the experiment on single MBS in Josephson junctions[25]: $m = 0.033m_e$, $W = 600$nm, and $\alpha = 34$ meVnm. The maximal relative change of the SOI necessary to enter the neighboring topological phase is then given by $\delta\alpha_{max}/\alpha = \pi\hbar^2/(m\alpha W) \approx 1$. Such *in-situ* tuning of the SOI parameter α was demonstrated in a two-dimensional electron gas [86].

The closing and reopening of the gap of the ABSBs is accompanied by the emergence of a Kramers pairs of MBSs at each end of the normal region (see Fig. 6.4), thus these gap closing points mark topological phase transitions. Due to their topological nature they are robust against potential disorder, as we checked numerically. Importantly, the emergence of the MBSs does neither rely on the fine-tuned point $|\alpha_1| = |\alpha_{\bar{1}}|$ nor on $\Gamma' = 0$. It turns out that MBSs exist for both regimes $\Gamma > \Gamma'$ and $\Gamma < \Gamma'$ (see Fig. 6.4), which implies that the relative strength Γ/Γ' is not crucial to reach the topological phase. However, it is essential that Γ is

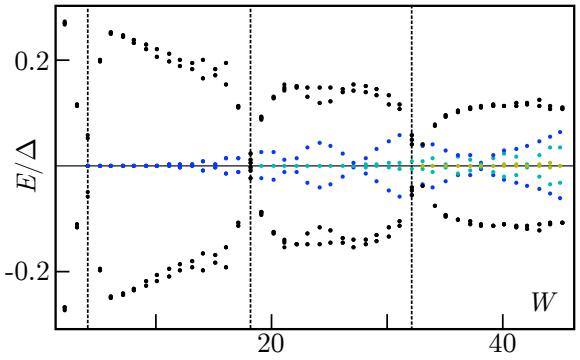

Figure 6.5: Energy of lowest states as function of W. Dashed lines mark the gap closing of the ABSB. After the first closing there are four zero-energy states, one Kramers pairs on each end of the normal region (blue). After the second gap closing there are two Kramers pairs of MBSs on each end (blue and turqoise). These two decoupled sets of MBSs come from the $n = 1$ and $n = 2$ subbands, as can be checked by counting the number of nodes of their wavefunction in y direction. Since the smallest gap of the $n = 1$ subband at the outer Fermi momemtum decreases with increasing W, the localization length increases and hence the zero-energy states are split away from $E = 0$. This behavior repeats after the next gap closing where the $n = 3$ band undergoes a topological phase transition and a third Kramers pair of MBS emerges (green). Parameters are: $N_x = 800$, $N_y = 350$, $\alpha_1/t = -\alpha_{\bar{1}}/t = 0.07$, $\Delta = E_{so}/2$, and $\Gamma = 3\Delta$.

non-zero. This can be qualitatively understood by considering the limit $\Gamma' > 0$ and $\Gamma = 0$. In this case the system consists of two copies of an SNS junction and two tunnel coupled proximitzed Rashba bilayers (for $|y| > W/2$). The tunnel coupling between proximitized layers does not greatly affect the ABSBs since the ABSs exponentially decay into the superconducting regions. Moreover, it was shown [87] that tunnel coupled proximitized Rashba layers with opposite SOI can only be in a TRI topological superconducting phase if their superconducting pairing has a phase difference of $\phi = \pi$. In our setup, the proximitized layers coupled by Γ' have the same phase, and thus are always trivial. In essence, Γ' has no qualitative influence on the topological properties of the system, which are only depending on the hybridization of the ABSBs in the two layers.

As has become clear from the discussion above, for fixed coupling strength Γ and increasing width W, the lowest lying ABSB will change its 'orbital content' around $k_x = 0$ and will have contributions from transverse subbands with larger n while the contributions from subbands with smaller n are 'pushed' to higher values of k_x (see Fig. 6.2). Each time the band gap closes, a new transverse subband with higher n undergoes a topological phase transition with the emergence of a new Kramers pair of MBSs (see Fig. 6.5). The wavefunctions of the MBSs show

that they are localized on one end of the normal region as is expected. In the y direction, however, the states that emerge for larger W have n peaks, revealing that they stem from the topological phase transition of the corresponding subband.

Having discussed the physics around $k_x = 0$, it is also important to look at finite momenta, as the localization length of the MBSs is determined by the smallest gap. Gaps at higher momenta, where the band has contributions from lower subbands, become smaller with increasing W and thus, the localization length of MBSs coming from these subbands increases [88, 89]. This delocalization leads to a larger overlap of their wavefunction and thus they split in energy (see Fig. 6.5) Typically, when a new Kramers pair of MBSs emerges, the MBSs coming from subbands with lower n are already split due their overlap, and there is only one Kramers pair of MBSs at each end that is at zero-energy. Thus, disorder induced coupling between an even number of Kramers pairs is suppressed since they are no longer energetically degenerate. As we have verified numerically, the phases with an even number of Kramers pairs of MBSs are indeed quite robust against potential disorder. Only in the limit where the junction is much longer in the x direction than any of the localization lengths, the MBSs on opposite ends do not overlap, and one can always find a term that gaps out all MBSs without violating any symmetries. Strictly speaking only the phases with an odd number of Kramers pair of MBSs are topologically protected and thus stable against any symmetry-respecting perturbations.

6.4 Breaking Time-Reversal Symmetry

If TRS is broken by a Zeeman field along the x direction, the system behaves similarly to what is known in topological double nanowires setups [47]. Increasing Δ_Z continuously from zero brings the system into a trivial phase until a critical field value is reached and the gap of the ABSBs closes. Increasing Δ_Z further leads to a reopening of the gap and the system enters a topological phase with a total of two MBSs, one MBS at each end of the normal region, see Appendix 6.D Importantly, there exist regions where the topological phase can be reached with relatively small Zeeman fields (see Fig. 6.6).

6.5 Conclusions

We considered a Josephson bijunction which can be controllably brought into a TRI topological superconducting phase with a Kramers pair of MBSs. Using a relatively simple effective model, we show that the tunnel coupling between the

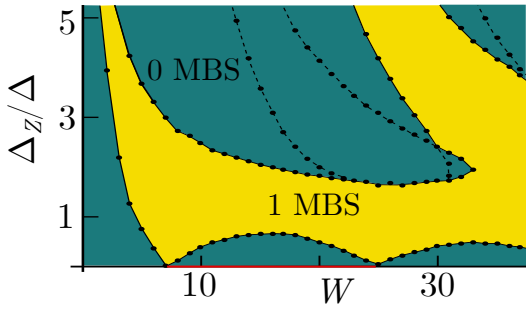

Figure 6.6: Phase diagram as function of in-plane Zeeman field Δ_Z and W. The Zeeman field is aligned along the x direction. The solid black lines mark the topological phase transitions between the trivial (green) and the topological (yellow) phase, which harbors one MBS at each end of the normal region. Dashed lines mark closings of the gap of the ABSBs, which do not correspond to topological phase transitions. The TRI topolgical phase for $\Delta_Z = 0$ (red line) evolves into a trivial phase by continuously increasing the Zeeman field since the pair of MBSs on one end is no longer protected. The phase boundaries were obtained for the same numerical parameters as in Fig. 6.3b and for $\Gamma = 1.5\Delta$.

ABSBs induces a topological phase transition and derive an analytical expression for the topological phase criterion. The possibility for a TRI topological phase only depends on the presence of a non-zero tunneling amplitude between the normal regions, and does not depend on the tunneling amplitude between the proximitized layers. We show, that a finite size system can have multiple localized bound states that are split away from zero energy, but which are still quite robust against non-magnetic disorder. This is due to the simultaneous growth of the localization length of already existing MBS and the topological phase transitions from higher transverse subbands. We also show, that the system can enter a topological phase with a total of two MBS if a Zeeman field is applied along the normal region.

6.6 Acknowledgements

We acknowledge helpful discussions with Olesia Dmytruk, Silas Hoffman, and Christopher Reeg. This work was supported by the Swiss National Science Foundation and NCCR QSIT. This project received funding from the European Union's Horizon 2020 research and innovation program (ERC Starting Grant, grant agreement No 757725).

6.A Discretized Lattice Models

In the main text we present numerical results for the semi-infinite and the finite geometries in which the Rashba bilayer system is assumed to have a rectangular shape. In this section we explicitly discretize the total Hamiltonian H defined by Eqs. (6.2.1)-(6.2.3) of the main text.

Semi-Infinite Geometry

In the semi-infinite geometry, we assume, without loss of generality, that the system is translationally invariant along the x and finite along the y direction with the length $L_y = (N_y - 1)a$, where N_y is the number of lattice sites in y direction and a the lattice constant. The width of the left superconducting region is given by $L_1 = (N_1 - 1)a$ and the width of the normal region is $W = (N_W + 1)a$. The total Hamiltonian for the semi-infinite geometry is given by $\bar{H}' = \sum_{k_x}[\bar{H}'_1(k_x) + \bar{H}'_{\bar{1}}(k_x) + \bar{H}'_\Gamma(k_x) + \bar{H}'_{\Gamma'}(k_x) + \bar{H}'_\Delta(k_x)]$ with

$$
\begin{aligned}
\bar{H}'_\tau(k_x) &= \sum_m \Big\{ \sum_\sigma \Big(-tc^\dagger_{k_x\tau(m+1)\sigma} c_{k_x\tau m\sigma} + [-t\cos(k_x a) + \mu_\tau/2 + 2t] c^\dagger_{k_x\tau m\sigma} c_{k_x\tau m\sigma} \Big) \\
&\quad + \tau\tilde{\alpha}\Big[i(c^\dagger_{k_x\tau(m+1)\uparrow} c_{k_x\tau m\downarrow} - c^\dagger_{k_x\tau(m-1)\uparrow} c_{k_x\tau m\downarrow}) + 2i\sin(k_x a) c^\dagger_{k_x\tau m\uparrow} c_{k_x\tau m\downarrow} \Big] + \text{H.c.} \Big\}, \\
\bar{H}'_\Gamma(k_x) &= \Gamma \sum_\sigma \sum_{m=N_1+1}^{N_1+N_W} \Big(c^\dagger_{k_x 1\sigma m} c_{k_x \bar{1}\sigma m} + \text{H.c.} \Big), \\
\bar{H}'_{\Gamma'}(k_x) &= \Gamma' \sum_\sigma \Bigg[\sum_{m=1}^{N_1} \Big(c^\dagger_{k_x 1\sigma m} c_{k_x \bar{1}\sigma m} + \text{H.c.} \Big) + \sum_{m=N_1+N_W+1}^{N_y} \Big(c^\dagger_{k_x 1\sigma m} c_{k_x \bar{1}\sigma m} + \text{H.c.} \Big) \Bigg], \\
\bar{H}'_\Delta(k_x) &= \frac{1}{2} \sum_\tau \sum_{\sigma,\sigma'} \Bigg[\sum_{m=1}^{N_1} \Big(\Delta e^{-i\phi/2} c^\dagger_{k_x\tau m\sigma} [i\sigma_2]_{\sigma\sigma'} c^\dagger_{-k_x\tau m\sigma'} + \text{H.c.} \Big) \\
&\qquad + \sum_{m=N_1+N_W+1}^{N_y} \Big(\Delta e^{i\phi/2} c^\dagger_{k_x\tau m\sigma} [i\sigma_2]_{\sigma\sigma'} c^\dagger_{-k_x\tau m\sigma'} + \text{H.c.} \Big) \Bigg].
\end{aligned}
\tag{6.A.1}
$$

The operator $c^\dagger_{k_x\tau\sigma n}$ creates an electron with momentum k_x and spin projection σ (along z-axis) in the layer τ at the lattice site m. Here, t is the amplitude for a hopping process between two neighboring lattice sites used to set the effective mass as $t = \hbar^2/(2ma^2)$. The spin-flip hopping amplitude $\tilde{\alpha}$ is related to the SOI parameter by $\tilde{\alpha} = \alpha/2a$. The spin-orbit energy E_{so} is given by $E_{so} = \tilde{\alpha}^2/t$ [88, 89]. We use this Hamiltonian to obtain the spectra and wavefunction in Fig. 6.2 in the main text, and to determine the position of the gap closing of the ABSBs.

Finite Rectangular Geometry

In the finite geometry we assume the system to be finite in both x and y directions and of size $L_x \times L_y = (N_x - 1)(N_y - 1)a^2$. The indices (n, m) label sites in the two-dimensional square lattice with $n \in \{1, \ldots, N_x\}$ and $m \in \{1, \ldots, N_y\}$. The total Hamiltonian $\bar{H} = \bar{H}_1 + \bar{H}_{\bar{1}} + \bar{H}_\Gamma + \bar{H}_{\Gamma'} + \bar{H}_D$ in the finite geometry is then given by

$$
\begin{aligned}
\bar{H}_\tau &= \sum_{n,m} \Big\{ \sum_\sigma \Big(- t_x c^\dagger_{\tau\sigma(n+1)m} c_{\tau\sigma nm} - t_y c^\dagger_{\tau\sigma n(m+1)} c_{\tau\sigma nm} + \frac{\mu_\tau + 4t}{2} c^\dagger_{\tau\sigma nm} c_{\tau\sigma nm} + \text{H.c.} \Big) \\
&\quad + \tau\tilde{\alpha} \Big[i (c^\dagger_{\tau\uparrow n(m+1)} c_{\tau\downarrow nm} - c^\dagger_{\tau\uparrow n(m-1)} c_{\tau\downarrow nm}) \\
&\qquad - (c^\dagger_{\tau\uparrow(n+1)m} c_{\tau\downarrow nm} - c^\dagger_{\tau\uparrow(n-1)m} c_{\tau\downarrow nm}) + \text{H.c.} \Big] \Big\}, \\
\bar{H}_\Gamma &= \Gamma \sum_n \sum_{m=N_1+1}^{N_1+N_W} \Big(c^\dagger_{1\sigma nm} c_{\bar{1}\sigma nm} + \text{H.c.} \Big), \\
\bar{H}_{\Gamma'} &= \Gamma' \sum_n \Bigg[\sum_{m=1}^{N_1} \Big(c^\dagger_{1\sigma nm} c_{\bar{1}\sigma nm} + \text{H.c.} \Big) + \sum_{m=N_1+N_W+1}^{N_y} \Big(c^\dagger_{1\sigma nm} c_{\bar{1}\sigma nm} + \text{H.c.} \Big) \Bigg], \\
\bar{H}_\Delta &= \frac{1}{2} \sum_n \sum_{\sigma,\sigma'} \Bigg[\sum_{m=1}^{N_1} \Big(\Delta e^{-i\phi/2} c^\dagger_{\tau\sigma nm} [i\sigma_2]_{\sigma\sigma'} c^\dagger_{\tau\sigma' nm} + \text{H.c.} \Big) \\
&\quad + \sum_{m=N_1+N_W+1}^{N_y} \Big(\Delta e^{i\phi/2} c^\dagger_{\tau\sigma nm} [i\sigma_2]_{\sigma\sigma'} c^\dagger_{\tau\sigma' nm} + \text{H.c.} \Big) \Bigg].
\end{aligned}
\tag{6.A.2}
$$

The operator $c^\dagger_{\tau\sigma nm}$ creates an electron with spin projection σ in the layer τ at the lattice site (n, m). Note that $\bar{H}'$ in the semi-infinite geometry can be obtained from $\bar{H}$ by applying the Fourier transformation in the x direction. We use this Hamiltonian to obtain the spectra and MBS wavefunction in Figs. 6.4 and 6.5 in the main text, as well as to identify the different topological phases.

6.B Hybridization of Transverse Subbands

As discussed in the main text the 'orbital content' of the ABSBs depends on the momentum k_x and changes as a function of W. When W is increased, more transverse subbands of the normal region move into the superconducting gap and as a consequence more ABSBs are formed. Generally, the ABSBs in the tunnel coupled Josephson bijunction are gapped. In the semi-infinite geometry, the gap only closes at $k_x = 0$ (the momentum along the junction) for certain combinations of $k_{so}W$ and Γ/Δ. Examining the wavefunction of the ABS at a fixed momentum reveals which transverse subband is dominating at that point. In order to better understand the topological phase transitions of several transverse subbands, we consider the lowest ABSB at $k_x = 0$, $\Gamma/\Delta = 1.5$, and when W is varied from

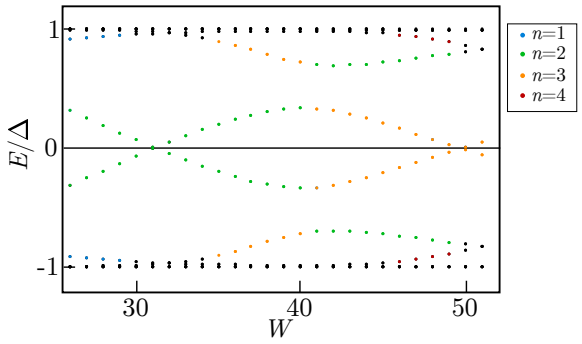

Figure 6.7: Spectrum in the semi-infinite geometry at $k_x = 0$ as a function of W. The lowest ABSB with positive energy has a dominant contribution coming from the $n = 2$ transverse subband (green dots). The gap closes at $W = 30$, which corresponds to the topological phase transition of the $n = 2$ subband. As W is increased, the $n = 3$ subband enters the superconducting gap and the second lowest ABSB in energy has its dominant contribution from this subband (orange dots). At $W = 39$ the dominant contribution is switched and the lowest ABSB has then mainly a contribution from the $n = 3$ subband. At $W = 49$ the gap closes, which corresponds to the topological phase transition of the $n = 3$ subband. Numerical parameters are: $N_x = 1500$, $\alpha_1/t = -\alpha_{\bar{1}}/t = 0.066$, $\Delta = E_{so}/2$, $\Gamma/\Delta = 1.5$, and $V = t/10$.

$W = 26$ to $W = 51$ (see Fig. 6.7). For $W = 26$ the dominant contribution is coming from the second transverse subband. As W is increased, the gap closes at $W = 31$ and then reopens as W is increased further. This corresponds to the topological phase transition of the second transverse subband. Since the width of the normal region is increased, a new ABSB forms and the second lowest ABSB then has a dominant contribution from the third transverse subband. At some point the second and third transverse subband hybridize, such that the dominant contribution of the lowest ABSB is switched (at $W = 40$) and the situation is now opposite. Increasing W further, the gap of the lowest ABSB then closes at $W = 50$, which corresponds to the topological phase transition of the third transverse subband. While for the lowest ABSB the main contribution at $k_x = 0$ is coming from higher transverse subbands as W is increased, the contribution of the lower transverse subbands appears at finite momenta (see Fig. 6.8). The local minima at these finite momenta, where the band has dominant contributions from lower subbands, determines the localization lengths of potential bound states [90]. For $W = 41$, the $n = 1$ and the $n = 2$ subbands are in the topological phase (see Fig. 6.7), and as the gaps around $|k_x| = 0.17$ ($n = 1$) and around $|k_x| = 0.12$ ($n = 2$) are quite small (see Fig. 6.8), the localization length of the MBS become quite large. We note that these localization lengths can be decreased if zigzag-shaped

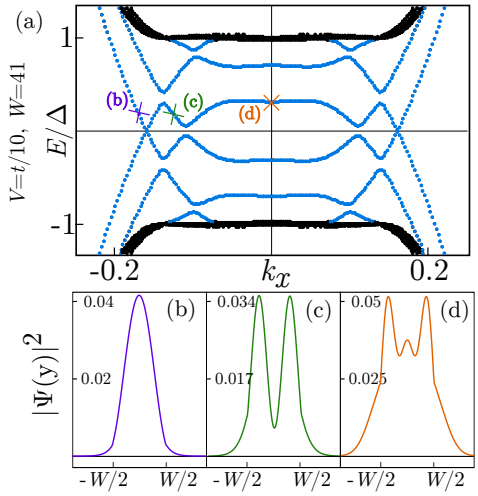

Figure 6.8: Spectrum in the semi-infinite geometry for $W = 41$, $\Gamma/\Delta = 1.5$ and $V = t/10$. At this point there are three ABSBs (blue dots) in the superconducting gap (black dots). The probability density of the wavefunction of the lowest ABSB at (b) $k_x = -0.17$ (purple), (c) $k_x = -0.12$ (green), and (d) $k_x = 0$ (orange) shows that the band has dominant contributions from lower subbands [(b) $n = 1$ and (c) $n = 2$] at finite momenta. Numerical parameters are the same as in Fig. 6.7.

boundaries of the SNS interface are considered [91]. This explains the behavior discussed in Fig. 6.5 in the main text.

6.C ABS Wavefunction and Topological Phase Transition Criterion

In this section we give a detailed derivation of the ABS wavefunction present in the coupled Josephson junction setup. As explained in the main text, we assume the system to be translationally invariant along the x direction (along the junction), and finite in the y direction. We then focus on the subgap states at $k_x = 0$ with energy $E < \Delta$ and the time-reversal invariant case $\phi = \pi$. The BdG equations for this problem then read

$$\left[-\eta_3\frac{\hbar^2}{2m}\partial_y^2 - i\tau\alpha\partial_y\sigma_1 + \bar{\Gamma}(y)\tau_1\eta_3 - \Delta(y)\eta_2\sigma_2\right]\tilde{\Phi}_E(y) = E\tilde{\Phi}_E(y), \tag{6.C.1}$$

where $\bar{\Gamma}(y) = \Gamma\theta(W/2 - |y|)$, and $\Delta(y) = \mathrm{sgn}(y)\Delta\theta(|y| - W/2)$ and without loss of generality we assume $\Gamma > 0$ and $\Delta > 0$, as discussed in the main text. The wavefunction $\bar{\Phi}_E(y)$ is given by

$$\bar{\Phi}_E(y) = [u_{E,1\uparrow}(y), u_{E,1\downarrow}(y), v_{E,1\uparrow}(y), v_{E,1\downarrow}(y), u_{E,\bar{1}\uparrow}(y), u_{E,\bar{1}\downarrow}(y), v_{E,\bar{1}\uparrow}(y), v_{E,\bar{1}\downarrow}(y)]. \tag{6.C.2}$$

By inspecting Eq. (6.C.1) one can see that there are actually two decoupled sets of equations, one only involving $\Phi_E^{(1)}(y) = [u_{E,1\uparrow}(y), v_{E,1\downarrow}(y), u_{E,\bar{1}\uparrow}(y), v_{E,\bar{1}\downarrow}(y)]$ and the other only involving $\Phi_E^{(2)}(y) = [u_{E,1\downarrow}(y), v_{E,1\uparrow}(y), u_{E,\bar{1}\downarrow}(y), v_{E,\bar{1}\uparrow}(y)]$. Since these two sectors are decoupled the spectrum is two-fold degenerate, and it is enough to focus on one sector in order to derive the zero-energy condition. Without loss of generality, we solve the BdG equations for $\Phi_E^{(1)}(y)$ and we drop from now on the superscript. First, we perform a unitary transformation $U = e^{i\pi\sigma_2/4}$, which maps $\sigma_1 \to \sigma_3$ and $\sigma_3 \to -\sigma_1$. With these preparations the reduced BdG equations read

$$\begin{pmatrix} -\hbar^2/2m\partial_y^2 - i\alpha\partial_y & 0 & \Gamma(y) & \Delta(y) \\ 0 & \hbar^2/2m\partial_y^2 + i\alpha\partial_y & -\Delta(y) & -\Gamma(y) \\ \Gamma(y) & -\Delta^*(y) & -\hbar^2/2m\partial_y^2 + i\alpha\partial_y & 0 \\ \Delta^*(y) & -\Gamma(y) & 0 & \hbar^2/2m\partial_y^2 - i\alpha\partial_y \end{pmatrix} \Phi(y) = 0, \tag{6.C.3}$$

which are then solved in the normal region $|y| < W/2$, in the left superconducting region $y < -W/2$, and in the right superconducting region $y > W/2$. The general solution in the normal region is given by

$$\begin{aligned} \Phi^{(N)}(y) = {} & a_1 \left[0, -\frac{2E_{so}\lambda_-}{\Gamma}\left(\lambda_- + \sqrt{2}\right), 0, 1\right] e^{-i\sqrt{2}\lambda_- k_{so} y} \\ & + a_2 \left[0, -\frac{2E_{so}\lambda_-}{\Gamma}\left(\lambda_- - \sqrt{2}\right), 0, 1\right] e^{i\sqrt{2}\lambda_- k_{so} y} \\ & + a_3 \left[0, -\frac{2E_{so}\lambda_+}{\Gamma}\left(\lambda_+ + \sqrt{2}\right), 0, 1\right] e^{-i\sqrt{2}\lambda_+ k_{so} y} \\ & + a_4 \left[0, -\frac{2E_{so}\lambda_+}{\Gamma}\left(\lambda_+ - \sqrt{2}\right), 0, 1\right] e^{i\sqrt{2}\lambda_+ k_{so} y} \\ & + a_5 \left[-\frac{2E_{so}\lambda_-}{\Gamma}\left(\lambda_- + \sqrt{2}\right), 0, 1, 0\right] e^{-i\sqrt{2}\lambda_- k_{so} y} \\ & + a_6 \left[-\frac{2E_{so}\lambda_-}{\Gamma}\left(\lambda_- - \sqrt{2}\right), 0, 1, 0\right] e^{i\sqrt{2}\lambda_- k_{so} y} \\ & + a_7 \left[-\frac{2E_{so}\lambda_+}{\Gamma}\left(\lambda_+ + \sqrt{2}\right), 0, 1, 0\right] e^{-i\sqrt{2}\lambda_+ k_{so} y} \\ & + a_8 \left[-\frac{2E_{so}\lambda_+}{\Gamma}\left(\lambda_+ - \sqrt{2}\right), 0, 1, 0\right] e^{i\sqrt{2}\lambda_+ k_{so} y}, \end{aligned} \tag{6.C.4}$$

where $\lambda_\pm = \sqrt{1 \pm \sqrt{1 + \frac{\Gamma^2}{4E_{so}^2}}}$. Since we are interested in subgap solutions with $E < \Delta$, the states have to be decaying in the superconducting regions. For the left

superconducting region $y < -W/2$ the solution has to decay for $y \to -\infty$. We find,

$$\begin{aligned}\Phi^{(L)}(y) = a_9\,[1,1,0,0]\,e^{-ik_{so}y\left(1+\sqrt{1+i\frac{\Delta}{E_{so}}}\right)} + a_{10}[-1,1,0,0]e^{ik_{so}y\left(-1+\sqrt{1-i\frac{\Delta}{E_{so}}}\right)} \\ + a_{11}[0,0,-1,1]e^{ik_{so}y\left(1+\sqrt{1-i\frac{\Delta}{E_{so}}}\right)} + a_{12}[0,0,1,1]e^{-ik_{so}y\left(-1+\sqrt{1+i\frac{\Delta}{E_{so}}}\right)}.\end{aligned} \tag{6.C.5}$$

Analogously one finds the wavefunction in the right superconducting region, which decays for $y \to \infty$,

$$\begin{aligned}\Phi^{(R)}(y) = a_{13}[0,0,-1,1]e^{ik_{so}y\left(1+\sqrt{1+i\frac{\Delta}{E_{so}}}\right)} + a_{14}[0,0,1,1]e^{-ik_{so}y\left(-1+\sqrt{1-i\frac{\Delta}{E_{so}}}\right)} \\ + a_{15}[1,1,0,0]e^{-ik_{so}y\left(1+\sqrt{1-i\frac{\Delta}{E_{so}}}\right)} + a_{16}[-1,1,0,0]e^{ik_{so}y\left(-1+\sqrt{1+i\frac{\Delta}{E_{so}}}\right)}.\end{aligned} \tag{6.C.6}$$

The total ABS wavefunction then reads $\Phi(y) = \Phi^{(L)}(y)\theta(-y-W/2)+\Phi^{(N)}(y)\theta(W/2-|y|) + \Phi^{(R)}(y)\theta(y-W/2)$. One has to impose the boundary conditions at the two interfaces,

$$\Phi^{(R)}(-W/2) - \Phi^{(N)}(-W/2) \stackrel{!}{=} 0, \tag{6.C.7}$$

$$\partial_y\Phi^{(R)}(-W/2) - \partial_y\Phi^{(N)}(-W/2) \stackrel{!}{=} 0, \tag{6.C.8}$$

$$\Phi^{(L)}(W/2) - \Phi^{(N)}(W/2) \stackrel{!}{=} 0, \tag{6.C.9}$$

$$\partial_y\Phi^{(L)}(W/2) - \partial_y\Phi^{(N)}(W/2) \stackrel{!}{=} 0, \tag{6.C.10}$$

which can be recast in matrix form as

$$Ma = 0, \tag{6.C.11}$$

where $a = (a_1, \ldots, a_{16})$ is the vector of linear coefficients. Non-trivial solutions exist only if the matrix M is singular, *i.e.*, $\det(M) = 0$. The solution of this equation then yields the condition on the system parameters ($k_{so}W$, Γ, Δ) under which a zero-energy ABS exists. This is the topological phase transition criterion we are looking for. As can be seen above, the presence of the square root factors makes it impossible to find an analytical closed form expression. However, in the strong SOI limit, *i.e.*, Γ, $\Delta \ll E_{so}$, these square roots can be expanded and thus the matrix M and the equation Eq. (6.C.11) are expanded in the strong SOI limit, and can be brought into form

$$\det(M) = f^{(0)}(k_{so}W,\Gamma,\Delta) + \frac{f^{(1)}(k_{so}W,\Gamma,\Delta)}{E_{so}} + \frac{f^{(2)}(k_{so}W,\Gamma,\Delta)}{E_{so}^2} \stackrel{!}{=} 0\,. \tag{6.C.12}$$

In doing so, we find

$$\begin{aligned} f^{(0)}(k_{so}W,\Gamma,\Delta) &= 0,\\ f^{(1)}(k_{so}W,\Gamma,\Delta) &= 0,\\ f^{(2)}(k_{so}W,\Gamma,\Delta) &= -\frac{\cos(k_{so}W)\left[\Delta^2 - k_{so}W\Gamma^2\tan(k_{so}W)\right]}{\Gamma^2}. \end{aligned} \tag{6.C.13}$$

Thus, for $\Gamma > 0$, Eq. (6.C.12) can only be fulfilled if

$$\frac{\Gamma^2}{\Delta^2} = \frac{\cot(k_{so}W)}{k_{so}W}. \tag{6.C.14}$$

One can see that the system only has zero-energy bound states when the cotangent is positive, since throughout the derivation it was assumed that $\Gamma > 0$.

6.D Effect of Breaking Time-Reversal Symmetry

In the main text we presented the results for the TRI topological superconducting phase and briefly mentioned the effect of breaking time-reversal symmetry (TRS). In this section we give a more detailed discussion of the TRS broken phase.

In our system, TRS can be broken by either deviating from a π-junction, *i.e.*, $\phi = \pi + \delta\phi$, or by applying a Zeeman field. The TRS breaking term coming from the deviation from a π-junction, acts in the same way on all states independently of their spin-structure. This results in trivially gapping out the MBS, and the system is always in a trivial phase.

We take into account the effect of applying a Zeeman field along the junction (the x direction), by adding the term

$$H_Z = \sum_{\tau,\sigma,\sigma'} \int d\boldsymbol{r}\ \bar{\Delta}_Z(y)\Big(\psi_{\tau\sigma}(\boldsymbol{r})^\dagger[\sigma_1]_{\sigma\sigma'}\psi_{\tau\sigma'}(\boldsymbol{r}) + \text{H.c.}\Big), \tag{6.D.1}$$

where $\bar{\Delta}_Z(y) = \Delta_Z\theta(W/2 - |y|)$, and we assume without loss of generality that $\Delta_Z \geq 0$. We find that the Zeeman field leads to a closing of the gap in the ABSBs at $k_x = 0$ for some critical fields. Starting with $\Delta_Z = 0$ for some fixed width W, one starts in the TRI topological phases discussed in the main text, which then become trivial under the application of the Zeeman field, since the Kramers pairs of MBS are gapped out. Increasing Δ_Z furhter until the ABSB gap closes and reopens the first time, the system enters a topological phase with one MBS at each end of the junction (see Fig. 6.6). After the second gap closing and reopening the system has an even number of MBS, which are not protected against disorder, and indeed we observe that they split as a function of disorder strength, and hence, this region is also trivial.

Bibliography

[1] A. Y. Kitaev, Phys.-Usp. **44**, 131 (2001).

[2] R. M. Lutchyn, J. D. Sau, and S. D. Sarma, Phys. Rev. Lett. **105**, 077001 (2010).

[3] Y. Oreg, R. Refael, and F. von Oppen, Phys. Rev. Lett. **105**, 177002 (2010).

[4] J. Alicea, Phys. Rev. B **81**, 125318 (2010).

[5] W. Chang, S. M. Albrecht, T. S. Jespersen, F. Kuemmeth, P. Krogstrup, J. Nygård, and C. M. Marcus, Nat. Nano. **10**, 232 (2015).

[6] S. Gazibegovic, D. Car, H. Zhang, S. C. Balk, J. A. Logan, M. W. A. de Moor, M. C. Cassidy, R. Schmits, D. Xu, G. Wang, P. Krogstrup, R. L. M. Op het Veld, K. Zuo, Y. Vos, J. Shen, D. Bouman, B. Shojaei, D. Pen- nachio, J. S. Lee, P. J. van Veldhoven, S. Koelling, M. A. Verheijen, L. P. Kouwenhoven, C. J. Palmstrøm, and E. P. A. M. Bakkers, Nature **548**, 434 (2017).

[7] M. Kjaergaard, F. Nichele, H. J. Suominen, M. P. Nowak, M. Wimmer, A. R. Akhmerov, J. A. Folk, K. Flensberg, J. Shabani, C. J. Palmstrøm, and C. M. Marcus, Nat. Commun. **7**, 12841 (2016).

[8] J. Shabani, M. Kjaergaard, H. J. Suominen, Y. Kim, F. Nichele, K. Pakrouski, T. Stankevic, R. M. Lutchyn, P. Krogstrup, R. Feidenhans'l, S. Kraemer, C. Nayak, M. Troyer, C. M. Marcus, and C. J. Palmstrøm, Phys. Rev. B **93**, 155402 (2016).

[9] R. M. Lutchyn, G. W. Winkler, B. van Heck, T. Karzig, K. Flensberg, L. I. Glazman, and C. Nayak, arXiv:1809.05512.

[10] S. Vaitiekenas, M.-T. Deng, P. Krogstrup, and C. M. Marcus, arXiv:1809.05513.

[11] S. Nadj-Perge, I. K. Drozdov, J. Li, H. Chen, S. Jeon, J. Seo, A. H. MacDonald, B. A. Bernevig, and A. Yazdani, Science **346**, 602 (2014).

[12] M. Ruby, F. Pientka, Y. Peng, F. von Oppen, B. W. Heinrich, and K. J. Franke, Phys. Rev. Lett. **115**, 197204 (2015).

[13] R. Pawlak, M. Kisiel, J. Klinovaja, T. Meier, S. Kawai, T. Glatzel, D. Loss, and E. Meyer, Npj Quantum Inform. **2**, 16035 (2016).

[14] J. Klinovaja, P. Stano, A. Yazdani, D. Loss, Phys. Rev. Lett., **111** 186805 (2013).

[15] B. Braunecker and P. Simon, Phys. Rev. Lett. **111**, 147202 (2013).

[16] M. M. Vazifeh and M. Franz, Phys. Rev. Lett. **111**, 206802 (2013).

[17] S. Nadj-Perge, I. K. Drozdov, B. A. Bernevig, and A. Yazdani, Phys. Rev. B **88**, 020407(R) (2013).

[18] F. Pientka, L. I. Glazman, and F. von Oppen, Phys. Rev. B **88**, 155420 (2013).

[19] R. Rawlak, S. Hoffman, J. Klinovaja, D. Loss, and E. Meyer, Progress in Particle and Nuclear Physics **107**, 1 (2019).

[20] F. Pientka, A. Keselman, E. Berg, A. Yacoby, A. Stern, and B. I. Halperin, Phys. Rev. X **7**, 021032 (2017).

[21] M. Hell, M. Leijnse, and K. Flensberg, Phys. Rev. Lett. **118**, 107701 (2017).

[22] M. Hell, K. Flensberg, and M. Leijnse, Phys. Rev. B **96**, 035444 (2017).

[23] S. Hart, H. Ren, M. Kosowsky, G. Ben-Shach, P. Leubner, C. Bruune, H. Buhmann, L. W. Molenkamp, B. I. Halperin, and A. Yacoby, Nat. Phys. **13**, 87 (2017).

[24] H. J. Suominen, M. Kjaergaard, A. R. Hamilton, J. Shabani, C. J. Palmstrøm, C. M. Marcus, and F. Nichele, Phys. Rev. Lett. **119**, 176805 (2017).

[25] H. Ren, F. Pientka, S. Hart, A. Pierce, M. Kosowsky, L. Lunczer, R. Schlereth, B. Scharf, E. M. Hankiewicz, L. W. Molenkamp, B. I. Halperin, and A. Yacoby, arXiv:1809.03076.

[26] A. Fornieri, A. M. Whiticar, F. Setiawan, E. P. Martin, A. C. C. Drachmann, A. Keselman, S. Gronin, C. Thomas, T. Wang, R. Kallaher, G. C. Gardner, E. Berg, M.J. Manfra, A. Stern, C. M. Marcus, and F. Nichele, arXiv:1809.03037.

[27] D. T. Liu, J. Shabani, and A. Mitra, Phys. Rev. B **97**, 235114 (2018).

[28] B. Scharf, F. Pientka, H. Ren, A. Yacoby, and E. M. Hankiewicz, arXiv:1904.08981.

[29] J. Zhi, N. Kang, S. Li, D. Fan, F. Su, D. Pan, S. Zhao, J. Zhao, and H. Xu Phys. Status Solidi B **256**, 1800538 (2019).

[30] J. S. Lee, B. Shojaei, M. Pendharkar, A. P. McFadden, Y. Kim, H. J. Suominen, M. Kjaergaard, F. Nichele, H. Zhang, C. M. Marcus, and C. J. Palmstrøm, Nano Lett. **19**, 3083 (2019).

[31] F. Setiawan, A. Stern, and E. Berg, Phys. Rev. B **99**, 220506(R) (2019).

[32] L. Fu and C. L. Kane, Phys. Rev. Lett. **100**, 096407 (2008).

[33] X. L. Qi, T. L. Hughes, S. Raghu, and S. C. Zhang, Phys. Rev. Lett. **102**, 187001 (2009).

[34] M. Sato and S. Fujimoto, Phys. Rev. B **79**, 094504 (2009).

[35] L. Fu and E. Berg, Phys. Rev. Lett. **105**, 097001 (2010).

[36] C. X. Liu and B. Trauzettel, Phys. Rev. B **83**, 220510(R) (2011).

[37] S. Nakosai, Y. Tanaka, and N. Nagaosa, Phys. Rev. Lett. **108**, 147003 (2012).

[38] S. Deng, L. Viola, and G. Ortiz, Phys. Rev. Lett. **108**, 036803 (2012).

[39] F. Zhang, C. L. Kane, and E. J. Mele, Phys. Rev. Lett. **111**, 056402 (2013).

[40] A. Haim, A. Keselman, E. Berg, and Y. Oreg, Phys. Rev. B **89**, 220504(R) (2014).

[41] E. Gaidamauskas, J. Paaske, and K. Flensberg, Phys. Rev. Lett. **112**, 126402 (2014).

[42] J. Klinovaja and D. Loss, Phys. Rev. B **90**, 045118 (2014).

[43] C. P. Orth, R. P. Tiwari, T. Meng, and T. L. Schmidt, Phys. Rev. B **91**, 081406(R) (2015).

[44] J. Klinovaja and D. Loss, Phys. Rev. B **92**, 121410(R) (2015).

[45] J. Wang, Phys. Rev. B **94**, 214502 (2016).

[46] F. Parhizgar and A. M. Black-Schaffer, Sci. Rep. **7**, 9817 (2017).

[47] C. Schrade, M. Thakurathi, C. Reeg, S. Hoffman, J. Klinovaja, and D. Loss, Phys Rev. B **96**, 035306 (2017).

[48] A. Camjayi, L. Arrachea, A. Aligia, and F. von Oppen, Phys. Rev. Lett. **119**, 046801 (2017).

[49] Z. Yan, F. Song, and Z. Wang, Phys. Rev. Lett. **121**, 096803 (2018).

[50] Q. Wang, C.-C. Liu, Y.-M. Lu, and F. Zhang, Phys. Rev. Lett. **121**, 186801 (2018).

[51] C.-H. Hsu, P. Stano, J. Klinovaja, and D. Loss, Phys. Rev. Lett. **121**, 196801 (2018).

[52] C. Schrade and L. Fu, Pyhs. Rev. Lett. **120**, 267002 (2018).

[53] A. A. Aligia and L. Arrachea, Phys. Rev. B **98**, 174507 (2018).

[54] O. Dmytruk, M. Thakurathi, D. Loss, J. Klinovaja, Phys. Rev. B **99**, 245416 (2019).
[55] F. Schulz, J. C. Budich, E. G. Novik, P. Recher, and B. Trauzettel, arXiv:1904.07166.
[56] A. Haim, E. Berg, K. Flensberg, and Y. Oreg, Phys. Rev. B **94**, 161110(R) (2016).
[57] M. Thakurathi, P. Simon, I. Mandal, J. Klinovaja, and D. Loss, Phys. Rev. B **97**, 045415 (2018).
[58] A. I. Buzdin, L. N. Bulaevskii, and S.V. Panyukov, Pis'ma Zh. Eksp. Teor. Fiz. **35**, 147 (1982) [JETP Lett. **35**, 178 (1982)].
[59] V.V. Ryazanov, V.A. Oboznov, A. Yu. Rusanov, A.V. Veretennikov, A.A. Golubov, and J. Aarts, Phys. Rev. Lett. **86**, 2427 (2001).
[60] B. I. Spivak and S. A. Kivelson, Phys. Rev. B **43**, 3740 (1991).
[61] J. A. van Dam, Y.V. Nazarov, E. P.A.M. Bakkers, and L. P. Kouwenhoven, Nature (London) **442**, 667 (2006).
[62] C. Schrade, A. A. Zyuzin, J. Klinovaja, and D. Loss, Phys. Rev. Lett. **115**, 237001 (2015).
[63] J. Nitta, T. Akazaki, H. Takayanagi, and T. Enoki, Phys. Rev. Lett. **78**, 1335 (1997).
[64] G. Engels, J. Lange, T. Schapers, and H. Luth, Phys. Rev. B **55**, R1958 (1997).
[65] F. Dettwiler, J. Fu, S. Mack, P. J. Weigele, J. C. Egues, D. D. Awschalom, and D. M. Zumbuhl, Phys. Rev. X **7**, 031010 (2017).
[66] Y. Cao, V. Fatemi, S. Fang, K. Watanabe, T. Taniguchi, E. Kaxiras, and P. Jarillo-Herrero, Nature **556**, 43-50 (2018).
[67] Y. Cao, V. Fatemi, A. Demir, S. Fang, S. K. Tomarken, J. Y. Luo, J. D. Sanchez-Yamagishi, K. Watanabe, T. Taniguchi, E. Kaxiras, R. C. Ashoori, and P. Jarillo-Herrero, Nature **556**, 80-84 (2018).
[68] M. Yankowitz, S. Chen, H. Polshyn, Y. Zhang, K. Watanabe, T. Taniguchi, D. Graf, A. F. Young, C. R. Dean, Science **363**, 1059 (2019).
[69] Y. Xie, B. Lian, B. J äck, X. Liu, C.-L. Chiu, K. Watanabe, T. Taniguchi, B. A. Bernevig, and A. Yazdani, Nature **572**, 101 (2019).
[70] K. Novoselov, V. Fal'ko, L. Colombo, P. Gellert, M. Schwab, and K. Kim, Nature **490**, 192 (2012).
[71] B. Sachs, L. Britnell, T. O. Wehling, A. Eckmann, R. Jalil, B. D. Belle, A. I. Lichtenstein, M. I. Katsnelson, and K. S. Novoselov, App. Phys. Lett. **103** 251607 (2013).
[72] A. K. Geim and I. V. Grigorieva, Nature **499**, 419 (2013).
[73] K. S. Novoselov, A. Mishchenko, A. Carvalho, and A. H. Castro Neto, Science **353**, 6298 (2016).
[74] Y. Liu, N. O. Weiss, X. Duan, H.-C. Cheng, Y. Huang, and X. Duan, Nat. Rev. Mat. **1**, 16042 (2016).
[75] C. Reeg, J. Klinovaja, D. Loss, Physical Review B **96**, 081301(R) (2017).
[76] We note that crossed Andreev superconducting pairing [77–82] is suppressed in this setup since the signs of the SOI couplings $\alpha_\tau = |\boldsymbol{\alpha}_\tau|$ are opposite.
[77] M. S. Choi, C. Bruder, and D. Loss, Phys. Rev. B **62**, 13569 (2000).
[78] G. Deutscher, Appl. Phys. Lett. **76**, 487 (2000).
[79] P. Recher, E. V. Sukhorukov, and D. Loss, Phys. Rev. B **63**, 165314 (2001).
[80] L. Hofstetter, S. Csonka, J. Nygard, and C. Schonenberger, Nature (London) **461**, 960 (2009).
[81] A. Das, Y. Ronen, M. Heiblum, D. Mahalu, A. V. Kretinin, and H. Shtrikman, Nat. Commun. **3**, 1165 (2012).

[82] S. Baba, C. Junger, S. Matsuo, A. Baumgartner, Y. Sato, H. Kamata, K. Li, S. Jeppesen, L. Samuelson, H. Xu, C. Schonenberger, and S. Tarucha, arXiv:1802.08059.

[83] C. Reeg, D. Loss, J. Klinovaja, Beilstein Journal of Nanotechnology **9**, 1263 (2018).

[84] O. Dmytruk, D. Chevallier, D. Loss, and J. Klinovaja, Phys. Rev. B **98**, 165403 (2018).

[85] S. Ryu, A. P. Schnyder, A. Furusaki, and A. W. W. Ludwig, New J. Phys. **12**, 065010 (2010).

[86] F. Dettwiler, J. Fu, S. Mack, P. J. Weigele, J. C. Egues, D. D. Awschalom, and D. M. Zumbühl, Phys. Rev. X **7**, 031010 (2017).

[87] Y. Volpez, D. Loss, and J. Klinovaja, Physical Review Lett. **122**, 126402 (2019).

[88] D. Rainis, L. Trifunovic, J. Klinovaja, D. Loss, Physical Review B **87**, 024515 (2013).

[89] E. Prada, P. San-Jose, R . Aguado, Physical Review B **86**, 180503(R) (2012).

[90] J. Klinovaja and D. Loss, Physical Review B **86**, 085408 (2012).

[91] T. Laeven, B. Nijholt, M. Wimmer, and A. R Akhmerov, arXiv:1903.06168.

Curriculum vitae

Personal data

Name	Yanick Volpez
Place and date of birth	Frauenfeld, Switzerland, 24.09.1990
Nationality	Swiss
Address	Wylerstrasse 43, 3014 Bern, Switzerland
Email	yanickandre.volpez@unibas.ch

Employment

2016-2020 — *Basel, Switzerland*
Doctoral Candidate, University of Basel
Conducting research in the Condensed Matter Theory and Quantum Computing group
Supervisors: Prof. Dr. Daniel Loss and Prof. Dr. Jelena Klinovaja

2015-2016 — *Heidelberg, Germany*
Teaching Assistant, Heidelberg University
Conducting teaching classes for lectures in theoretical physics

Education

2016-2020 — *Basel, Switzerland*
Ph. D. in Theoretical Physics, University of Basel

Thesis	Topological Quantum Matter in Layered Systems with Rashba Spin-Orbit Interaction
Supervisor	Prof. Dr. Daniel Loss and Prof. Dr. Jelena Klinovaja
Institute	Basel Centre for Quantum Computing and Quantum Coherence

2014-2016 — *Heidelberg, Germany*
M. Sc. in Physics, Heidelberg University

Thesis	Correlated Fermions on Hexagonal Lattices from the Functional Renormalization Group
Supervisor	PD Dr. Michael Scherer
Institute	Institute for Theoretical Physics, Heidelberg

2010-2014 — *Zürich, Switzerland*
B. Sc. in Physics, University of Zurich

Thesis:	Computation of Two-Loop Master Integrals for qq→VV
Supervisor:	Prof. Dr. Thomas Gehrmann
Institute	Institute for Theoretical Physics, Zürich

2005-2009 — *Frauenfeld, Switzerland*
High-School

Fellowships

2017-2020	**Excellence fellowship** in the Quantum Computing and Quantum Technology Ph. D. School
2016-2019	**Marie Skolodowska-Curie fellowship** Early stage researcher in the European collaborative Innovative Training Network „Spin-NANO“

Publication List

Y. Volpez, D. Loss, and J. Klinovaja,
Time-Reversal Invariant Topological Superconductivity in Planar Josephson Bijunction,
arXiv:1910.06921.

Y. Volpez, D. Loss and J. Klinovaja,
Second Order Topological Superconductivity in π-Junction Rashba Layers,
Phys. Rev. Lett. 122, 126402 (2019).

Y. Volpez, D. Loss and J. Klinovaja,
Rashba Sandwiches with Topological Superconducting Phases,
Phys. Rev. B 97, 195421 (2018).

Y. Volpez, D. Loss, and J. Klinovaja,
Three-Dimensional Fractional Topological Insulators in Coupled Rashba Layers,
Phys. Rev. B 96, 085422 (2017).

Y. Volpez, D. D. Scherer, and M. M. Scherer,
Electronic instabilities of the extended Hubbard model on the honeycomb lattice from functional renormalization,
Phys. Rev. B 94, 165107 (2016).

Conferences & Schools

16.6.-21.6.19 *Hong Kong*	**New Materials and Structures in Topological and Correlated Systems** „Second-Order Topological Superconductivity in π-Junction Rashba Layers“, poster presentation
18.3.-20.3.19 *Toulouse, France*	**Toulouse Workshop 2019** „Second-Order Topological Superconductivity in π-Junction Rashba Layers“, poster presentation
10.9.-14. 9.18 *Konstanz, Germany*	**4th Conference on Spin-Based Quantum Information Processing** „Rashba Sandwiches with Topological Superconducting Phases“, poster presentation
9.9.18 *Konstanz, Germany*	**4th Conference on Spin-Based Quantum Information Processing** Lecture day
5.3.-9.3.18 *Los Angeles, USA*	**APS March Meeting 2018** „Fractional Three-Dimensional Topological Insulators in Coupled Rashba Layers“, talk
5.2.-9.2.18 *Arosa, Switzerland*	**Winter School & Annual Meeting Quantum Science and Technology**

30.1.-3.2.17 **Winter School & Annual Meeting Quantum Science and Technology**
Arosa, Switzerland „Fractional Three-Dimensional Topological Insulators in Coupled Rashba Layers“, poster presentation

11.4.-15.4.16 **36. Heidelberg Physics Graduate Days**
Heidelberg, Germany Courses: Topological Phases in Solids, Geometrical and Topological Methods in Physics

5.10.-9.10.15 **35. Heidelberg Physics Graduate Days**
Heidelberg, Germany Courses: Ideas and Results of the Mathematical Theory of Phase Transitions, Exploring Collective Features of QCD in Heavy Ion Collisions

20.4.-24.4.15 **Fermions 2015 at IWH**
Heidelberg, Germany

7.4.-10.4.15 **34. Heidelberg Physics Graduate Days**
Heidelberg, Germany Courses: Physical Modelling of Neural Circuits, Physics of New Materials: From Carbon Nanotubes to Topological Insulators